Technische Universität München
TUM School of Engineering and Design

A Batch–Evaporation Power Cycle for Low-Temperature Heat Sources: Thermodynamics and Economics

Moritz D. Gleinser, M.Sc.

Vollständiger Abdruck der von der School of Engineering and Design
der Technischen Universität München zur Erlangung des
akademischen Grades eines
Doktors der Ingenieurwissenschaften
genehmigten Dissertation.

Vorsitzender:		Prof. Dr.-Ing. Karsten Stahl
Prüfer der Dissertation:	1.	Prof. Dr.-Ing. Hartmut Spliethoff
	2.	Prof. Dr.-Ing. Dieter Brüggemann Universität Bayreuth

Die Dissertation wurde am 06.12.2021 bei der Technischen Universität München eingereicht und durch die TUM School of Engineering and Design am 20.06.2022 angenommen.

Preface

Die vorliegende Dissertation entstand im Rahmen meiner Tätigkeit als wissenschaftlicher Angestellter am Lehrstuhl für Energiesysteme der TU München.

Herrn Professor Dr.-Ing. Hartmut Spliethoff, Leiter des Lehrstuhls, gilt mein besonderer Dank für seinen Beitrag zu meinem wissenschaftlichen Werdegang bis hin zur Begutachtung der vorliegenden Arbeit. Seine wertvollen Anmerkungen und die stets angenehme Zeit an seinem Lehrstuhl werden mir in guter Erinnerung bleiben.

Ebenso möchte ich mich bei Herrn Professor Dr.-Ing. Dieter Brüggemann von der Universität Bayreuth für die Übernahme des Zweitgutachtens und seine Rolle als Zweitprüfer bedanken.

Außerdem bedanke ich mich herzlich bei Herrn Manfred Moullion der Maschinenwerk Misselhorn MWM GmbH, ohne den die Forschung am Misselhorn Prozess und diese Arbeit nicht möglich gewesen wäre.

Allen Mitarbeitern des Lehrstuhls gilt mein großer Dank für die gute Zusammenarbeit, den regen wissenschaftlichen Austausch und die Unterstützung. Allen voran gilt mein besonderer Dank Dr.-Ing. Christoph Wieland, über den ich mit meiner Masterarbeit überhaupt erst an den Lehrstuhl gekommen bin und der anschließend als mein Gruppenleiter mit zahlreichen fachlichen Diskussionen maßgeblich zum Gelingen des gesamten Forschungsthemas beigetragen hat. Bei den weiteren Kollegen gilt mein Dank im Speziellen den *Coffee Friends* für die vielen, sowohl fachlich als auch persönlich, schönen und wertvollen Stunden am Lehrstuhl: Barbara Gumpert, Felix Fischer, Julia Hentschel, Manuel Würth, Michael Angerer, Sebastian Jell und Wolf Wedel.

Nicht zuletzt bedanke ich mich bei allen Freunden und bei meiner Familie für die Geduld bis diese Arbeit schließlich fertiggestellt war.

Hannover, August 2022

Abstract

The global climate target—reducing the greenhouse gases by 85 % to 90 % until 2050—boosted the utilization of new sustainable and renewable energy sources like photovoltaic, wind turbines and biomass power plants. One closely related approach is the recovery of low temperature heat from industrial waste heat or geothermal energy. While those sources come at an extensive scale and almost "free of charge", there are no simple yet high–performing power cycles for low-temperatures to date. Even though extensive research has been done over the last years, most setups are complex, expensive or not practically realizable at all. This work screens the current options and presents a detailed thermodynamic and economic analysis of a promising batch-evaporation power cycle: the MWM Cycle. First, a theoretical analysis of this dynamic cycle is presented based on revised versions of temperature–heat– and temperature–entropy–diagrams. Second, a dynamic simulation model is introduced, covering heat and mass transfer effects and the influence of thermal inertia on the dynamic behavior. At last, an economic evaluation by means of static and dynamic methods, most importantly the annuity method, is performed with different reference conditions and working fluids. The cycle analysis showed that the dynamic batch evaporation allows for an almost perfect temperature match between heat source and working fluid without the need for complex components. At the temperature of 100 °C, the second law efficiency of the MWM Cycle outperforms a simple ORC by about 39 % (ORC: $\eta_{II} = 30.9\,\%$, MWM: $\eta_{II} = 42.8\,\%$) even with the environmentally recommended "replacement–fluid" R1234ze(E). With regard to the economic figures, the annuity of the MWM Cycle could only compete with the ORC by dismissing the originally estimated reduced operation hours (ORC: 26 500 €, MWM: 33 000 €, +25 %). The overall comparison of different temperatures, working fluids and refund rates showed that the MWM Cycle is a thermodynamically promising and feasible cycle. However, at low temperatures it is, like the ORC, hardly profitable with the electricity prices and regulatory conditions used in this work.

Kurzfassung

Die globalen Klimaziele—Reduktion der Treibhausgase um 85 % bis 90 % bis 2050—haben zu einem Aufschwung bei den nachhaltigen und regenerativen Energiequellen wie Photovoltaik, Windkraft und Biomasse geführt. Ein eng damit verknüpfter Ansatz ist die Nutzung von Niedertemperaturwärme aus industrieller Abwärme oder Geothermie. Obwohl diese Energiequellen in enormem Umfang nahezu kostenlos zur Verfügung stehen, gibt es aktuell keine einfachen aber effizienten Prozesse zur Verstromung dieser Niedertemperaturwärmequellen. Selbst die umfangreiche Forschung der letzten Jahre hat fast ausschließlich hochkomplexe, teure oder praktisch nicht umsetzbare Konzepte hervorgebracht. Diese Arbeit gibt einen Überblick über den aktuellen Stand der Technik und geht im Detail auf die thermodynamische und wirtschaftliche Untersuchung eines konkreten, vielversprechenden Batchverdampfungskreisprozesses ein: den MWM Prozess. Zunächst wird eine theoretische Untersuchung des instationären Prozesses auf Basis überarbeiteter Temperatur-Wärme- und Temperatur-Entropie-Diagramme präsentiert. Anschließend wird ein dynamisches Simulationsmodell vorgestellt, das Wärmetransport- und Massentransporteffekte sowie den Einfluss der thermischen Trägheit auf den instationären Prozess berücksichtigt. Abschließend folgt eine Wirtschaftlichkeitsanalyse, die auf Basis von statischen und dynamischen Ansätzen, allen voran die Annuitätsmethode, den Einfluss verschiedener Randbedingungen und Arbeitsmedien untersucht. Es konnte gezeigt werden, dass durch die instationäre Batchverdampfung eine nahezu perfekte Anpassung zwischen den Temperaturen von Arbeitsmedium und Wärmequellenmedium erreicht werden kann, ohne dass dafür aufwendige Komponente benötigt werden. Bei einer Temperatur von 100 °C liegt der Exergiewirkungsgrad des MWM Prozesses um 39 % über dem eines typischen ORC (ORC: $\eta_{\mathrm{II}} = 30.9\,\%$, MWM: $\eta_{\mathrm{II}} = 42.8\,\%$). Bezogen auf die Wirtschaftlichkeit zeigt sich jedoch, dass die Annuität des MWM Prozess das Niveau des ORCs nur erreichen kann, wenn die zunächst angesetzten reduzierten Betriebsstunden vernachlässigt werden (ORC: 26 500 €, MWM:

33 000 €, +25 %). Der abschließende Vergleich verschiedener Temperaturen, Arbeitsmedien und Erlösquellen zeigt, dass der MWM Prozess ein thermodynamisch vielversprechender und praktisch umsetzbarer Prozess ist. Für die reine Verstromung von Niedertemperaturwärmequellen ist er jedoch, wie auch der ORC, bei den hier betrachteten Strompreisen und regulatorischen Randbedingungen kaum wirtschaftlich zu betreiben.

Contents

List of Figures

List of Tables

Nomenclature

Abbreviations

ASHRAE	American Society of Heating, Refrigerating and Air-Conditioning Engineers	p. 23
CAPEX	Capital-Related Expenditures	p. 39
dPBT	dynamic Payback Time	p. 37
EEG	German: “Erneuerbare Energien Gesetz” (Renewable Energy Sources Act)	p. 111
ga	Genetic Algorithm	p. 47
GWP	Global Warming Potential	p. 21
HCFC	Hydrochlorofluorocarbons	p. 23
HX	Heat Exchanger	p. 19
IRR	Internal Rate of Return	p. 37
LCOE	Levelized Costs of Electricity	p. 144
LL	Liquid Level	p. 76
MWM	Maschinenwerk Misselhorn MWM GmbH	p. 34
NTU	Number of Transfer Units	p. 75
ODP	Ozone Depletion Potential	p. 21
OFC	Organic Flash Cycle	p. 29

η	Efficiency	[	-	] p. 7
Λ	Wavelength	[	m	] p. 199
λ	Thermal Conductivity	[	kW/(m·K)	] p. 74
ν	Kinematic Viscosity	[	m^2/s	] p. 198
Φ	Area Enlargement Factor	[	-	] p. 199
φ	Angle	[	°	] p. 199
ρ	Density	[	kg/m^3	] p. 65
σ	Surface Tension	[	N/m	] p. 201
τ	Dwell Time	[	s	] p. 79
ξ	Inverse Slope of Vapor Curve	[	kJ/(kg·K)	] p. 22

Indices

0	Reference State	p. 7
aux	Auxiliary	p. 8
av	Available	p. 9
avg	Average	p. 85
cond	Condenser, condensed	p. 88
eng	Expansion Engine	p. 54
exp	Expander, expanded	p. 54
fp	Feed Pump	p. 54
HS	Heat Source	p. 8
I	First Law (in context of efficiency)	p. 8
II	Second Law (in context of efficiency)	p. 9

in	Input / Ingoing	p. 8
int	Internal	p. 8
is	isentropic	p. 54
j	Counter for Time, e.g. Years (finan.) or Index of Timestep	p. 35
k	Index of Item, Component or Payment	p. 35
liq	Liquid Phase	p. 100
m	Mean Value	p. 7
n	Counter for Quantity and Space, e.g. n-th Replacement or Spatial Index	p. 39
net	Net Value	p. 8
out	Output / Outgoing	p. 8
vap	Vapor	p. 73
wall	wall properties	p. 74
WF	Working Fluid	p. 64

Latin Symbols

A	Area	[	m^2	]	p. 19
a	Amplitude of chevron structure	[	m	]	p. 79
a	Annuity Factor	[	-	]	p. 36
a	Thermal Diffusivity	[	m^2/s	]	p. 198
$A_{N,A}$	Annuity of Auxiliary Costs	[	€	]	p. 38
$A_{N,C}$	Annuity of Capital-Related Costs	[	€	]	p. 38
$A_{N,D}$	Annuity of Demand-Related Costs	[	€	]	p. 38

Chapter 1

Introduction

1.1 Framework

With the current efforts and discussions to reach the global climate target—reducing the greenhouse gases by 85 % to 90 % until 2050 (Umweltbundesamt [1])—all sectors are more than ever required to contribute. Mobility now seems to slowly shift to electrically powered cars and buses, households consume more and more "green" electricity and the industry satisfies the stricter limits and requirements. All of these approaches can basically be classified into two topics: Using sustainable and renewable energy sources and making the utilization of available resources more efficient.

The first part is already present in everyday life in the form of photovoltaic plants, wind farms and the first actually suitable electric cars. Even though the share of electric mobility is still small, the first steps have been made and the intermediate targets for 2012 had been accomplished [1]. According to the assessment of the Umweltbundesamt [1], also the targets for 2020 should be reached with regard to the reduction of greenhouse gases and the share of renewable energies. However, the second part seems more challenging. Most of our technologies, take for example the combustion engine, have already been used and optimized for generations and the remaining potential for improvement is small. The forecast of the Umweltbundesamt [1] predicts that additional effort is urgently needed in order to reach the goals for an increased energy efficiency in 2020 and 2030.

One promising field for an improved resource efficiency is the recovery of energy from low and medium temperature heat. This could for example be industrial waste heat from large–scale processes at moderate temperatures

like annealing furnaces and kilns, and drying processes (Lecompte et al. [2]). A higher temperature range is also available in the energy sector from the exhaust gases of gas turbines or internal combustion engines [2].

Campana et al. [3] specifically list cement, glass and steel industries to provide the most suitable processes. For all suitable cement plants in the EU27 countries, they estimate the potential for a total installed electric capacity of 576 MW_e. Depending on the operating hours per year, this corresponds to annual energy savings between 2.9 TWh and 4.6 TWh. Based on the electricity consumption of the European industries in 2010, about 0.46 % of the total energy consumption could be saved. Already back in 2005, Bailey and Worrell [4] also estimated the potential for an installed electric capacity for industrial waste heat recovery of 500 MW_e in Europe (EU12). Another 3.7 TWh to 6.0 TWh are estimated for the steel industry [3]. While the exhaust heat of gas turbines in the energy sector is often already used for combined heat–and–power concepts, Campana et al. [3] identify gas turbines in gas compressor stations and gas storage fields of the oil & gas industry as another major source for waste heat. Even without Russia, they predict 1300 MW_e in potential power capacity. With the base load stations working non–stop, an electricity generation of up to 10 TWh per year would be possible.

Combining these potential numbers of cement, steel, gas & oil and glass industry in Europe adds up to a total combined electricity production of over 20 TWh per year. The resulting reduction of 8.5 Mt of CO_2 corresponds to almost 2 % of the emissions of the European industry in 2010 [3] and also still in a similar range in 2017 (data by Umweltbundesamt [5]). While this is only a small share, especially compared to the total emissions of the energy sector (3368 Mt of CO_2-equivalents in 2017 [5]), every bit is needed in order to reach the goals for 2030 and 2050.

Another recent approach to unlock new sustainable energy sources is to tap into deep reservoirs of hot water and utilize this geothermal energy where the available temperatures are in the same range as for waste heat. Assuming the temperature range from 90 °C to 150 °C can fully be utilized, Quoilin et al. [6] give a potential electric capacity of about 9000 MW_e for Europe. Covering all temperature ranges up to 250 °C, Paschen, Oertel, and Grünwald [7] estimate the total technical potential for geothermal power production in Germany to be 300 PWh_e. With removing the hardly accessible 95 % of petrothermal resources, this still leaves a technical potential of about

15 PWh_e. Based on updated data, Eyerer et al. [8] estimate a technical potential for German hydrothermal geothermal energy of 12.2 PWh_e/a. Including the economic performance of current geothermal power plants and considering a sustainable exploitation rate further reduces the numbers, but still leaves an annual economic potential of 9.1 TWh_e/a.

1.2 Challenges of Waste Heat Utilization

The technically available amount of heat is impressive, but the challenge of the utilization of the low temperature levels can clearly be seen in the economically and ecologically usable share. In a few cases, the heat source can directly be used for heating. If a district heating network is already available, the heat could relatively simple be fed to the network. Still, the heating demand is limited and dependent on the seasons. For all other cases, the more versatile alternative is the power production.

The high efficiencies of common power plants are however bound to large scale superheated water–steam turbine cycles, which require high heat source temperatures and a complex setup. For the low temperatures and small scales, the thermodynamic limitations, temperature mismatch, and other losses have a much higher share on the total available energy. Even though the waste heat is a "free-of-charge" resource, special power cycles for low temperature applications are needed in order to even achieve a profitable investment. Almost all of them have in common that water is replaced by an organic working fluid. The lower boiling temperatures in these "Organic Rankine Cycles" (ORC) are better adapted to the low temperature heat sources.

With the rising demand for alternative cycle setups and the possibilities of sophisticated simulation tools, other variations have been widely discussed in literature for several decades now. Following the concept of the Kalina Cycle, first mentioned by Kalina [9] in 1984, scores of research can be found on mixtures of different working fluids in ORC–like cycles for an even better utilization of the heat sources and heat sinks. Other approaches shift the process to supercritical conditions (for example shown by Lecompte et al. [2] and Schuster, Karellas, and Aumann [10]) or delay the phase change of the working fluid to a late process phase in order to reach a better temperature match (as presented by Fischer [11] and Ho, Mao, and Greif [12]). Still, none

of these advanced cycles had a real breakthrough so far as all of them struggle with the practical implementation and the profitability compared to the conventional ORC.

1.3 Main Focus

This work focuses on another concept, the MWM Cycle. This batch evaporation power cycle also aims to efficiently recover low temperature heat sources. Its dynamic process behavior allows for a much better temperature match and higher efficiencies than a common ORC. The moderate requirements to the components allow for a practical implementation with standard components that are already available on the market. In return, the control of the transient process sequence and the more complex layout are more challenging than for the ORC.

In order to analyze, understand and evaluate the basic concept of this cycle, a dynamic simulation model is introduced. Covering the energy balances, the heat transfer and the thermal inertia, the feasibility of the concept is shown. Thermodynamically optimized cases for different heat source temperatures and with different working fluids are compared to the well-established ORC. In addition to the purely thermodynamic evaluation, an economic comparison between MWM Cycle and ORC is presented.

Chapter 2

Fundamentals

This chapter establishes the fundamentals and forms the base needed for later discussions. The first section defines efficiencies to rate power cycles and introduces the general challenges of low-temperature implementations. Furthermore, advanced cycle approaches are presented which try to solve these challenges. The theory behind the economic evaluation is given in section two. Section three compares different simulation approaches for thermodynamic process models which are widely used in literature.

2.1 Power Cycles for Low Temperature Applications

The definitions of low and medium temperatures differ widely in literature. Bianchi and Pascale [13] compare different bottoming cycles for "low temperature heat sources" in the range of 200 °C to 400 °C. Lower ranges are only mentioned as "very low temperatures" but were not further discussed. In extension to them, Dai, Wang, and Gao [14] use a heat source at 145 °C in their study of "low grade waste heat recovery". Geothermal energy resources are also commonly categorized as low temperature heat sources. The considered temperatures in the survey of Quoilin et al. [6] cover a range from 65 °C to 300 °C. According to DiPippo [15], the typical geothermal temperature range is around 150 °C. Irrespective of the exact temperature values, all authors agree that lower temperatures call for more advanced cycles. Instead of the operation of a classical Rankine Cycle, the medium-low temperature range is

normally handled by a simple Organic Rankine Cycle[1] (ORC) [6, 13, 14, 16] or sometimes a Kalina Cycle [15].

More recent studies focus mainly on the lower temperatures, where, according to Lecompte et al. [2], advanced cycle architectures have their foremost potential: they [2] evaluate a common ORC, a trilateral cycle and a transcritical ORC (TCORC) for waste heat recovery applications at low temperatures (100 °C to 150 °C), medium temperature (150 °C to 250 °C) and high temperatures (250 °C to 350 °C). The "low grade heat" source streams in the work of Andreasen et al. [17] represent geothermal and industrial waste heat sources at temperatures of 120 °C and 90 °C. Instead of pure working fluids, they screen different mixtures of refrigerants and hydrocarbons for improved efficiencies. Heberle and Brüggemann [18], as well as Preißinger, Heberle, and Brüggemann [19], also compare the performance of fluid mixtures to pure fluids in a geothermal application with low temperatures from 80 °C to 180 °C and 100 °C to 190 °C, respectively.

In accordance with the latter studies, the expression of *low temperature heat sources* is used for heat source temperatures from 100 °C to 150 °C in this work.

2.1.1 Definition of Cycle Efficiencies

The performance of a power cycle includes not only the gross power output but is dependent on its general operation purpose. In the context of a quantitative rating of the thermodynamic cycle performance, several efficiencies are used in literature.

Especially for low temperature applications, the concept of exergy analysis is used frequently [2, 12, 14, 15, 18, 20–22]. In contrast to energy based concepts, the exergy is defined as the maximum amount of work that can theoretically be gained from a heat source with regard to thermodynamic limitations. The specific exergy ex of a stream is defined by Baehr and Kabelac [23] as

$$ex = (h - h_0) - T_0 \cdot (s - s_0)\,, \tag{2.1}$$

where h and s are the specific enthalpy and the specific entropy of the stream, T is the temperature in Kelvin and the index 0 denotes the reference condition

[1] simple ORC: subcritical conditions and pure working fluids

for the exergy calculation. The lower reference for the exergy calculations T_0 (also known as dead state [2, 12, 15]) is in most cases set to ambient conditions or the properties of the heat sink.

Another often used method to quantify the potential of a heat source is the Carnot efficiency η_c of the ideal, reversible Carnot cycle. Though not being an actual thermodynamic cycle, this construct of four theoretical steps (two isentropic and two isothermal changes of state) marks the upper possible limit of the conversion from heat to work. The premise for the Carnot cycle is that heat is added and rejected at a constant upper and lower cycle temperature (T_{upper} and T_{lower}). The corresponding Carnot efficiency is defined by

$$\eta_c = 1 - \frac{T_{lower}}{T_{upper}}. \tag{2.2}$$

As derived by DiPippo [15], the relationship of a heat flow $\dot{Q}_T$ at the constant temperature T and the contained exergy flow $\dot{E}x_Q$ is also characterized by the Carnot efficiency η_c. When the cycle temperatures are matched to the temperatures of heat flow T and dead state T_0, respectively, it can be expressed by:

$$\dot{E}x_{Q_T} = \left(1 - \frac{T_0}{T}\right) \cdot \dot{Q}_T = \eta_c \cdot \dot{Q}_T. \tag{2.3}$$

However, when heat is transferred from a heat source stream to the cycle, the heat is generally not added at a constant temperature. In fact, the temperature of the heat source stream gradually decreases and the mean temperature T_m of heat transfer has to be used instead of the upper process temperature. According to Baehr and Kabelac [23], the mean temperature of heat transfer can be derived from the distribution of the heat flow over the temperature interval $\left(T_{high}, T_{low}\right)$ and follows as

$$T_m = \frac{h_{high} - h_{low}}{s_{high} - s_{low}} \approx \frac{T_{high} - T_{low}}{\ln\left(T_{high}/T_{low}\right)}. \tag{2.4}$$

When a heat flow $\dot{Q}_{T \to T_0}$ over a temperature interval from heat source temperature T to dead state T_0 is considered, the exergy content is calculated

as:

$$\dot{E}x_{Q_{T\to T_0}} = \left(1 - \frac{T_0}{T_\mathrm{m}}\right) \cdot \dot{Q}_{T\to T_0} = \eta_{\mathrm{c,m}} \cdot \dot{Q}_{T\to T_0}, \tag{2.5}$$

with

$$T_\mathrm{m} \approx \frac{T - T_0}{\ln\left(T/T_0\right)}. \tag{2.6}$$

This heat transfer over a temperature interval and the according efficiency, here called $\eta_{\mathrm{c,m}}$, can be represented by the theoretical Trilateral Cycle that will be further discussed in section 2.1.2 on page 10.

In summary, exergy based (or second law) efficiencies indicate more precisely the performance of the cycle itself rather than the limitation of the heat source. So to say, the cycle performance is rated against the ideal Carnot efficiency for the given temperature levels. However, energy based (or first law) efficiencies can be of better use for the analysis of energy conversion and utilization.

In a closed loop heat source, any heat that is not transferred to the cycle just remains in the loop and can still be utilized later on. A common example are solar power applications with an intermediate heat transfer oil loop, where normally the internal cycle efficiency is maximized [6]. For the so called thermal efficiency or internal first law efficiency

$$\eta_{\mathrm{I,int}} = \frac{P_\mathrm{out} - P_\mathrm{aux}}{\dot{Q}_\mathrm{in}} = \frac{P_\mathrm{net}}{\dot{Q}_\mathrm{in}}, \tag{2.7}$$

the net power output P_net is set in relation to the heat flow that is actually transferred from the heat source to the cycle $\dot{Q}_\mathrm{in} = \dot{m}_\mathrm{HS} \cdot c_p \left(T_{\mathrm{HS,in}} - T_{\mathrm{HS,out}}\right)$. The auxiliary power P_aux combines the power demand for the feed pump of the working fluid and the power demand for the compensation of pressure losses of heat source and heat sink.

Accordingly, for the exergetic analysis, the net power is set in relation to the exergy flow $\dot{E}x_\mathrm{in} = \dot{m}_\mathrm{HS}\left(ex_{\mathrm{HS,in}} - ex_{\mathrm{HS,out}}\right)$ that is transferred from the heat source to the cycle. The internal second law efficiency is defined as:

$$\eta_{\mathrm{II,int}} = \frac{P_\mathrm{out} - P_\mathrm{aux}}{\dot{E}x_\mathrm{in}} = \frac{P_\mathrm{net}}{\dot{E}x_\mathrm{in}}. \tag{2.8}$$

Both internal efficiencies account for the internal power demand P_{aux} and the efficiency of the expansion machine. Furthermore, the transferred heat flow and exergy flow refer to the flow released from the heat source rather than to the amount added to the working fluid. Any losses and irreversibility during heat transfer are therefore also covered by this definition.

In case of an open heat source, any heat that is not transferred to the cycle is lost. In many waste heat recovery (WHR) applications, the original heat source (for example exhaust gas) is cooled down and then discarded to the environment or further treatment. Therefore, it is important to add the heat transfer efficiency to the overall consideration. The objective should then be a maximized power output or maximized system efficiency [6].

The heat transfer efficiency or external first law efficiency

$$\eta_{\text{I,ext}} = \frac{\dot{m}_{\text{HS}} \cdot c_p \left(T_{\text{HS,in}} - T_{\text{HS,out}}\right)}{\dot{m}_{\text{HS}} \cdot c_p (T_{\text{HS,in}} - T_0)} = \frac{\dot{Q}_{\text{in}}}{\dot{Q}_{\text{av}}}, \tag{2.9}$$

is the ratio of the actually transferred heat flow $\dot{Q}_{\text{in}}$ to the totally available heat flow $\dot{Q}_{\text{av}}$.

In terms of exergy analysis, the external second law efficiency is defined accordingly as

$$\eta_{\text{II,ext}} = \frac{\dot{m}_{\text{HS}} \cdot \left(ex_{\text{HS,in}} - ex_{\text{HS,out}}\right)}{\dot{m}_{\text{HS}} \cdot (ex_{\text{HS,in}} - \underbrace{ex_{\text{HS,0}}}_{=0})} = \frac{\dot{E}x_{\text{in}}}{\dot{E}x_{\text{av}}}, \tag{2.10}$$

where, following the definition of exergy in eq. (2.1) on page 6, the exergy at reference conditions equals $ex_{\text{HS,0}} = 0$.

The combination of internal and external efficiency (eqs. (2.7) and (2.9)) leads to the system efficiency or overall first law efficiency

$$\eta_{\text{I}} = \eta_{\text{I,int}} \cdot \eta_{\text{I,ext}} = \frac{P_{\text{net}}}{\dot{Q}_{\text{in}}} \cdot \frac{\dot{Q}_{\text{in}}}{\dot{Q}_{\text{av}}} = \frac{P_{\text{net}}}{\dot{Q}_{\text{av}}}. \tag{2.11}$$

The second law eqs. (2.8) and (2.10) lead to the exergetic system efficiency or

(overall) second law efficiency

$$\eta_{\mathrm{II}} = \eta_{\mathrm{II,int}} \cdot \eta_{\mathrm{II,ext}} = \frac{P_{\mathrm{net}}}{\dot{E}x_{\mathrm{in}}} \cdot \frac{\dot{E}x_{\mathrm{in}}}{\dot{E}x_{\mathrm{av}}} = \frac{P_{\mathrm{net}}}{\dot{E}x_{\mathrm{av}}}. \tag{2.12}$$

These system efficiencies indicate the fraction of the total available heat and exergy, respectively, that is converted to accessible net power output. The maximized (net) power output, as demanded by Quoilin et al. [6] for open heat sources, is therefore equivalent to a maximized system efficiency (eqs. (2.11) and (2.12)).

2.1.2 Thermodynamic Approach

Theoretical Cycles As already mentioned in section 2.1.1, the common benchmark for cycle performance is the ideal, reversible Carnot Cycle. However, the assumption of heat being available at a constant temperature level is only applicable in rare occasions. Typical examples are a directly fired heater at constant flame temperatures or a condensing heat source, and a large condenser with a virtually constant temperature. In operation with heat source and heat sink in form of streams, the heat transfer will always take place over a temperature interval (see fig. 2.1 on the facing page). This temperature mismatch will therefore limit the efficiency of the basic Carnot Cycle η_{c} (eq. (2.2) on page 7) to a somewhat lower process temperature rather than the maximal heat source temperature T. In fact, the temperatures for the Carnot calculations have to be even further reduced to the interval ($T_{\mathrm{high}} \rightarrow T_{\mathrm{low}}$) due to the finite temperature differences needed for heat transfer:

$$\left(\eta_{\mathrm{I,int}}\right)_{\mathrm{Carnot}} = \left(1 - \frac{T_{\mathrm{low}}}{T_{\mathrm{high}}}\right) \ll \left(1 - \frac{T_0}{T}\right). \tag{2.13}$$

Accordingly, the shown 80 °C-cycle in fig. 2.1 only has an internal efficiency of $\left(\eta_{\mathrm{I,int}}\right)_{\mathrm{Carnot}} = 12.7\,\%$ instead of the 20.1 % the temperature spread $T \rightarrow T_0$ would suggest.

In addition, the temperature level of the heat addition and the temperature mismatch also strongly affect the amount of utilized heat (heat transfer efficiency $\eta_{\mathrm{I,ext}}$ eq. (2.9)). Therefore, also the overall system efficiency η_{I} (eq. (2.11))

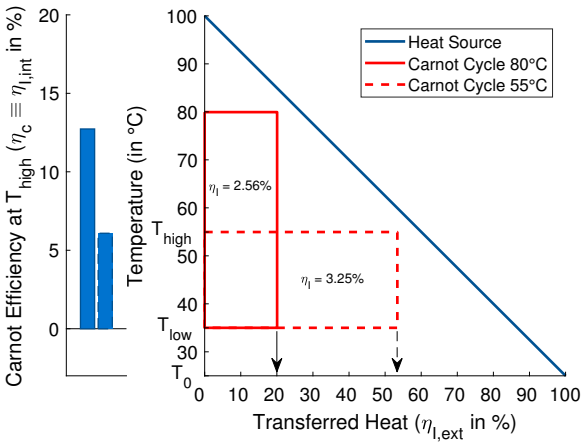

Figure 2.1: Efficiencies of two exemplary Carnot cycles ($T_{\text{high}} \rightarrow T_{\text{low}}$) with a heat source stream at 100 °C.

and the net power output are dependent on the temperature level. The auxiliary power P_{aux} and engine efficiency are neglected for these theoretical considerations.

Figure 2.1 shows the relationship of the heat transfer temperature and the efficiencies of the Carnot cycle in a commonly used temperature-heat-diagram (T-Q-diagram). Here, the x-axis corresponds to the heat that is available from the heat source stream. Transferring all the available heat and therefore cooling down the heat source to the reference temperature T_0 would be equal to an external first law efficiency of $\eta_{\text{I,ext}} = 100\,\%$. Thus, these diagrams are especially suited to visualize the ability of a power cycle to utilize a given heat source and are therefore perfect for the following discussion.

On one hand, a high process temperature allows for a high cycle efficiency as indicated by the bars on the left. On the other hand, it limits the accessible fraction of heat as displayed on the x-axis. Being the product of cycle efficiency and heat transfer efficiency, the total system efficiency is proportional to the area that is covered by the Carnot Cycle in the T-Q-diagram. The power output of the cycle is directly coupled to this overall system efficiency and it can be seen that a higher internal cycle efficiency does not implicitly lead to a

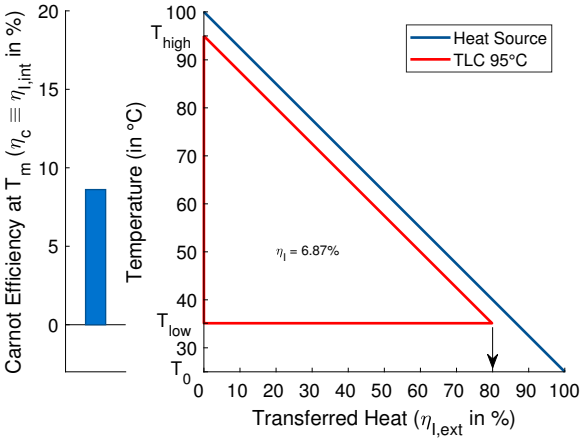

Figure 2.2: Efficiencies of an exemplary trilateral cycle ($T_\mathrm{m} \rightarrow T_\mathrm{low}$) with a heat source stream at 100 °C.

higher power output.

It becomes clear from fig. 2.1 on page 11 that the Carnot cycle is not always the perfect benchmark for heat source streams. While it still marks the maximal possible internal cycle efficiency, it cannot reach a high utilization of the heat source at the same time. Figure 2.2 shows the—also theoretical but much better fitted—Trilateral Cycle (TLC). In the TLC, the heat transfer to the cycle is implemented at a gliding temperature. This reduces the possible internal cycle efficiency compared to the previous Carnot examples, but allows for an almost perfect temperature match of heat source and working fluid. In this cycle, the maximal possible internal efficiency is calculated with the mean temperature of heat transfer T_m that was already introduced in eq. (2.4) on page 7

$$\left(\eta_{\mathrm{I,int}}\right)_{\mathrm{TLC}} = \left(1 - \frac{T_\mathrm{low}}{T_\mathrm{m}}\right) \ll \left(1 - \frac{T_0}{T}\right). \tag{2.14}$$

and is reduced to about the half of the Carnot efficiency at the process temperature T_high in eq. (2.13) on page 10. At the same time, the heat transfer efficiency is remarkably higher and the overall system efficiency surpasses

those of the Carnot examples.

Again, the system efficiency is proportional to the area that is covered by the process in the T-Q-diagram. If all the necessary temperature differences were neglected ($T_{\text{high}} = T$ and $T_{\text{low}} = T_0$), the TLC would exactly fit the heat source. According to the definition of exergy, the full exergy potential could then be converted to power by the cycle: Comparing the exergy content of the heat source stream (according to eq. (2.5) on page 8) and the Power output of the TLC (according to eq. (2.11) on page 9) proves the full conversion of the available exergy and verifies that a second law efficiency of $\eta_{\text{II}} = 100\,\%$ would be accomplished:

$$\dot{E}x_{Q_{T\to T_0}} \stackrel{?}{=} P_{\text{TLC}} \tag{2.15}$$

$$\left(1 - \frac{T_0}{T_{\text{m}}}\right) \cdot \dot{Q}_{T\to T_0} = \underbrace{\left(\eta_{\text{I,int}}\right)_{\text{TLC}}}_{\text{eq. (2.14)}} \cdot \underbrace{\eta_{\text{I,ext}}}_{100\,\%} \cdot \dot{Q}_{\text{av}} \tag{2.16}$$

$$\text{with } T_{\text{low}} = T_0 \Rightarrow \qquad \left(1 - \frac{T_0}{T_{\text{m}}}\right) \cdot \dot{Q}_{\text{av}} = \left(1 - \frac{T_0}{T_{\text{m}}}\right) \cdot \dot{Q}_{\text{av}} \tag{2.17}$$

$$\dot{E}x_{Q_{\text{av}}} = P_{\text{TLC}} \qquad \boxtimes \tag{2.18}$$

In reverse, this allows not only the conclusion that the area covered by the cycle graph represents the power output, but also that the total area under the heat source graph visualizes, to good approximation, the total exergy content of the heat source stream.

Organic Rankine Cycle As already mentioned, the Carnot Cycle and the Trilateral Cycle are just theoretical standard cycles. They both represent, in their own way, the ideal adaption to the heat source. At a given temperature:

- the Carnot Cycles marks the maximal possible internal efficiency
- the TLC marks the maximal possible system efficiency.

With regard to real applications, the Rankine Cycle for high temperatures and the Organic Rankine Cycle (ORC) for medium and low temperatures are the common choices. While the standard Rankine cycle is operated with water as a working fluid, the lower boiling point of organic fluids in the ORC perfectly

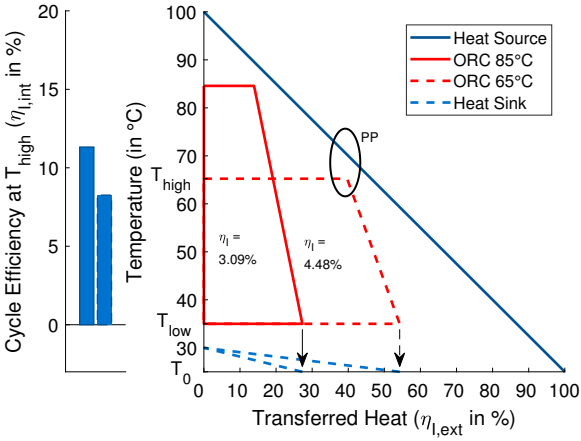

Figure 2.3: Efficiencies of two exemplary Organic Rankine Cycles ($T_{\text{high}} \rightarrow T_{\text{low}}$) with a heat source stream at 100 °C.

fits lower heat source temperatures. With the focus on low temperature applications, the further discussion will only consider the "Organic" variation of the Rankine Cycle.

Figure 2.3 shows two exemplary Organic Rankine Cycles. In contrast to the Carnot cycle, the isothermal phases are here replaced by more viable isobaric phases. This results in the typical two parts of heat input: The rising temperature during the preheating of the working fluid and the constant temperature during the boiling phase. The distinctive kink at the intersection of these two parts always marks the onset point of boiling. For many (but not all) configurations, this kink is also the position of the smallest temperature difference between heat source and working fluid. This smallest but finite temperature difference, the so called "pinch point" (PP), is necessary in order to assure a finite heat exchanger area and is one of the design specifications of an ORC. In addition to the pinch point in the evaporator, the figure also shows the heat sink streams and the pinch point in the condenser (smallest temperature difference at $\eta_{\text{I,ext}} = 0\,\%$).

Again, an optimum between a high internal and external efficiency has to be found due to the temperature mismatch of working fluid and heat source.

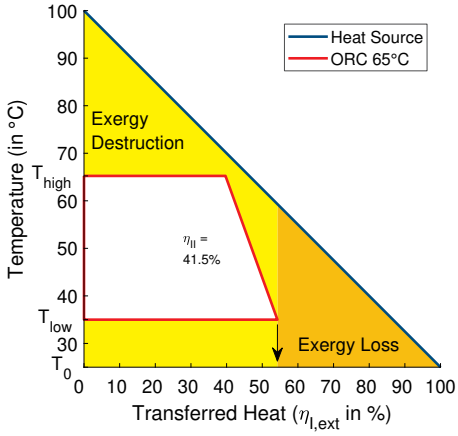

Figure 2.4: Exergy distribution in an exemplary Organic Rankine Cycle with a heat source stream at 100 °C.

Like for the Carnot Cycle and the TLC, the system efficiency of the ORC is proportional to the area that is covered by the process in the T-Q-diagram. There it was furthermore shown that the area under the heat source graph represents the available exergy. While the first law efficiencies $\eta_{I,int}$ and $\eta_{I,ext}$ are represented on the axes of the previous figure, the second law efficiencies and losses can be directly visualized by areas in the T-Q-diagram (see fig. 2.4).

In fig. 2.4, the orange sector is unused, lost exergy. Compared to the corresponding amount of lost *heat* in the first law analysis (shown on the x-axis), this low-temperature corner of the heat source contains only a small amount of lost *exergy*. Consequently, the external second law efficiency $\eta_{II,ext} = 77\,\%$ is bigger than its first law counterpart with only $\eta_{I,ext} = 54\,\%$. This relationship puts emphasis on the fact that low-temperature heat is less valuable than the same amount of heat at a higher temperature.

In addition, the yellow areas between the cycle and the heat source / heat sink streams represents destroyed exergy. When heat is transferred from a hot stream to a colder stream (for example from heat source to working fluid) some amount of exergy is destroyed. Although the energy content is conserved during this heat transfer, the lower-temperature heat flow that

reaches the target stream contains less work potential. Therefore, in addition to the exergy losses, exergy is destroyed in all the introduced thermodynamic cycles due to the necessary finite temperature difference during heat transfer and due to the mismatch of the temperature profiles of heat source and cycle.

The fraction of the white cycle area on the whole area under the heat source equals what is left of the available exergy. It is also directly linked to the overall second law efficiency $\eta_{\mathrm{II}} = 42\,\%$.

In summary, it can be said that the areas in the T-Q-diagram (fig. 2.4 on page 15) represent, in good approximation, the following shares of exergy:

- The whole area under the heat source stream represents the **available exergy** of the heat source Ex_{av}.
- The bottom corner to the right of the cycle (orange area) visualizes the part of **exergy losses**. The whole other part is the amount of exergy that is actually transferred to the cycle Ex_{in}.
- The parts between heat source and cycle and between cycle and reference temperature T_0 (yellow areas) visualize the **exergy destruction** due to temperature differences during heat transfer.
- Only the part within the graph of the process (white area) represents the actual **power output** of the cycle P_{out} and the **overall second law efficiency** η_{II} (note: the auxiliary power demand is not considered here, therefore $P_{\mathrm{out}} = P_{\mathrm{net}}$).

Challenges in Low-Temperature Applications Based on the concept of exergy, the challenges for low-temperature cycles become clear.

First, the accessible fraction of work from the heat source is already small compared to high temperature heat sources. The comparison in table 2.1 on the next page shows that an exemplary low-temperature heat source with an available heat flow of 1 MW provides only about 21 % of the exergy that is stored in its high temperature equivalent. The following calculations are based on dry air at a pressure of 4 bar. Other fluids, like water or steam, show less distinct, but otherwise similar results. Effects like phase changes and supercritical conditions would complicate the comparison over this wide

Table 2.1: Comparison of the exergy content of an exemplary low temperature and high temperature, gaseous heat source with a heat flow of 1 MW(dry air, $T_0 = 25\,°C$).

Temperature T in °C	Mass Flow $\dot{m}$ in kg/s	Energy E in kW	Exergy Ex in kW
800	1.20	1000	515
100	13.18	1000	108

Table 2.2: Exergy losses due to the pinch point in evaporator and condenser and due to temperature mismatch of working fluid and heat source / heat sink for an exemplary low- and high-temperature, gaseous heat source (dry air, $T_0 = 25\,°C$).

Heat Source Temperature			100 °C		800 °C	
		Unit	value	fraction	value	fraction
Working Fluid			R134a		water	
Evap. Pressure		(bar)	19		90	
Exergy content		(kW)	108	100 %	515	100 %
Exergy losses	PP Evap.	(kW)	8	7 %	2	<1 %
and destruction	PP Cond.	(kW)	10	9 %	9	2 %
relating to total	Heat Sink	(kW)	10	9 %	9	2 %
exergy content	Heat Source	(kW)	35	32 %	132	26 %
Turbine Power		(kW)	45	42 %	363	70 %

temperature range. Therefore, dry air is used here as a simple model heat source.

Second, the necessary temperature difference in the pinch point has a greater impact on the already limited available work potential. A descriptive example is given in table 2.2 based on the the above 1 MW heat source and the exemplary ORC that was already used in figs. 2.3 and 2.4. A simple shortcut simulation was used in order to compute the ORC with and without the exergy losses and destruction (see appendix A.1 on page 187 for more details about

the shortcut model). When reducing the pinch point in the evaporator to almost 0 K, the shortcut simulations showed that about 7 % of the available exergy are destroyed due to the original pinch point. Another 9 % have to be accounted to the pinch point in the condenser. The rising temperature of the heat sink stream is blocking additional 9 %. Even though the absolute numbers are in the same order of magnitude for the high temperature example, their percentage on the total available exergy of about 2 % each is almost negligible.

The third part, however, is a major source for exergy destruction in both cases. The temperature mismatch between heat source and working fluid limits the possible mass flow of the working fluid cycle and prevents the perfect utilization of what exergy is left after the pinch point and heat sink limitations. Similar to the Carnot Cycle, the previously shown ORC examples do simply not fit the heat source as perfectly as the TLC would. Therefore, the exergy destruction due to a temperature mismatch is about 30 % in both examples (high and low temperature).

After all the exergy losses and exergy destruction, the actually used exergy of the low temperature example cycle is only 45 kW, which leads to the already mentioned exergetic system efficiency of $\eta_{\mathrm{II}} = 45\,\mathrm{kW}/108\,\mathrm{kW} = 42\,\%$. Even compared to the, here neglected, engine losses of about 20 %, the heat transfer in evaporator and condenser accounts for the major fraction of destroyed exergy. Mago et al. [20] also show in their more detailed exergy analysis that "[…] the evaporator is the component with the highest influence coefficient and highest exergy loss with respect to the overall system exergy loss". Keeping in mind that this is not a constraint of the components, but rather a thermodynamic limitation, illustrates the importance of a well-suited cycle for low-temperature applications.

2.1.3 Cycle Setup

To maintain a competitive setup with the small amount of available exergy at low temperatures, extra effort is necessary in order to minimize all losses as far as possible. In contrast, the substantial amount of available exergy from a high temperature heat source may allow for simpler solutions in favor of reduced investment costs. The approaches to deal with the flaws in heat transfer are discussed in the following paragraphs.

2.1.3.1 Operational Cycle Setup

Pinch Point Obviously, the losses due to the pinch point in the evaporator and condenser can be reduced by simply reducing the minimal necessary temperature difference. The heat flow $\dot{Q}$ in these heat exchangers (HX) is subject to the heat transfer area A, the total heat transfer coefficient k and the temperature difference ΔT by

$$\dot{Q} = k \cdot A \cdot \Delta T. \tag{2.19}$$

Thus, a reduced temperature difference needs an increased heat transfer area or an improved heat transfer coefficient in order to maintain the heat flow. When it comes to an economic evaluation, the additional investment costs for bigger or more complex heat exchangers will at some point outbalance the gains from the better thermodynamic cycle performance. Still, reducing this limit does actually increase the amount of accessible exergy.

Literature shows that a temperature difference at the pinch point of 5 K to 10 K is a common initial guess for the design phase [2, 13, 14, 18] and also matches the results of economic optimizations [24].

Evaporation Pressure The selection of the appropriate evaporation pressure is the most direct, but less versatile parameter. In contrast to the following structural cycle design and the fluid selection, the pressure level can be adjusted even during operation (within a certain range). However, this measure is limited in its potential of actually increasing the accessible exergy. It was already shown in the Carnot and ORC example cycles that the selected evaporation pressure rather shifts the balance between internal and external cycle efficiency. In order to maximize the overall cycle efficiency, an optimum at an intermediate pressure has to be found. Figure 2.5a on the following page shows the influence of the evaporation pressure on the different efficiencies. It can be seen that the internal and external efficiency follow an opposed dependency. The arrows mark the pressure levels for a high external efficiency, a maximized internal efficiency and a maximized overall efficiency, respectively.

A high evaporation pressure limits the transferred exergy $\dot{Ex}_{\mathrm{in}}$ and causes a great amount of lost exergy (see fig. 2.5b, 28 bar). At the same time it provides a boiling temperature close to the heat source temperature and keeps the

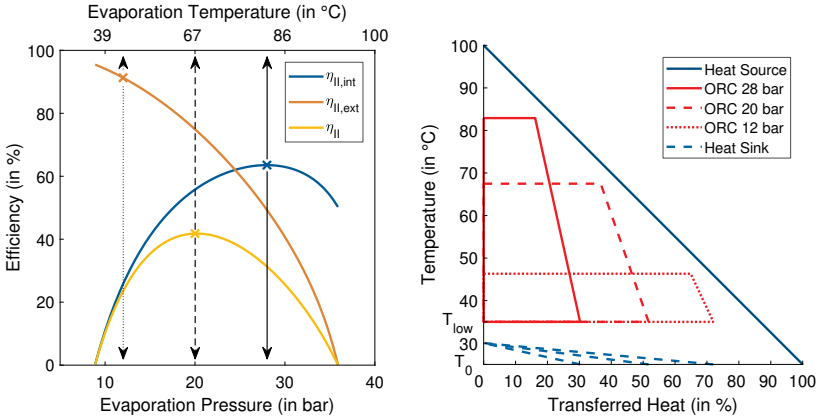

(a) Influence of evaporation pressure on cycle efficiencies

(b) Temperature match for three characteristic evaporation pressures

Figure 2.5: Performance of an Organic Rankine Cycle at different operation points.

exergy destruction small. The great pressure drop and high specific enthalpy difference over the expansion engine lead to a maximized internal efficiency. The absolute power output is still limited, because only a small fraction of the available exergy is transferred at all. The high pressure allows for a low mass flow of working fluid. Thus, the high internal efficiency comes along with only moderately sized heat exchangers and expansion engine, but does need a more expensive feed pump to reach the high pressure (Quoilin et al. [24]). For very high pressures, close to the critical point of the working fluid, the effort for a further increased boiling temperature will hardly improve the specific enthalpy, and therefore the internal efficiency will decline again.

A low evaporation pressure allows utilizing almost all the available exergy (see fig. 2.5b, 12 bar). The low evaporation temperature, however, leads to great temperature differences during heat transfer and causes exergy destruction. Despite the high external efficiency and great amount of transferred exergy, the small pressure and enthalpy difference over the expansion engine can only provide a very limited power output. Furthermore, a high mass flow

of working fluid is necessary to carry all the transferred exergy and bigger equipment (heat exchangers and expansion engine) are needed. A smaller feed pump is sufficient for the low pressure level, though.

The operation point of maximized power output is always a trade off between these two extreme cases. The 20 bar example in fig. 2.5b shows how the combination of two medium values for internal and external efficiency lead to a maximized overall cycle efficiency. However, there is still a considerable fraction of both exergy destruction and exergy losses due to the temperature mismatch, even in this optimal case.

In summary, it can be said that it is essential to choose the right evaporation pressure for each working fluid and heat source temperature.

Working Fluid While the pressure level only gives a variable to shift between high internal and external efficiencies, the selection of a matching working fluid actually allows the process to better fit the heat source. All previous ORC examples were presented with R134a as working fluid in order to first analyze the influence of all other factors independently of the working fluid selection.

Extensive research can be found in literature about the selection of the perfect working fluid. The screening for proper fluids always starts with categorizing them by the following properties:

- Critical temperature of the fluid and other thermodynamic properties
- Dry, wet or isentropic fluid
- Environmental impact, in specific: global warming potential (GWP) and ozone depletion potential (ODP)
- Safety issues (AHSRAE classification).

Commonly presented fluids are hydrocarbons, halogenated hydrocarbons, amines and ether. Many fluids used in refrigeration are also suitable for a reversed application in a low-temperature power cycle. After a preselection according to safety and environmental regulations as well as general thermodynamic properties, the actual evaluation is mostly done by running full cycle simulations on the remaining fluid candidates [2, 17, 24–26]. Researchers

like Liu et al. [25] try to further reduce this number during preselection by theory-based prediction approaches for the "optimal heat source temperature (OHST)". In the end, there barely is one single optimal working fluid. The final choice depends on all the reference conditions and on the question, if the goal is a thermodynamic or economic optimization.

Basic selection criteria for working fluids, with regard to the above summarized categories, are:

- The thermodynamic properties of the fluid should match the available temperature range: The fluid has to be condensable at the temperature of the heat sink. The condensation pressure should meanwhile neither be too high (cost of high–pressure equipment) nor be in partial vacuum (reliability and complexity of sealing effort) (Chen, Goswami, and Stefanakos [27]). Depending on the choice of cycle setup, sub-critical or trans-critical (see section 2.1.3.2), the critical temperature of the working fluid should match the heat source temperature accordingly. As a "rule of thumb", the best–performing fluids at a certain heat source temperature show a critical temperature close to the heat source (He et al. [28]). A moderate evaporation pressure also works in favor of lower equipment costs.

- The type of the fluid can be defined by the slope of the saturated vapor curve in a T-s-diagram ($\mathrm{d}T/\mathrm{d}s$). Examples for all three types are shown in fig. 2.6 on the next page. Chen, Goswami, and Stefanakos [27] recommend using the inverse slope $\xi = \frac{1}{\mathrm{d}T/\mathrm{d}s}$ in order to avoid an infinite value for vertical sections. In general, they do not recommended to use wet fluids ($\xi < 0$) because of the danger to form droplets in the turbine when expanding into the two-phase region. Wet fluids therefore always require putting additional effort into superheating the fluid. Dry fluids ($\xi > 0$) are always a safe choice in this regard, but the remaining superheat after expansion adds to the exergy destruction. Isentropic fluids ($\xi \approx 0$) show the best suitability, but they are not available for all temperature ranges.

- Many thermodynamically suitable fluids have already been phased out due to environmental issues. Fluids which show any form of ozone depletion potential, the so called HCFCs, are already banned by the

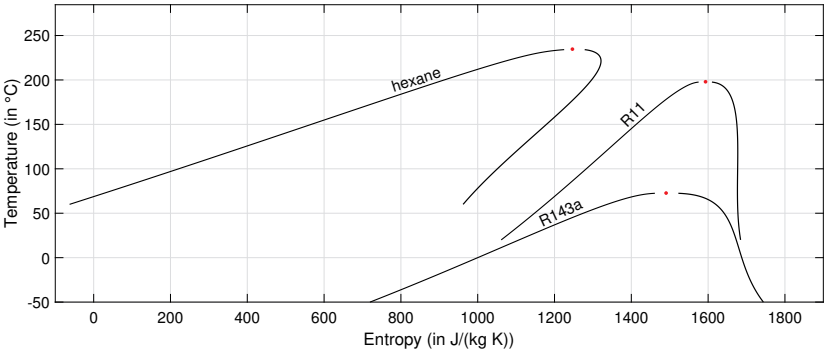

Figure 2.6: Examples for a wet (R143a), dry (hexane) and isentropic (R11) fluid in the T-s-diagram.

Montreal Protocol. Furthermore, the limits for the tolerated global warming potential will be further reduced over the next years. Therefore, Lecompte et al. [2], for example, only consider fluids with a GWP lower than 150 in order to comply with the F-gas regulations.

- The "American Society of Heating, Refrigerating and Air-Conditioning Engineers"(ASHRAE) classification is a good indicator for the practical applicability of a working fluid. According to their flammability and toxicity, they are categorized from A1 (non-flammable, non-toxic) to B3 (highly flammable, toxic):

	Non-Flammable	Flammable	Highly Flammable
Non-Toxic	A1	A2	A3
Toxic	B1	B2	B3

While the toxicity is a criterion for exclusion, a flammable but otherwise uncritical fluid (like the saturated hydrocarbons) may still be a suitable candidate.

The conflict between safe, environmentally uncritical fluids and a high performance drives the research on new working fluids. Although there is progress

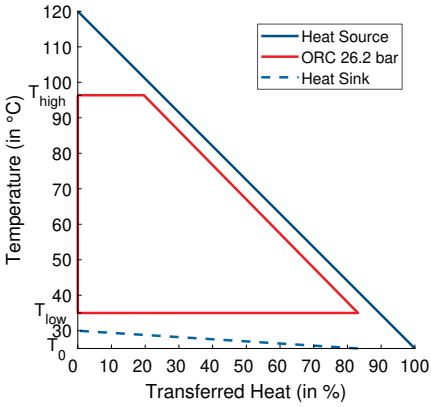

Figure 2.7: Perfect temperature match of an ORC (working fluid: R227ea) to a heat source at 120°.

in the direction of only partly fluorinated hydrocarbons, the long-term stability and compatibility with other materials is still under research (see for example Eyerer et al. [29]).

Following the prediction method of Liu et al. [25], a matching working fluid for a 120 °C heat source would be R227ea. Even though R227ea is not recommended anymore due to its high GWP of over 3000, fig. 2.7 shows the temperature match of such an ORC. The additional potential of the higher heat source temperature itself (120 °C vs. 100 °C) is already compensated by the usage of exergetic efficiencies. Beyond that, this perfectly matching working fluid would allow for a theoretical second law efficiency of $\eta_{II} = 61\,\%$ (R134a at 100 °C: $\eta_{II} = 42\,\%$). The predicted 61 % are overestimated by the error of the shortcut model when used close to critical temperatures of the working fluid. The comparison to R134a, as known from the reference cycles in section 2.1.2, still justifies the motivation for the ongoing research on matching working fluids for various applications.

Nevertheless, Quoilin et al. [6] see the lower limit for economic power generation at 80 °C. Lecompte et al. [2] even state that there are no high performance fluids for heat source temperatures at and below 100 °C that comply with current environmental restrictions. Liu et al. [25] also only show

fluids with an optimal heat source temperature over 120 °C (except for R218 which shows a very high GWP of almost 9000). Others completely skip the low temperature range and only consider the more yielding medium temperature sources, like Bianchi and Pascale [13] in their work on ORCs starting from 200 °C.

2.1.3.2 Structural Cycle Setup of Advanced Cycles

Further improvement over the previous operational methods is only possible by adjusting the structural characteristics of the ORC and by introducing new, advanced cycle setups:

Transcritical ORC One approach to reduce the losses during heat transfer is to increase the evaporation pressure up to critical conditions. Schuster, Karellas, and Aumann [10] give a good introduction to these supercritical cycles. Close to the critical point of the working fluid, the distinction between liquid and vapor phase vanishes. Without the characteristic kink at the transition from pre-heating to evaporation in the boiling curve, the temperature match can be improved (see fig. 2.8a on the next page) and higher system efficiencies are possible. Both Schuster, Karellas, and Aumann [10] and Lecompte et al. [2] predict an improvement in system efficiency of about 10 % over a subcritical ORC. For low-temperature applications, the condensation typically takes place under subcritical conditions and these cycles should therefore, more correctly, be called transcritical cycles [2].

The typical example, a supercritical CO_2 cycle, however, comes at operation conditions of 60 bar to 160 bar and requires extended safety measures [27]. Bianchi and Pascale [13] also raise concerns that the extra effort in order to handle all kinds of supercritical fluids "could be questionable" for small scale applications. Especially the design of turbomachinery for supercritical conditions proves to be problematic and is still subject to current research (Cho et al. [30]). In addition, the reduced heat transfer to supercritical fluids (Karellas, Schuster, and Leontaritis [31]) and the high pressure in the turbine cause higher costs for the components which are usually not completely compensated by the increased power output (Oyewunmi et al. [32]).

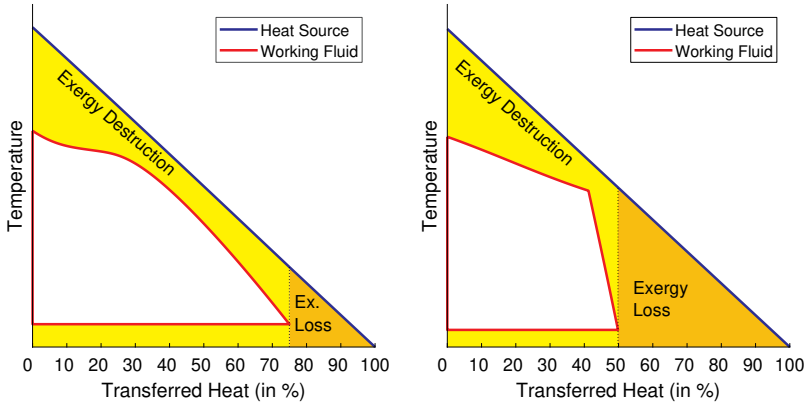

(a) Transcritical ORC (b) Zeotropic ORC

Figure 2.8: Exemplary temperature matches in advanced cycle structures.

Kalina Cycle and Zeotropic Mixtures Another way to overcome the phase of constant temperature during boiling is to use a mixture of working fluids. With a zeotropic mixture, the low boiling component will evaporate first and the less volatile part will accumulate in the residue. Therefore, a temperature glide will occur during the evaporation phase (see fig. 2.8b).

The most famous mixture is water/ammonia in the so called Kalina Cycle (named after Kalina [9], who first introduced this concept). In this cycle, the high-boiling water is hardly evaporated at all and acts merely as transport carrier for the ammonia. Consequently, the two phases have to be separated before the ammonia-rich vapor is expanded in the turbine. Separating and mixing of the two streams requires additional components and adds extra costs and complexity. Numerous modifications, adjustments and reviews have therefore been published ever since derived from the original Kalina Cycle [e.g. 15, 22, 33, 34]. With regard to the toxicity of ammonia, current research focuses on suitable combinations of already known and harmless working fluids. Mixtures of fluids with close boiling points, like isobutane and isopentane, show only a limited temperature glide. On the other hand they can both be completely evaporated and the required setup therefore hardly

differs from a common ORC.

DiPippo [15] criticizes that, due to the better temperature match in the Kalina Cycle, claims about an improvement in the cycle efficiency of over 40 % were made. However, despite this dramatic theoretical advantage, the difficulties in practical application become obvious when looking for actual Kalina plants in operation. According to the calculations of DiPippo [15], the effective second law efficiency of the Kalina power plant in Húsavík, Iceland, is only $\eta_{II} = 23.1\,\%$ at a heat source temperature of 120 °C. One of the few other commercial Kalina power plants in Unterhaching, Germany [35], already shut down their power production in 2017 and now uses the geothermal resources exclusively for district heating [36].

In contrast, the work of Heberle, Preißinger, and Brüggemann [37] predicts an increase of the second law efficiency up to 15 % for mixtures of R227ea / R245fa and isopentane / isobutane for heat source temperatures below 120 °C. Pure components can only keep up with mixtures when their properties perfectly align with the heat source temperature (like seen for R227ea in fig. 2.7 on page 24). As there are only so many different working fluids and matching temperatures (see Liu et al. [25]), the use of zeotropic mixtures will allow for a better adaption and a higher cycle performance in most cases. Complications in the practical application like for the Kalina Cycle are not expected due to the comparably simple setup. Heberle and Brüggemann [18] confirm an efficiency increase up to 20 % for zeotropic mixtures over the most efficient pure working fluid. However, they admit that the drastically reduced heat transfer coefficients for fluid mixtures depletes this advantage. While the increased power output for higher temperatures (160 °C) still overcompensates the additional heat transfers surfaces, the most economic selection for lower temperatures (120 °C) is R227ea as pure fluid. Andreasen et al. [17] also come to an increased net power of about 13 % when using zeotropic mixtures, but affirm the expected disadvantages with regard to the heat transfer. Chys et al. [26] add to the list of analyzed working fluids and find possible advantages of about 12 %. As they only consider a heat source of 150 °C and 250 °C, none of their pure fluids can compete with the mixtures.

Trilateral Cycle and Organic Flash Cycle The best temperature match is achievable in the already introduced Trilateral Cycle (TLC). A practical

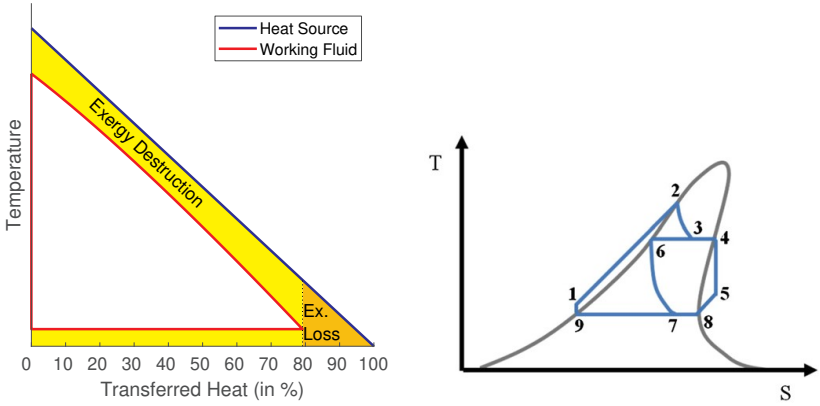

(a) Temperature match in an exemplary Trilateral Cycle.

(b) State diagram of an Organic Flash Cycle (from Ho, Mao, and Greif [12]).

Figure 2.9: Trilateral Cycles

implementation is possible, when the evaporation phase of the ORC is completely discarded and the heat transfer is limited to the preheating phase. At a sufficiently high pressure, the fluid is heated up just to its boiling point. Without the isothermal boiling phase, the temperature curves of heat source and working fluid almost perfectly align (see fig. 2.9a). The saturated liquid is then fed to a two-phase expander where expansion and evaporation take place simultaneously while delivering work.

The simulations of Fischer [11] show that a TLC at heat source temperature of 150 °C promises an advantage of second law efficiency of about 29 %[2] over an optimized, transcritical ORC (TLC – water: η_{II} = 48 % vs. ORC - supercritical propane: η_{II} = 37 %). These calculations are based on an assumed isentropic expander efficiency of $\eta_{is,E}$ = 85 %. According to Yari et al. [22], the TLC outperforms an optimized ORC and a Kalina Cycle for a heat source temperature of 120 °C by 35 % and 86 %, respectively (TLC - n-butane: η_{II} = 45 % vs. ORC - R1234yf :η_{II} = 34 %). However, these numbers are based on the assumption of a suitable two-phase expander which provides an isentropic

[2]Fischer [11] uses the "exergy efficiency for power production" ξ_P to rate the cycles. The definition equals the second law efficiency and can therefore easily be compared

efficiency that can compete with current ORC turbines ($\eta_{is} \approx 85\,\%$). A more realistic expander efficiency of $\eta_{is} \approx 75\,\%$ would still give the TLC a thermodynamic advantage over the other two cycles, but makes the ORC the most economic solution for the low temperature heat source.

While the matching heat transfer promises for an almost perfect power cycle, the necessary "two-phase expander is the technically most challenging component" [11]. Where ORCs are often operated with superheated turbine inlet conditions to avoid droplet formation at any cost, it becomes clear that a turbine is not a suitable component for intended two-phase expansion. Volumetric machines like scroll and screw expanders can easily handle the liquid fraction. However, their limited expansion ratio and the complex geometry make them specialized and, especially for the very large volume flows that occur in the TLC [38], expensive items. In addition, the rapid expansion in the machinery is still not fully understood and subject to current research like Kanno and Shikazono [39].

One approach to evade the two-phase expansion is the flash-expansion of the saturated liquid through a throttle. Ho, Mao, and Greif [12] introduce the advanced setup of an Organic Flash Cycle (OFC), where the saturated high-pressure liquid (state point 2 in fig. 2.9b) is first partly flash evaporated (3) before the vapor fraction (4) is fed to a common turbine. Meanwhile, the liquid fraction (6) is further expanded through a throttling valve and is mixed with the turbine outlet (5). The rest of the cycle matches the setup of the other cycles: condenser, feed pump and heater. The investigated heat source is hot water at 300 °C. While they reach impressive internal efficiencies of up to $\eta_{II,int} = 92\,\%$, the throttling losses completely outweigh this advantage. So, the proposed OFC setup could be realized with turbine technology that is already commonly used for ORCs, but the total power output and efficiency can not at all outperform a well designed standard ORC. Being well aware of this condition, Ho, Mao, and Greif [21] follow up with a revised setup of their first introduced cycle. In order to reduce the throttling losses, the whole process is split into two stages—high and medium pressure. Different concepts with remixing liquid and vapor streams of the different stages reduce the overall irreversibilities. These modified setups promises an advantage in the second law efficiency of about 10 % over a benchmark ORC for hydrocarbon working fluids. However, for a fair comparison, these numbers should be matched against the efficiencies of a multi-stage ORC as well.

The previously summarized research showed that more complex and advanced cycles can pay off especially for the low-temperature segment. The range of 300 °C is well covered by the common ORC, but the OFC could be more advantageous at lower operating conditions. However, the question of the profitability of the additional components for the additional OFC stage remains open. At last, both the TLC and the OFC share one more disadvantage when it comes to economic considerations. The coefficient for convective heat transfer to a liquid can be smaller than the coefficient for boiling heat transfer by an order of magnitude. Consequently, the improved temperature match is reached at the price of bigger and therefore more expensive heat exchangers for the heat input.

Discontinuous and Partly Discontinuous Cycle Concepts Several conceptual ideas were presented picking up on the idea of the perfect temperature match of the TLC. They all claim to benefit from the heat transfer at a (nearly) constant temperature difference, but can avoid both the challenges of two-phase expanders and the irreversibilities that occur during a rapid flash evaporation in a throttle.

The proposed setup of Steffen, Löffler, and Schaber [40] only differs in the expansion unit, while the remaining parts of their cycle are identical to the typical TLC. Where the two-phase expansion in a scroll or screw expander combines expansion and evaporation in the same unit, those two processes are separated here. In contrast to the continuous nature of all the previously discussed cycles, the discontinuous expansion in a piston engine is intended as follows: A small amount of saturated, high-pressure liquid from the heater is injected into a cyclone. With the piston movement of the connected engine, the liquid in the cyclone is flash evaporated. However, the separation ability of the cyclones ensures that only the vapor will enter the piston chamber. During the return movement of the piston, the expanded vapor and the remaining liquid are discharged to the condenser and the next injection can take place. The major source for losses is the dead volume of the cyclone which causes uncontrolled, instant evaporation at injection and the remaining liquid at the end of each piston stroke. In order to convert a larger amount of heat, a higher injection mass or higher engine speed would be necessary. In turn, those measures lead to a reduced isentropic efficiency due to the increasing

dead volume and injection / discharge dynamics. Steffen, Löffler, and Schaber [40] compared an ORC (with an expander efficiency of $\eta_{\mathrm{is,exp}} = 85\,\%$) to their cycle (with specifically calculated isentropic expander efficiencies for each working fluid) following the calculations of Fischer [11]. Even though they state that the assumed efficiencies of Fischer [11] seem quite high for small scale turbines, their setup shows an advantage over these benchmark ORCs of about 70 % at 120 °C heat source temperature (TLC - water: $\eta_{\mathrm{II}} = 43\,\%$ vs. ORC - supercritical propane: $\eta_{\mathrm{II}} = 25\,\%$). However, despite their detailed analysis of the dependence between injection mass, dead volume, cycle timing, engine speed and efficiency, neither did they present which values were finally used in the comparison with the ORC nor is their comparably low result of the benchmark ORC reproducible. Still, the general findings seem to endorse their idea on the separation of flash evaporation and expansion.

In comparison, the approach of Löffler [41] is aimed at a batch-wise heat source handling rather than on a batch expansion. The proposed cycle includes a large vessel that is initially loaded with the heat source. The inner working fluid cycle itself resembles a common ORC that is designed for a wide range of working conditions. Instead of the balancing act between internal and external efficiency, the operation is strictly aimed for a maximized internal cycle efficiency. However, after the heat exchanger, the heat source and its remaining exergy content are not discarded but simply feed back to the storage unit. Over time, the stored heat source therefore gradually cools further down and the evaporation pressure of the cycle is accordingly adjusted. This setup can best be summarized as a multi-stage ORC where the stages are not implemented in form of different units but are realized with one working fluid cycle at different operation points. Figure 2.10 on the next page shows an example of this idea, where the process is displayed by five representative stages at different times of the cycle sequence. Starting from the left, the initial hot heat source is harnessed by a high–pressure pass of the cycle. After the expansion of the working fluid (first “dip” in the figure), it is condensed and then pressurized again. In order to match the changed heat source conditions, the evaporation pressure is lower in this second pass. Following the heat source temperature, the pressure level of the working fluid is adjusted for every cycle pass. To maintain quasi-stationary conditions for the ORC, the mass in the heat source storage has to be high enough compared to the mass flow of the working fluid. Once a lower temperature limit of the heat source

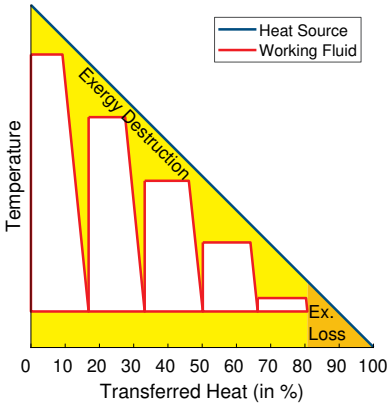

Figure 2.10: Temperature match of five virtual stages over the cooldown of one storage vessel load as proposed by Löffler [41].

medium is reached, the storage vessel is discharged and reloaded with the next batch of hot heat source. In order to avoid a periodical downtime during the reloading, two storage units for alternating use are proposed. The idea of a multi-stage ORC with the need for only one actual stage sounds promising. However, to rate the overall performance of this cycle, extended transient simulations are essential. While the author addresses the challenge of the wide operation range with estimated dimensions for screw expanders, the overall energy and exergy balances have yet to be provided.

The concept of a batch-wise heat transfer is also picked up in the first concept of Misselhorn [42]. The proposed Misselhorn Cycle consists of two heat exchangers—one evaporator and one condenser—as well as a single-piston engine. The working fluid is fed from the overhead condenser to the bottom-lying evaporator simply by gravity. Only then is the evaporator completely sealed and heated, and pressure will build-up during the isochoric evaporation. Once the vapor pressure of the upper temperature level is reached, the connection to the engine is opened and the high pressure is used to move the piston. To compensate the increasing volume caused by the piston movement, the working fluid is further heated and the remaining liquid is evaporated as well. The high pressure can therefore be maintained during the whole

expansion phase. At the end of the expansion, the connecting valve from the engine to the condenser is opened and the link from the evaporator is closed. The condensation causes a pressure drop and the liquefied working fluid accumulates in the condenser, ready to be fed to the evaporator again. This setup was originally introduced to reduce the overall structural complexity and to avoid the need for a feed pump. However, the used isochoric batch-evaporation also leads to a continuously rising working fluid temperature during the evaporation without an isothermal phase. The temperature profile is therefore quite similar to the heating phase in the TLC, but the endpoint is already in the two-phase region rather than on the saturated liquid curve. The technical implementation by Moullion [43] shows more resemblance with the previously discussed cycle structures. The isochoric batch-evaporation still takes place in a heat exchanger that can be completely sealed from the rest of the cycle. Three of these evaporators are operated in alternating turns to compensate the batch-wise character. The single-piston engine is replaced by a version with several cylinders as found in diesel generator sets. Instead of one piston stroke per discharging evaporator, the discharging stream is now used as a continuous source for the high-revolution engine. The condenser can therefore also be implemented as continuous component. The gravity-based feed system is replaced by a feed pump. However, the size of the pump can be smaller than for an ORC / TLC setup as no increase in pressure is necessary.

All three of the above cycles are more of basic ideas rather than full concepts. In order to properly rate and compare them to established cycles, they all lack further analysis. Most importantly, this includes the comparison of actual temperature levels of streams where heat transfer takes place, overall energy and entropy balances and full transient simulations to cover the nonsteady development of the discontinuous aspects of each concept.

In summary, all three of them use one discontinuous element in order to match the temperature profile of heat source and working fluid:

- Steffen, Löffler, and Schaber [40] use the continuous “common TLC-heating” which leads to a linear temperature profile of the working fluid. The necessary two-phase expansion is handled by batch-wise flash evaporation just outside of a piston engine for each piston stroke. It is expected that the rapid flash evaporation still causes significant losses as reported by Ho, Mao, and Greif [12] for their OFC.

- Löffler [41] proposes a batch storage on the heat source side that provides an almost constant heat source temperature to the cycle. The inner cycle itself is a common continuous concept that has to adapt to the gradually decreasing heat source temperature. The wide range of conditions, including changing mass flow and heat transfer coefficients of the working fluid, is expected to lead to a challenging design of the cycle as there is no single operation point.
- The Misselhorn Cycle [42, 43] uses a continuous heat source handling. Only the evaporators are designed for an isochoric batch evaporation. The expansion engine and condenser are fed with a varying, but continuous stream of fully gaseous working fluid.

In the following, the cycle with three heat exchangers as proposed by Moullion [43] will lay the basis for the detailed evaluation of a promising low–temperature cycle. With its single-phase expansion and the stationary heat source conditions it will be further analyzed as the most promising and least complex of these three concepts. This work on the cycle was performed and funded in the context of a research project with *Maschinenwerk Misselhorn MWM GmbH*. The MWM project was sponsored by the Bavarian Ministry of Economic Affairs and Media, Energy and Technology in the context of the BayINVENT program (funding program for innovative energy technologies and energy efficiency). In contrast to the original *Misselhorn Cycle* by Misselhorn [42], the particular variant by Moullion [43] and all derived designs with several heat exchangers will be called *MWM Cycle*.

2.2 Economic Evaluation

In addition to the thermodynamic rating of a concept, only an economic evaluation will estimate its profitability at last. The decision if and when an investment should be made can be based on different evaluation methods.

2.2.1 Economic Evaluation Methods

Payback Time The ratio of the initial investment and the average yearly revenue leads to the time when the “break-even” of the investment is reached.

The shorter this time, the smaller is the risk of the investment.

Return of Investment The ratio of the overall revenue to the overall investment costs defines the *Return of Investment* (ROI). High values are favorable, but cannot be directly rated against the current regular interest rate. The overall revenue depends strongly on the selected observation period and the ROI method is therefore best applied to short-term investments.

Specific Investment Costs The ratio of the total investment cost to the net power output gives the *Specific Investment Costs* (SIC), a rating of the investment costs that is independent of the size of the concept. While not giving any direct feedback about the profitability of an investment, it can best be used to compare the economic efficiency of concepts of different size and implementation.

Net Present Value According to Hutzschenreuter [44], all single cash flows (CF_k)—payments, investments and proceeds—are referenced and discounted to year 0 by

$$CV_k = CF_{j,k} \cdot \frac{1}{(1+i)^j}. \tag{2.20}$$

This cash value (CV_k) depends on the interest rate i and the year j when the payment occurs. The counter k denotes the index for one specific item (payment, component…). Early proceeds and late costs are favorable to their late and early counterparts, respectively (see fig. 2.11 on the following page). The individual cash values of each year and item are then summed up for the overall net present value

$$NPV = \sum_k \sum_{j=0}^{T} CF_{j,k} \cdot \frac{1}{(1+i)^j}. \tag{2.21}$$

In contrast to the previous three static methods, this dynamic approach considers the time value of money and is especially suited for evaluation of long-term projects. In the end, all dynamic methods measure the growth of an investment compared to the investment in the money market including the compound

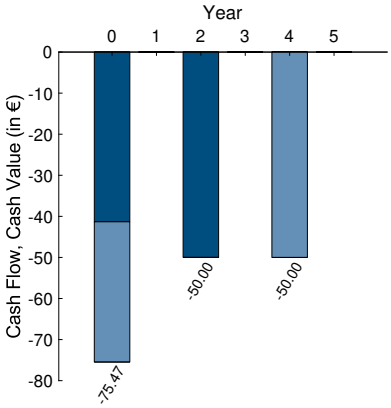

Figure 2.11: Two exemplary payments (cash flows), discounted to their cash values of year 0 (interest rate of 10 %) and summed up to the overall NPV.

interest. So, the revenues outweigh all costs and payments simply if the NPV is bigger than 0.

Annuity As a variation of the NPV-method, all cash flows are again scaled with the rate of interest and depending on the time of their occurrence. Where the NPV sums and references all cash flows back to year 0, the annuity methods goes one step further and splits the cash values of one-time events into "reverse-discounted" equal annual amounts – the annuities A_N:

$$A_{N,k} = \underbrace{\frac{q-1}{1-q^{-T}}}_{a} \cdot CV_k. \tag{2.22}$$

In this equation, $q = 1 + i$ is the annual interest factor and a is the annuity factor. The equally split annuities can then easily be balanced against annual ongoing payments and proceeds. If all the annuities resulting from one cash flow are discounted back to year 0 following eq. (2.20) and then summed, they again lead to the initial cash value (see fig. 2.12 on the next page).

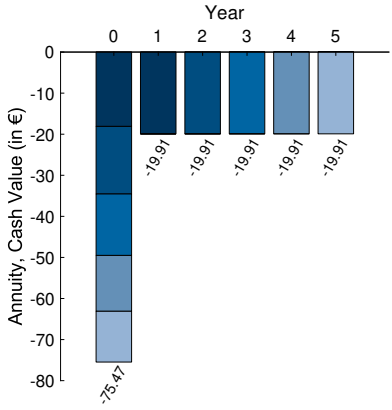

Figure 2.12: Exemplary cash value from fig. 2.11, split into equal annuities. Discounting & summing up leads back to the initial cash value.

Internal Rate of Return Both the Net Present Value and the Annuity method only rate the absolute profit and presume unlimited liquidity. An enormous, but hardly lucrative investment would still create a considerable profit. However, it would also bind a distinct share of the available funds. The *Internal Rate of Return* (IRR) provides the opportunity to identify the "most efficient" investment: It is defined as the virtual interest rate i_{IRR} where the Net Present Value would exactly be $NPV = 0$. A NPV of zero implies that an investment yields the same profit as the capital market can offer at this virtual rate. The IRR therefore directly represents the interest rate that can be realized with this investment. The IRR can not be solved analytical in most cases with more than two years or different cash flows. A simple iterative solver for the NPV calculations will, however, lead to the desired interest rate.

Dynamic Payback Time The IRR is a dynamic extension of the static ROI method based on the concept of the cash value. In the same manner, the static payback time can be extended to a "dynamic payback time" (dPBT). Typically, the negative CV of the initial costs in year 0 will gradually be compensated by the yearly positive cash values. At some point, the accumulated cash value (NPV up to this year) will become positive and the dPBT is found. In contrast

to the purely static PBT, interest rates and non-uniform cash flows are included in this definition. When the yearly cash values are calculated anyways in context of the annuity evaluation, the search for the dPBT is a simple matter of evaluating the array of cash values.

None of these methods can indicate the one single best investment. The final decision about the ideal investment always depends strongly on the philosophy and the available resources of the investor. Hutzschenreuter [44] recommends that small investments with a very high IRR should always be implemented. The remaining free capital about to be invested will normally be used on the other cases with an over-average IRR, the ones with the highest Annuity first.

2.2.2 Application of the Annuity Method

For long-term investments, Hutzschenreuter [44] and Verein Deutscher Ingenieure [45] recommend dynamic methods. The widely used VDI-norm 2067 [45] explains and applies the dynamic annuity method and it will therefore also be used for the cycle evaluation in this work. The following equations, abbreviations and symbols are used in accordance with this norm [45].

All upcoming cost—initial investments and recurring payments—can be covered by four categories:

- capital–related costs K_{C}
- demand–related costs K_{D}
- operation-related costs K_{O}
- other / auxiliary costs K_{A}.

Their individual annuities ($A_{\mathrm{N,C}}$, $A_{\mathrm{N,D}}$, $A_{\mathrm{N,O}}$, $A_{\mathrm{N,A}}$) as well as the annuity of the proceeds ($A_{\mathrm{N,P}}$) are summed up to the total annuity

$$A_{\mathrm{N}} = A_{\mathrm{N,P}} - \left(A_{\mathrm{N,C}} + A_{\mathrm{N,D}} + A_{\mathrm{N,O}} + A_{\mathrm{N,A}}\right). \tag{2.23}$$

The analyzed investment is only economical if the annuity of the proceeds exceeds the annuities of all costs which results in a total annuity of $A_{\mathrm{N}} > 0$. The higher the total annuity, the higher the gain from this particular investment.

Capital-Related Costs The capital-related costs or expenditures (CAPEX) consist of the initial investment and the replacement procurement. The estimation of the initial investment costs for all components K_0 are further discussed in section 2.2.3 and can be taken from eq. (2.39) on page 43. When the total observation time T is longer than the service life of a component T_N, the costs for its replacement have to be considered. Forecasting the price change based on the initial price of a specific component $K_{0,k}$ and then discounting this value back to year 0 leads to the cash value of the n-th procurement $CV_{n,k}$.

$$CV_{n,k} = K_{0,k} \cdot \underbrace{r^{n \cdot T_\mathrm{N}}}_{\text{price change}} \cdot \underbrace{\frac{1}{q^{n \cdot T_\mathrm{N}}}}_{\text{discounting}} \tag{2.24}$$

The index n indicates here the number of the procurement and is dependent on the service life of each component k. The price change factor r has to be taken from literature or official price indices for each corresponding group of investment (equipment, capital, energy…). If the end of the observation period does not match the end of a component service life, the residual value R_W is calculated by means of linear depreciation:

$$R_{\mathrm{W},k} = \underbrace{K_{0,k} \cdot r^{n \cdot T_\mathrm{N}}}_{\text{price at time of purchase}} \cdot \underbrace{\frac{(n+1)\,T_\mathrm{N} - T}{T_N}}_{\substack{\text{linear depreciation} \\ \text{of last replacement}}} \cdot \underbrace{\frac{1}{q^T}}_{\text{discounting to year 0}} \tag{2.25}$$

The capital-related costs for each component and all their replacements are then summed and converted to the annuity $A_\mathrm{N,C}$ with the annuity factor.

$$A_\mathrm{N,C} = a \cdot \sum_k \left(K_{0,k} + \sum_n CV_{n,k} - R_{\mathrm{W},k} \right) \tag{2.26}$$

Demand-Related Costs Assuming a constant operation over the years, the demand-related costs can be extrapolated from those of the first year of operation ($K_{\mathrm{D},1}$). The up-scaling to the total observation period is done by the

price dynamic cash value factor for the demand-related costs b_{D}.

$$b_{\mathrm{D}} = \frac{1 - \left(r_{\mathrm{D}}/q\right)^{T}}{q - r_{\mathrm{D}}} \tag{2.27}$$

The cash value factor from eq. (2.27) is also valid for other categories if their corresponding price change factor r is used. Combining the cash value factor and the annuity factor directly yields the annuity of the demand related costs.

$$A_{\mathrm{N,D}} = K_{\mathrm{D},1} \cdot a \cdot b_{\mathrm{D}} \tag{2.28}$$

The demand-related costs of year 1 ($K_{\mathrm{D},1}$) in turn are composed of the annual consumption-related costs like heating, cooling, electricity and water.

$$K_{\mathrm{D},1} = \sum_{k} Q_{\mathrm{k}} \cdot \mathrm{price}_{k}; \quad k = \begin{cases} \text{heat} \\ \text{cooling} \\ \text{electricity} \\ \text{water} \\ \dots \end{cases} . \tag{2.29}$$

Each part is the product of the annual amount of the demand Q_{k} and the specific $\mathrm{price}_{\mathrm{k}}$.

Operation-Related Costs The operation-related costs or operational expenditures (OPEX) can, again, be derived from the first year of operation. The amount of actual operational effort can be taken from the tables in the VDI norm 2067 [45] on a component-wise basis. The costs $K_{\mathrm{O},1}$ are then derived with average hourly wages.

Closely related are the costs for maintenance $K_{\mathrm{M},1}$ which are calculated as a fixed percentage of the initial investment costs.

$$K_{\mathrm{M},1} = K_0 \cdot \left(f_{\mathrm{repair}} + f_{\mathrm{s\&i}}\right) \tag{2.30}$$

The factors for repair effort f_{repair} and for service and inspection $f_{\mathrm{s\&i}}$ can also be found in the VDI 2067 [45] for each group of components. The estimated

costs for the first year are then extrapolated by means of the annuity factor and the cash value factor:

$$A_{\mathrm{N,O}} = K_{\mathrm{O},1} \cdot a \cdot b_{\mathrm{O}} + K_{\mathrm{M},1} \cdot a \cdot b_{\mathrm{M}} \tag{2.31}$$

Other Costs All other costs, mostly of administrative nature, are converted to their annuity as well.

$$A_{\mathrm{N,A}} = \sum_{k} K_{\mathrm{A},k} \cdot a \cdot b_{\mathrm{A}} \tag{2.32}$$

The single items are estimated either as a percentage of the initial investment costs (for example insurance of the components) or with a fixed amount (like liability insurance, public relations) according to Schlagermann [46]

Proceeds The proceeds can also be estimated from the first year of operation P_1 in the same manner as the costs described above. Assuming the price change can be covered by the price change factor b_{P}, the annuity of the proceeds follows from

$$A_{\mathrm{N,P}} = P_1 \cdot a \cdot b_{\mathrm{P}} \tag{2.33}$$

The proceeds themselves are calculated from the amount of sold product (heat, electricity) and the expected or guaranteed price. If irregular revenues are to be expected, the single price change factor may not be able to cover the development. For example, a novel concept like the MWM Cycle with little operational experience could lead to fewer operation hours in the first years. In such a case, the annual amount for every year should be discounted and summed (like for the NPV) and can only then be processed with the annuity factor.

$$A_{\mathrm{N,P}} = a \cdot \sum_{j=1}^{T} \left(P_j \cdot \frac{1}{q^j} \right). \tag{2.34}$$

2.2.3 Module Costing Technique

Some of the above described costs (capital-related costs and maintenance) are based on the initial investment K_0 which is the sum of all initial payments for

components. As this single value thereby affects a major share of the total cash value, the single assets should be estimated thoroughly. Precise prices are often not available and hard to inquire in advance. To cover this gap, Turton [47] collected and developed correlations for the price of various components based on their characteristic dimension X. The equation for the costs of a basic configuration (denoted by the superscript 0)

$$\log_{10} K_k^0 = C_1 + C_2 \cdot \log_{10} X + C_3 \cdot \left(\log_{10} X\right)^2 \tag{2.35}$$

should be corrected for the intended working conditions by a pressure factor F_p and a material factor F_M. The coefficients C_1 to C_3 are also tabulated in Turton [47] and are component–specific. While the material factor is also a tabulated value from Turton [47], the pressure factor is calculated by

$$\log_{10} F_p = C_{1,p} + C_{2,p} \cdot \log_{10} p + C_{3,p} \cdot \left(\log_{10} p\right)^2 . \tag{2.36}$$

One exception is the pressure factor for vessels and tanks, where the correlation depends on their wall thickness s_wall:

$$F_p = \begin{cases} 1 & \text{for } s_\mathrm{wall} < 0.0063\,\mathrm{m} \text{ and } p > -0.5\,\mathrm{bar_{gauge}} \\ \dfrac{\frac{(p+1)\cdot d}{2\cdot\left[850-0.6\cdot(p+1)\right]} + 0.00315}{0.0063} & \text{for } s_\mathrm{wall} > 0.0063\,\mathrm{m} \\ 1.25 & \text{for } p < -0.5\,\mathrm{bar_{gauge}} \end{cases} \tag{2.37}$$

Besides the wall thickness, the important dimensions in this correlation are the diameter of the vessel d and the design gauge pressure p.

In addition to the pressure and materiel correction, other indirect costs of the components have to be covered. The resulting bare module costs include all additional assets like transport, installation, piping and instrumentation/control/automation. The used bare module factor F_BM is build from the pressure and material correction as well as another component specific factor B from Turton [47]:

$$F_{\mathrm{BM},k} = B_{1,k} + B_{2,k} \cdot F_{\mathrm{M},k} \cdot F_{p,k} \tag{2.38}$$

According to Bejan, Tsatsaronis, and Moran [48], a typical bare module factor would have a value of about $F_{\mathrm{BM},k} \approx 1.45$.

Finally, adding some overhead for the general design (21.9 % [49]), the auxiliary construction and piping (12 % [47]) and the instrumentation (8 % [47]), the total initial investment then follows as

$$K_0 = \sum_k K_{0,k} = \sum_k K_k^0 \cdot F_{\mathrm{BM},k} \cdot (1 + 0.219 + 0.08 + 0.12)\,. \tag{2.39}$$

In a final step, the estimated investment has to be converted from the reference year and the currency of the correlations to the target conditions. Similar to the price dynamic cash value factor b, the total investment estimation has to be proportionally converted from the reference year of the correlations to the reference year of the cost estimation by means of price indices:

$$\frac{K_{0,\mathrm{then}}}{K_{0,\mathrm{now}}} = \frac{\text{price index}_{\mathrm{then}}}{\text{price index}_{\mathrm{now}}}. \tag{2.40}$$

The fluctuations of exchange rates can also have a short-term effect on the economic evaluation.

2.2.4 Summary of Economic Evaluation

In summary, the economic evaluation is based on the one main balance of positive and negative annuities (eq. (2.23)). Several of these annuities (capital-related eq. (2.26), operation-related eq. (2.31) and other costs eq. (2.32)) depend on the estimated costs of the initial investment for the components (eq. (2.39)). They, in turn, consist of tabulated cost estimations corrected by different factors for operating conditions and some overhead.

The total annuities of different concepts and variants are then directly rated against each other. A positive annuity implies that this concept is more profitable than the sole investment at the capital market with current interest rates. Moreover, the higher the total annuity, the bigger the profit.

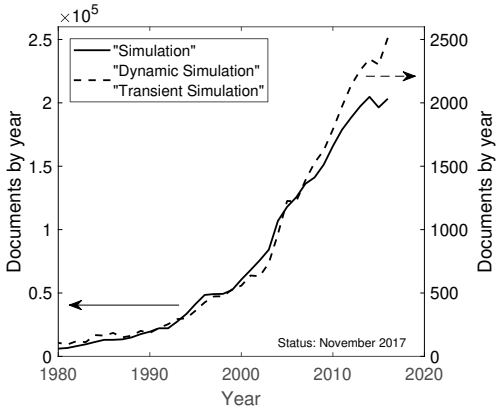

Figure 2.13: Disproportionately increasing topic occurrence for dynamic and transient simulations in Scopus (Title, Abstract, Keywords).

2.3 Model-Based Analysis of Thermodynamic Cycles

The increasing demand for more efficient and economic concepts causes a need for better and more detailed analyzing tools. Especially the non-stationary effects, induced by the fluctuation of renewable energy source (predicted for example by Buttler et al. [50] and Nitsch et al. [51]), the dynamic operation of a power cycle (see Quoilin et al. [52] and Orlandini et al. [53]) or a dynamic characteristic of the cycle concept itself (as seen in the concepts of Steffen, Löffler, and Schaber [40], Löffler [41], and Misselhorn [42]), have to be taken into account. Conventional problems are best solved with the common, commercial software packages for cycle simulation like Aspen Plus®, Ebsilon® Professional or Dymola. However, most of them can only model steady-state problems. Facilitated by the rapidly increasing computational power of modern hardware, the rising demand for specialized and non-stationary models becomes apparent from the growing share of publications about “dynamic” and “transient” simulations in current literature (see fig. 2.13).

With the access to more detailed and more extensive simulations, the

amount of output data increases rapidly as well. A simple sensitivity analysis over one or two parameters, like for the evaporation pressure in section 2.1.3, will not be feasible anymore. Instead, a combination of various parameters and possibilities has to be covered. Different optimization methods are available that can simultaneously handle various input parameters and will find the best case with a manageable amount of simulation runs.

Some of the most common modeling approaches for transient problems are presented in section 2.3.1. A short introduction to the genetic optimization algorithm is given in section 2.3.2.

2.3.1 Transient Modeling Approaches

As for example discussed by Jensen [54] and Gleinser, Wieland, and Spliethoff [55], the underlying balances for energy and mass of a thermodynamic model are to be broken down to partial differential equations in order to build a simulation model. Those conservation equations are interconnected by means of mass flows, heat conduction and heat transfer. Even for very simple, but transient problems, the resulting differential equations cannot be solved analytically anymore and have to be handled by numerical approaches. Depending on the difficulty of the task, the complexity of the approach varies.

If wide zones with an almost homogeneous behavior can be identified in the problem, a moving boundary approach (as used by Bell et al. [56] and Li, Luo, and Dang [57]) is often the best choice. Each of those patches can then be represented as one uniform sub-problem in good approximation. A typical example of use is a dynamic flow problem including single–phase heat transfer and evaporation. When splitting the whole domain into the two major regions, preheating and evaporation, the corresponding thermodynamic properties (heat transfer coefficients, heat capacity of fluids…) can be approximated by constant and linearly dependent values, respectively. Over the observed period, the location of the edge between the two zones might move and has to be tracked. Hence, the name—moving boundary approach.

When the task becomes more complex, the distinguishable zones become more and smaller and will completely vanish at last. At this point, a fully discretized approach has to be implemented. The continuous nature of the partial differential equations is therefore approximated by finite elements that are small enough to cover the gradients in the thermodynamic effects

properly. Each of those elements is then again represented by one small but uniform sub-problem. Finite differences (see [58, 59]) or finite volumes (compare to [52, 54, 60–62]) can map almost any problem and are more robust than a comparatively coarse moving boundary approach (Bendapudi, Braun, and Groll [63]). However, they are computationally more expensive due to their increased number of sub-problems. The equal and fixed size of all finite elements is also dependent of the most challenging gradient. If there is only one sharp change in an otherwise smooth domain, the predominant share of the problem will be "over-discretized" in the same fine grid and cause unnecessary overhead.

Feru et al. [16] propose a combination of moving boundary and finite discretization: taking the above example of a simple dynamic flow again, the domain is also split at the transition of preheating to evaporation. The resulting two patches are then discretized with a medium-coarse grid. Moderate variations within one of these zones (typically in the evaporation zone) can be matched much better than with the uniform section of a pure moving boundary approach. As the grid does not have to cover the challenging gradients of the transition itself, the grid size and computational effort is not as expansive as for the fully discretized approach though. Whether the reduced number of elements compensates for the additional structural effort for the boundary-handling has to be established for each individual application.

In section 5.1.1, the different modeling approaches for the evaporators of the MWM Cycle will be introduced. Both a moving boundary like method and a detailed finite elements section are implemented for different parts of the evaporators.

2.3.2 Optimization Approaches

For simple, smooth problems (objective twice differentiable), the first choice for an optimization are gradient-based solvers (Press [64]). Starting from a given or random initial point, they follow the slope to the local minimum like a ball on an inclined surface. A dynamic step-size, big steps at first and smaller steps when they get closer to the minimum, guarantees a most efficient number of iterations. Beyond the ball analogy, they can of course also be applied to multi-dimensional problems. More complex scenarios often feature more than one region with independent local minima. The

simple gradient-based solvers can only find the one in whose sink they start. Global optimization algorithms therefore use multiple starting points spread over the whole problem dimension. For applications in the field of cycle optimization, the smoothness of a problem is not guaranteed. Thermodynamic properties can show rough edges during phase change and physical limitations can disrupt regions of otherwise perfect performance. Those problems are therefore best handled by multi-point stochastic approaches. They also start with multiple initial points spread over the whole domain. Instead of following the—partly non-existent—gradient of the problem, they all use some kind of stochastic sub-pattern to map and evaluate the problem domain. A common solver of this kind is the genetic algorithm. Ready-to-use implementations are for example available for Matlab or Python.

The genetic algorithm (ga) adapts three main evolutionary principles to minimize complex, non-smooth and discontinuous optimization problems: selection, combination and mutation. The procedure is outlined by Goldberg [65] as follows. One specific set of values for the optimized independent variables ($\vec{x}$) is represented by a single *individual*. Each iteration of the algorithm holds a whole group of those individual: one *generation*. The initial generation is randomly created with the goal to evenly cover the whole problem domain. Setting upper and lower *boundaries* for the independent variables helps to narrow down the problem. Next, all individuals of one parent generation are evaluated by the *fitness function* $f(\vec{x})$. The fitness function returns the target of the optimization, for example an efficiency or an economic number for the given individual. Based on this *fitness value*, the individuals are rated and sorted. The best individuals directly enter the next generation as *elite children*. The others are slightly adjusted by *cross over* (random items of $\vec{x}$ are exchanged between two moderate parents) and *mutation* (random items of $\vec{x}$ are varied by a small random factor). Those variations can already be limited by some *constraints*. In the context of thermodynamic cycles it is for example necessary that the evaporation pressure is bigger than the turbine outlet. The new generation is again evaluated and becomes the next parent generation. The stop criterion can be a maximal number of generations or a minimal average improvement for the last generation that defines the end of the algorithm.

It is unavoidable for these stochastic approaches that an unfavorable cross over can split an already properly matching pair or subset of variables. On the

other hand, the algorithm has to know nothing about the partial dependency of some variables and a matching pair can still, by chance, be combined with promising other characteristics. In summary, this stochastic approach can handle most complex problems and even integer variables, but comes at the price of a drastically increased number of iterations compared to gradient-based solvers.

Chapter 3

Objectives

In this chapter, the literature review is summarized. Based on the current state of the art, the research demand and open questions are formulated and the aims of this work are defined. Finally, the outline of this work is presented.

3.1 Research Demand

The previously presented state of the art illustrates the great relevance of low-temperature power cycles. Numerous publications and surveys analyze the potential of low-temperature applications and try to put a number on the possible economic advantage. Despite this great interest within the academic field, the availability of real-life installations is quite limited.

The first and major challenge for low-temperature cycles is the limited efficiency. The established and well-developed Organic Rankine Cycle (ORC) is only economically feasible for at least medium-low temperatures (>150 °C). More advanced cycles outperform the ORC with regard to efficiency, but are more complicated, more expensive or not technically realizable to date. The selection of an appropriate working fluid that matches the heat source temperature can improve the system efficiency of the ORC to some extent. Besides the well known refrigerants, there are several new fluids for heat source temperatures above 120 °C which comply with recent and future regulations. However, there are no high–performing working fluids—former or more recent ones—for temperatures around 100 °C.

In a recent development, several concepts propose transient cycles for low-temperature applications. For example the “New Triangle Cycle” [40], “Batch Processes in Heat Engines” [41] and the “MWM Cycle” [43] promise a higher

efficiency than the ORC and, at the same time, a practical feasibility due to the moderate demands to the cycle components. However, the cycles themselves, their dynamic behavior, and the thermodynamic and economic performance with different working fluids are not fully explored so far.

Besides these concepts, also other advanced cycle setups as well as the changed framing conditions for power generation call for new research tools. Many out-of-the-box solutions cannot properly handle the important, upcoming dynamic aspects of power generation and power cycles. In order to cover all the relevant effects, it is often necessary to develop custom-build models that fit the individual problem.

3.2 Aims

This Dissertation aims to asses the potential of a suitable and realizable power cycle for low-temperature heat sources. To come to a well–informed decision, it is first necessary to survey the available concepts before selecting the most promising one. Then, the underlying basic principles have to be studied in order to fully understand the chosen concept. Based on these theoretical findings, a detailed and case-specific simulation model can be build. The simulation results and the identification of all relevant effects provide a significant basis for the comparability to other cycle concepts. The objectives are therefore defined as follows:

Select Promising Concept Current concepts for low-temperature power cycles should be screened and the most promising one has to be selected for further assessment.

Characterize the Cycle The selected concept should be analyzed with focus on the theoretical background. The gained theoretical insight has to be used to improve the originally introduced setup where possible.

Model the Cycle The cycle setup should be represented by an appropriate simulation model. All relevant effects of the dynamic behavior have to be covered and the cycle parameters have to be optimized.

Rate the Cycle The system efficiency and the economic aspects have to be compared to a benchmark ORC under consideration of different reference conditions and suitable working fluids.

3.3 Research Approach

The cycle and model development in this work is based on the state of the art that is presented in **chapter 2**. First, the general challenges for low-temperature cycles and some promising, advanced cycle setups were introduced. Of the reviewed transient concepts, the MWM Cycle was selected for further analysis as the most promising and least complex one due to its single–phase expansion and the stationary heat source conditions. With regard to the economic evaluation, a review of economic indicators and calculations was given. Furthermore, different modeling approaches, which are widely used in literature, were introduced and discussed.

Before the details of the model implementation are presented, the MWM Cycle itself is elaborated in detail in **chapter 4**. The basic idea of the batch evaporation was already introduced in the literature research. A special form of the temperature-heat-diagram is introduced in this work in order to visualize the exact functionality and the thermodynamic advantages of the MWM Cycle. Those diagrams display the quality of the heat source utilization and led to an improved setup with a cascaded heat source flow. All process parameters are discussed here and the free variables are defined.

The MATLAB model of the MWM Cycle is composed by four structural layers (see **chapter 5**). The inner section handles the individual evaporators, the heat and mass transfer within those and the temporal progress of the properties. The simple module is only based on a NTU-approach (Number of transfer units) with quasi-stationary heat transfer calculations. The flow characteristics and the thermal inertia of the heat exchanger are only included in the more complex cell-model module. These two implementations of the heat exchanger can easily be swapped depending on the desired level of detail. The second layer handles the overall simulation sequence. This includes for example the switching between the cycle phases and the routing of the heat source medium. Layer one and two already form a complete model to run a single evaporator configuration. Level three adds a genetic algorithm to

optimize the process parameters with regard to a maximal cycle performance or other targets. The outer fourth layer deals with the high computational demand of the optimization and prepares the model for parallel computation on a multi-core workstation. In addition, a simple ASPEN model provides benchmarking results of a common ORC. The general modeling assumptions for both the MWM Cycle and the ORC simulation are also given and compared in this chapter.

The reference conditions for all simulations are defined in **chapter 6**. Subsequently, the simulation results of the two cycles are compared and discussed with regard to overall system efficiency and economic aspects. Different established and new working fluids are tested for their suitability at the defined heat source temperatures in both cycles.

Chapter 7 gives a summary of the results, a recommendation with respect to the feasibility of the MWM Cycle in low-temperature power generation and an outlook for possible further work.

Chapter 4

Process Development of the MWM Cycle

This chapter covers the principle of operation and the specific characteristics of the MWM Cycle. The first section explains and compares the gradually rising temperature profile of the MWM Cycle in contrast to the pinch point limited ORC behavior. Furthermore, the adjustments to the typical state diagrams are addressed. They are necessary in order to display the combination of a dynamic batch process on the working fluid side of the evaporator and a continuously flowing heat source medium on the other. The resulting opportunities and challenges of the MWM Cycle are summarized in section two: On the one hand the almost perfect temperature match — On the other hand, most notably, the increased number of free variables that have to be handled and which are further discussed at the end of the second section.

4.1 General Operation

The basic layout of the MWM Cycle as proposed by Moullion [43] is quite similar to that of a simple ORC. Figure 4.1 shows the expansion engine, condenser and feed pump that can be found in both the MWM Cycle and the ORC. Only where the ORC shows one continuous evaporator, the MWM Cycle is equipped with at least three parallel batch evaporators that can individually be sealed off from the rest of the cycle.

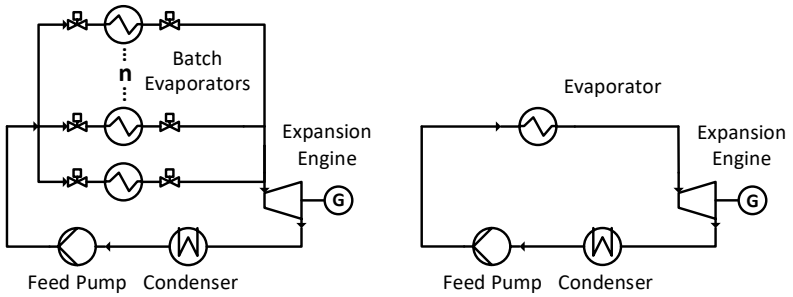

(a) MWM Cycle (b) Reference ORC

Figure 4.1: Comparison of process layouts.

4.1.1 Thermodynamic Processes on the Working Fluid Side

When analyzing the heat source utilization, the T-Q-diagram offers a practical form of presentation. However, when the focus lies on the cycle itself and phase changes are important, a temperature-entropy-diagram (T-s-diagram) is often favorable. To give an example, fig. 4.2 shows a simple ORC in a T-s-diagram. The transitions between the state points are:

1-2: isentropic compression of liquid in the feed pump (with isentropic efficiency $\eta_{\mathrm{is,fp}}$),
2-3: isobaric heating in the evaporator: preheating to state **2'**, evaporation to state **2"** and, where necessary, superheating to state **3**,
3-4: isentropic expansion in the expansion engine (with isentropic efficiency $\eta_{\mathrm{is,exp}}$),
4-1: isobaric cooling in the condenser: if the end of the expansion is still superheated, the saturated vapor is marked by **4"**.

The superheating is not mandatory for the process itself. However, as mentioned in the context of the two-phase expansion of the Trilateral Cycles, the commonly used turbines cannot handle any liquid fraction in the working fluid stream. Therefore, a slight superheating is advisable for wet and isentropic fluids.

The T-Q-diagrams in chapter 2 show only a simplified version of this ref-

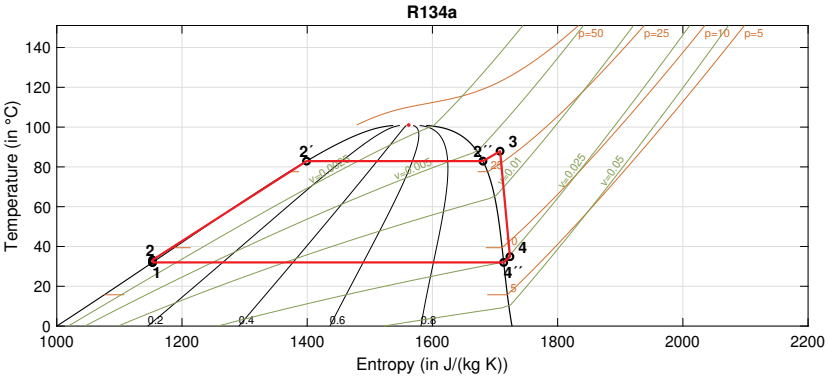

Figure 4.2: Progress of the working fluid in an exemplary ORC in a T-s-diagram.

erence ORC: The state points **1** and **2** are almost identical due to their small temperature difference. Furthermore, with the focus on the general temperature match, the state after the expansion is not too important for the discussions of the process itself. When neglecting the superheating, state point **3** is of saturated nature and falls together with point **2”**. Depending on the properties of the fluid, state point **4** may be superheated vapor, saturated vapor or lie in the two-phase region. As transferred heat Q leads mostly to changes in temperature T and entropy s of the working fluid ($dQ = Tds$ for ideal processes), the ORC looks quite similar in the T-s-diagram and the previously presented T-Q-diagrams (compare for example to fig. 2.3 on page 14). Both diagrams emphasis the distinctive kink at the onset of boiling and the plateau of constant temperature during the evaporation.

For the *continuous ORC*, the progress along the curve of the working fluid in the diagrams matches the *spatial movement* of a fluid element in the setup (from feed pump to evaporator, through expansion engine, condenser and back to feed pump). All the components represent *stationary open systems*, where the fluid state varies only over space and not over time. Accordingly, the corresponding specific properties are referenced to the constant mass flow of the cycle. In comparison, fig. 4.3 on the next page gives an example of a *transient MWM Cycle* in a T-s-diagram:

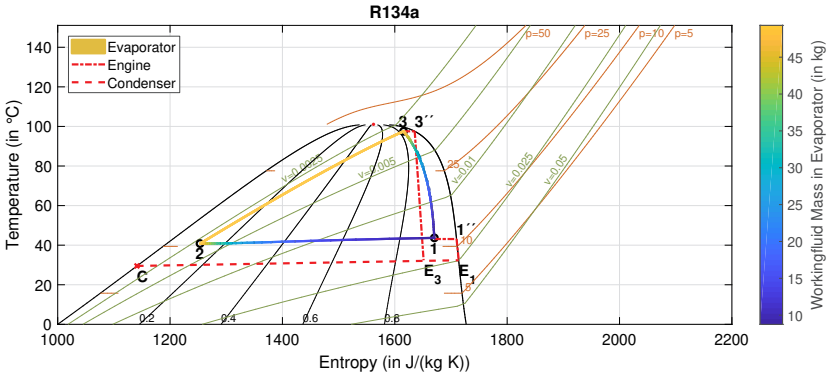

Figure 4.3: Progress of the working fluid in one evaporator of an exemplary MWM Cycle in a T-s-diagram.

- The MWM Cycle also contains *quasi-stationary open systems* in the expander, condenser and feed pump. The averaged streams through expander and condenser (red) represent a spatial progress that, like for the ORC, corresponds to a mass flow.
- In addition, the cycle consists of an *unsteady, open batch system* in the evaporators, where the states change over time *and* space. In contrast to the *spatial movement* in the ORC-figure, the curve of the unsteady working fluid in fig. 4.3 represents the *temporal progress* at a fixed location within one evaporator. With the MWM being a dynamic cycle, also the total mass within the evaporators changes over time. The specific properties are here based on the current mass rather than a mass flow.

Consequently, two different types of T-s-diagrams have to be combined in order to show the whole MWM Cycle in one figure: the specific states of the temporal progress of an enclosed mass and the specific states of the spatial progress of a mass flow are opposed. Even though being plotted side by side, it is not possible to directly draw any conclusions about their mass ratio or combined state due to their different nature.

In detail, the following steps take place in the MWM Cycle (fig. 4.3):

1-2: Open polytropic filling phase: The almost empty evaporator is filled with slightly subcooled liquid working fluid from the condenser **C** by

the feed pump. The mass in the evaporator rises (see color bar) and the state of the filling is moving towards a lower vapor quality q due to the cold liquid feed stream.

2-3: Closed isochoric batch evaporation: The evaporator is completely closed. The heating of the constant mass at a fixed volume causes a rising pressure, temperature and vapor fraction.

3-1: Open polytropic discharge phase: The vapor fraction (**3"**) of state **3** is gradually discharged to the expansion engine while the liquid phase remains in the evaporator. On the one hand, this leads to a decreasing vapor quality. On the other hand, the decreasing total mass also causes a pressure drop. The combination of the further heating and the pressure drop results in a re-evaporation of the remaining liquid and compensates the lost vapor fraction. When the lower pressure limit of the cycles is reached (**1**), a small amount of working fluid at a high vapor quality state remains in the evaporator and is mixed with the feed stream from the condenser **C** in the next filling phase.

3"-E: Continuous Expansion: At the beginning of the discharge phase, the saturated vapor phase (**3"**) of the corresponding state point **3** is fed to the engine and is expanded to the condenser pressure. Including the isentropic expander efficiency $\eta_{\mathrm{is,eng}}$, state point $\mathbf{E_3}$ is reached. Over the progress of the discharge phase, the process pressure gradually declines from **3** to **1** and the corresponding state point **3"** slides down along the saturation line. At the end of the discharge phase, the last expansion takes place from state **1"** to state $\mathbf{E_1}$.

E-C: Continuous condensation: The expanded vapor is condensed at the condensation pressure level and is available for the feed pump at state **C**. The pool of liquid working fluid in the condenser buffers the variations of the stream coming from the engine.

Again, it has to be taken into account in fig. 4.3 that the graph of the evaporator corresponds to the batch progress of the working fluid in the fixed domain of one evaporator over time. In contrast, the red lines of engine and condenser show quasi stationary, continuous processes that do, along these lines, not change over time but over space.

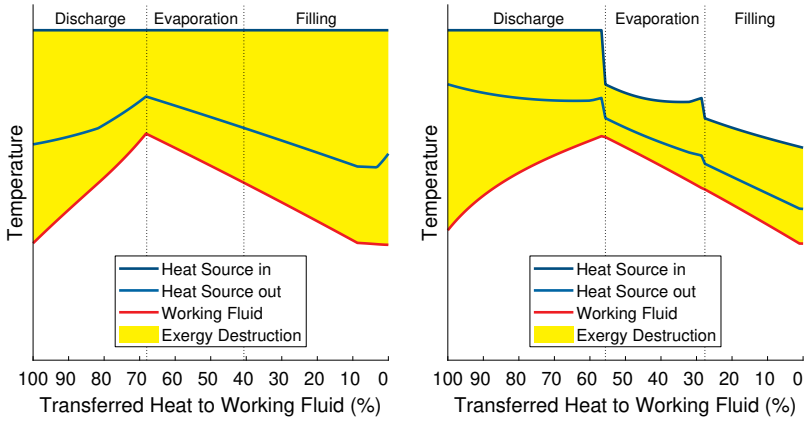

(a) Simple (Parallel) Heat Source Flow

(b) Cascaded Heat Source Flow

Figure 4.4: Qualitative comparison of heat source utilization by batch evaporation for two different heat source layouts.

4.1.2 Thermodynamic Processes on the Heat Source Side

Adding the change of the heat source temperature to the T-s-diagram of the ORC is simple. Each point of the working fluid between state **2** and **3** relates to one specific position in the evaporators and can easily be matched to the single locally corresponding state of the cooled heat source. This matching works for both the T-s- and the T-Q-diagram and shows the exact interacting temperatures of the two streams being the drivers for heat transfer. A commonly used counter-flow setup for working fluid and heat source stream then leads to the typical temperature match as seen in the previous T-Q-diagrams of the ORC.

This procedure is more complex for the MWM Cycle. As the process graph here maps the progress over time, the whole plot has to be based on the development over time. Is has to be noted that not only the evaporation phase but all phases of the MWM are heated and therefore the T-Q-diagram in fig. 4.4a covers an “unfolded”, complete version of the state points **1** - **2** - **3** - **1**. The corresponding phases are indicated by the vertical, dotted lines

and are in the order of: filling – evaporation – discharge (from right to left). Due to the time-base of this plot, the heat source stream has to be matched by time and its local information would be lost. Moreover, the continuous and time–independent heat source would always show the same inlet temperature for the whole time domain of the cycle (see "Heat Source in" in fig. 4.4a). To cover both time and space in one figure, a 3-D plot would be needed. In order to avoid the complexity of such a 3-D plot, some simplifications were made. Taking the example from fig. 4.3 again, simply the start- and end-point of two exemplary instances of the continuous expansion were plotted (3" to E_3 and 1" to E_1). In the same manner, only the inlet and outlet temperatures of the heat source were plotted for every instant of time in fig. 4.4a.

Even though the MWM Cycle here shows the desired gradually rising process temperature (cycle progress from right to left), the temperature match is even worse than for most ORCs: the constant inlet temperature of the heat source causes a great amount of exergy destruction. Furthermore, the outlet temperature is still very high when it leaves the cycle. The "Heat Source Out" in fig. 4.4a shows the time development of this outlet temperature which leaves the process and is lost for further usage (lost exergy is not explicitly displayed in these two qualitative figures). As a logical consequence, the cascaded heat source flow was added as major improvement to the MWM Cycle (see fig. 4.4b). Instead of having to split-up the heat source stream for all three heat exchangers, the full stream is first fed to the evaporator where the high temperature is most needed: during the discharge phase where the re-evaporation takes place. The heat source outlet of this phase is then redirected to the next heat exchanger that is, at the same time, in the evaporation phase. In fig. 4.4b, the outlet temperature of each phase is the inlet temperature of the next phase. Finally, the stream is fed to the last evaporator (which is in the filling phase), where the process temperature is low and the already cooled down heat source stream can still be used. Only the outlet of this last stage is the outlet stream of the whole cycle. The temperature match in the phases filling and evaporation is significantly improved by this new flow scheme. Only in the discharge phase the gap between the "fresh" heat source and the cooling working fluid is still critical. This issue will be further addressed in context of the effects of thermal inertia in section 6.2.2 on page 118.

It became apparent from fig. 4.4b that the evaporation phase provided the best temperature match and should be the preferred condition in the MWM

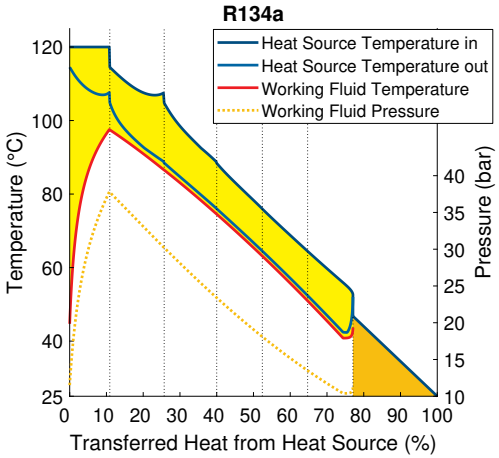

Figure 4.5: Temperature match and heat source utilization in an exemplary MWM Cycle with six heat exchangers.

Cycle. By adding more evaporators to the setup, a longer time interval could be given to the evaporation compared to filling and discharge. An exemplary setup with six heat exchangers, as shown in fig. 4.5, consist of the phases filling, evaporation 1 to 4, and discharge (again from right to left). The figure was further extended to also cover the remaining heat and exergy in the heat source stream at the end of the cycle pass. Starting at the average outlet temperature of the last cycle phase and going down to the reference temperature T_0, the orange triangular area marks the lost exergy.

The resulting progress of the cycle shows features comparable to a common continuous counter flow heat exchanger. The temperature match is smooth and almost constant over the whole domain. Even though the evaporation takes place over the whole cycle, the process temperature is gradually rising as desired and a temperature plateau can be avoided. Thereby, both exergy destruction and exergy losses are minimized.

Originally, the diagrams as in fig. 4.5 show the progress of one evaporator through all the phases of the MWM Cycle. Due to the cascading operation, each of the present evaporators is in a different phase. Therefore, as a second

interpretation, the diagram also simultaneously shows all the evaporators in their current, specific phase. This second understanding highlights the concept of the cascaded heat source flow. The heat source outlet of each heat exchanger is directly fed to the heat exchanger that is, at the same time, in the previous phase of the cycle.

With regard to the practical implementation, the cascaded heat source flow could for example be realized with a ring structure as proposed by Wieland et al. [66]. As shown in fig. 4.6 on the following page, the in- and outlets of the heat source side of the evaporators are connected in a ring. In accordance with fig. 4.4, the hot heat source is fed to HX 1 in the discharge phase (fig. 4.6a) and then passes through the other evaporators before it leaves the cycle. When one cycle phase is finished, the feed point and outlet point of this ring are switched by valve settings according to the cycle timing (see figs. 4.6b and 4.6c).

4.2 Characteristics of the MWM Cycle

Based on the previously outlined illustration of the MWM Cycle, this section lists the resulting characteristic features of the cycle—both advantageous and challenging.

4.2.1 Opportunities and Challenges of the MWM Cycle

Opportunities The MWM Cycle offers several opportunities that are also desired but not completely met by the other advanced cycle concepts:

- Perfect Temperature Match: When set-up properly, the MWM Cycle shows the almost perfect temperature match as targeted by the advanced ORCs (zeotropic and transcritical), the TLC and the other presented concepts.
- No two-phase Expansion: In contrast to the TLC, the temperature match does not come at the cost of a necessary two-phase expansion. The stream to the engine is already completely evaporated.
- Boiling Heat Transfer: The whole heat transfer is a boiling heat transfer. The heat transfer coefficients are therefore expected to be higher than for liquid heat transfer concepts (ORC preheating or TLC / OFC).

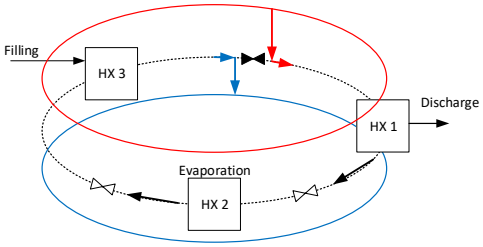

(a) Phase 1

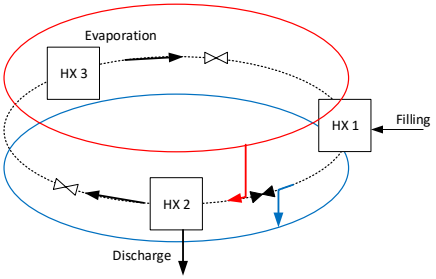

(b) Phase 2

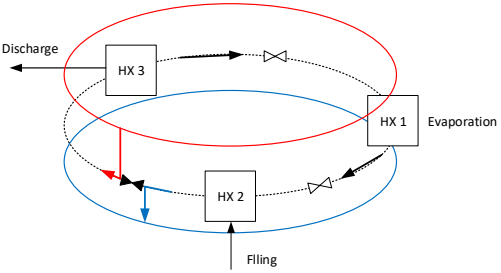

(c) Phase 3

Figure 4.6: Qualitative example of a ring structure for practical implementation of the cascaded heat source flow (hot inlet from top - red, cold outlet at bottom - blue).

- No Rapid Flash: The gradual evaporation in the heat exchanger is favorable compared to rapid flashing. The losses in the engine of the TLC, the throttle of the OFC (as presented by Ho, Mao, and Greif [12]) or the engine attachment in the concept of Steffen, Löffler, and Schaber [40] are avoided in the MWM Cycle.

Challenges The advantages come at the cost of a more complex cycle setup, where the challenges are:

- Polytropic Processes: Thermodynamic analysis is often based on the assumption of either an open + stationary process or a closed + transient process. For both of these combinations, typical model processes can be used (isobaric, isentropic, isochoric…). With the MWM Cycle being an open + transient process, none of these match. Therefore, the full mass and energy balances have to be solved for any process calculations (one exception is the closed, isochoric evaporation phase). Simple and commonly used shortcut methods and predictions from steady state simulations are hence not available and any involved simulation models become more complex.
- Timing and Process Control: The batch character of the process requires a mechanism that controls the timing of the cycle phases. The crucial parameter here is the dropping pressure in the discharging evaporator. When the current evaporator is almost empty, it is time for the next switch. However, the discharge phase thereby also determines the timing of filling and evaporation. Those lead to the available process pressure and have, in turn, a strong influence on the duration of the discharge phase. In order to manage a proper combination of all the influencing parameters (see full list in the next section) an optimization algorithm had proven to be necessary.
- Specialized Engine: Even though the expansion engine has not to be suitable for a full two-phase expansion, a specialized engine is necessary. Both the oscillating process pressure and the possible small amount of liquid fraction eliminate the usage of a common ORC turbine.
- More Heat Exchangers: The real advantages of the MWM Cycle can only be gained with several evaporators (at least three, favorably more).

Table 4.1: Independent variables of the MWM Cycle.

Independent Variable	
Total heat transfer ability per evaporator	kA_{all}
Total free volume per evaporator (HX + storage)	$V_{\text{HX},0}$
Working fluid mass flow during filling phase	$\dot{m}_{\text{WF,fill}}$
Maximum working fluid mass per filling phase	$m_{\text{WF,fill}}$
Discharge volume flow	$\dot{V}_{\text{WF,dis}}$
Switchover pressure limit	$p_{\text{WF,switch}}$

The economic impact of the additional components will be discussed in the context of the economic evaluation in section 6.4. Against the first implementations of Misselhorn and Freese [67], plate heat exchangers (PHEs) have proven to be best suited for the MWM Cycle with regard to their low costs, their high surface density[1] and their flexibility in size and type.

4.2.2 Degrees of Freedom and Design Inputs

For the stationary ORC, a direct dependency between most of the process parameters can be established beforehand and the final number of independent variables can be reduced to one or two (see section 5.2 on page 94 for a detailed model description). In contrast, the non-stationary batch process adds a whole new dimension of independent process variables. The time-dependent progress leads to a list of process variables (see table 4.1), which are connected but not predictably dependent from one another.

The combined total heat transfer ability per evaporator kA_{all} ("thermodynamic size") is used as a substitution for the geometric size of the evaporators. The free volume inside these evaporators is optionally extended by an additional vapor storage to the total volume $V_{\text{HX},0}$. The filling phase is governed by the incoming working fluid mass flow $\dot{m}_{\text{WF,fill}}$. To further shorten the percentage of the filling phase, it was favorable to use a high mass flow and stop the filling early once the maximum filling mass $m_{\text{WF,fill}}$ was reached.

[1] Ratio of heat transfer surface to total heat exchanger volume.

The discharge phase is defined by the discharge volume flow $\dot{V}_{\mathrm{WF,dis}}$ and the corresponding mass flow $\dot{m}_{\mathrm{WF,dis}}$ through the expansion engine. This volume flow results from the engine speed and engine displacement. The switching to the next cycle phase is triggered by the switchover pressure limit in the evaporators $p_{\mathrm{WF,switch}}$.

The following findings give a preview over the general relations of these process variables. They will be further discussed in detail in the following chapters:

Working fluid mass and free volume The suitable working fluid mass per cycle can be roughly estimated from the available energy flow of the heat source. The transferred energy from the heat source during one cycle has to be sufficient in order to evaporate most of the working fluid. The ratio of this total working fluid mass and the free volume defines the density ρ or rather the specific volume $v = V/m$ of the isochoric evaporation. If only the evaporator volume was available to the built-up vapor, the density was too high and the process pressure did rise rapidly. The evaporation then came to a halt after only a few seconds when the boiling temperature reached the heat source temperature. In the T-s-diagram of the MWM Cycle (see fig. 4.3 on page 56), such a high–density evaporation would follow a steep isochore close to the boiling line (even left to the isochore $v = 0.0025$). The vapor quality was still very low at the endpoint of the evaporation and the available small amount of vapor could not provide an appropriate power output in the engine.

If, on the other hand, the density was too low, all of the working fluid was already evaporated long before the desired process pressure was reached. In the T-s-diagram, the according evaporation would follow one of the isochores with only a marginal slope (see for example $v = 0.01$ in fig. 4.3). The remaining heat from the heat source was then wasted as the additional superheating of the vapor yielded only a small extra of power output.

The additional pressure storage allows to vary the total volume independently of the actual heat exchanger geometry and to adjust the ideal evaporation density.

Discharge The main influences on the discharge phase are the pressure, vapor quality and amount of available working fluid at the endpoint of the

evaporation. The operation of the engine defines the discharge volume flow and, depending on the vapor density within the evaporator, the discharge mass flow. If the discharge was too fast, the re-evaporation of the remaining liquid was too slow to keep up the process pressure. A slow discharge allowed for extensive re-evaporation, but directly affected the power output: Discharging the same mass over a longer time period t led to about the same energy output E of the engine, but a reduced power output P as $P = E/t$.

The switchover pressure limit then defines the endpoint of the discharge phase and thereby also the amount of working fluid that remains in the evaporator. Stopping the discharge at a still high process pressure allowed for a higher pressure drop over the engine and high internal efficiencies. However, during the next filling phase, the resulting higher process temperature limited the heat transfer and interfered with the heat source utilization.

Timing The cycle timing depends on a combination of all the independent variables: The right amount of working fluid has to be fed to a matching volume of the evaporator. The duration of the evaporation phase, the heat transfer and the available energy flow from the heat source have to provide a proper state of the working fluid at the endpoint of evaporation (peak pressure and adequate vapor quality with sufficient liquid for re-evaporation). The duration of the discharge phase, depending on the endpoint of evaporation, then in turn defines the time for the filling and evaporation. At last, not only the state and amount of discharged vapor but also the length of the discharge phase lead to the power output.

Summary of the MWM Cycle

The batch behavior of the MWM Cycle offers a promising temperature match of heat source and working fluid and thereby allows for a high exergy efficiency without any obvious, major drawbacks.

However, the more complex setup adds some challenges in comparison to the well–understood ORC. Primarily, the process timing of the MWM Cycle is implicitly defined and the handling is more challenging than for a continuous cycle. With regard to the model description in the next chapter, it becomes obvious from the complex relations of the input variables (which are not

completely independent after all) that the implementation of an optimization algorithm is essential in order to find a beneficial or even functional process setup.

In addition, the up-scaling of the MWM Cycle is expected to be more limited than for the ORC with regard to the necessity of an expansion engine instead of a turbine, an increasing complexity for large scale tanks and vessels and the increasing inertia of large scale components that obstructs the dynamic behavior.

Chapter 5

Model Development

This chapter describes the details of the simulation models. Section 5.1 covers the Matlab® model for the MWM simulations. This includes all layers of the model from the inner solver of the differential equations to the structural layers for optimization and parallel computation. In section 5.2, the setup of the ORC model in Aspen Plus® is introduced and explained. At last, section 5.3 gives a summary of the general thermodynamic and economic model assumptions like heat transfer correlations and cost estimation correlations.

5.1 Structure of the Matlab Model

The structure of the Matlab model is presented in fig. 5.1 on the following page. The shown layers, printed in bold, are named according to the function names in Matlab as described in the following paragraphs.

The outer layer, `setAndCallGA()`, is a GUI-aided routine for the setup of an optimization problem. The boundaries, constraints and options for the optimization are selected here as well as the reference conditions for the cycle calculations itself.

When the setup is finished, the genetic optimization function `ga()` (section 5.1.3), provided by the Matlab *Global Optimization Toolbox*, is called. Apart from the defined boundaries, linear constraints and options, the function handles[1] to the fitness function (*fitnessFunction*) and to the nonlinear-constraints function (*nonLinConstraints Function*) have to be provided. In order to eliminate an unfeasible short cycle timing, the one nonlinear constraint is the real–time duration of the cycle phases for the individual case.

[1] Matlab equivalent of pointer to a function

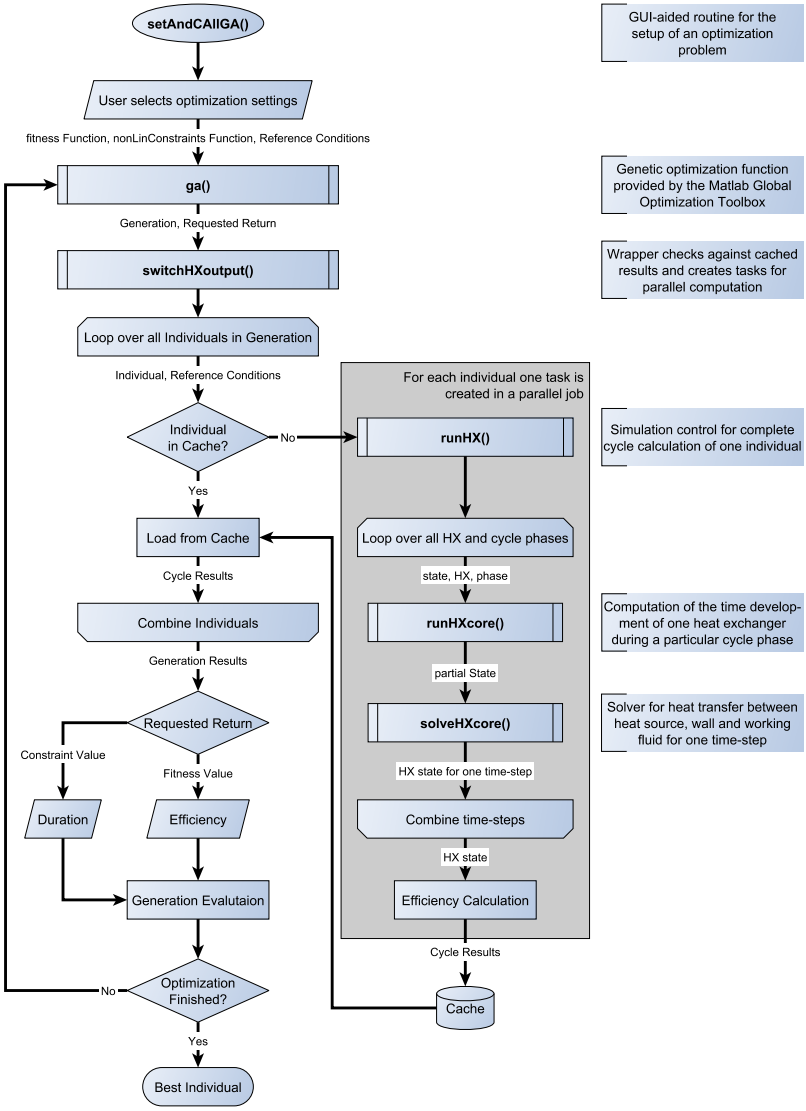

Figure 5.1: Structure of the Matlab model for the MWM Cycle.

As this duration is a result of the simulation and cannot be obtained in advance, both the handles to the fitness function and to the nonlinear constraint function point to the same cycle simulation, but expect a different response. The genetic algorithm then creates the initial generation and passes an array with all individuals of this generation to the next layer. The returned results for this generation are evaluated and are carried forward either into a new generation or into the completion of the optimization.

The next layer, `switchHXoutput()` (section 5.1.4), is merely a wrapper in order to receive the generation array (*Generation*) and the requested response (*Request Return*) from the genetic algorithm. The individuals are checked against a cache of already calculated cases and the new ones are passed on to a parallel job as individual tasks. After the parallel job is finished, the returned results are merged with the cached data and the whole output array is returned to the genetic algorithm. Depending on the request,—fitness value or nonlinear constraint—only the required results are included in the return array.

Each of the parallel tasks calls one individual instance of the actual cycle calculations `runHX()` (section 5.1.2). The required inputs are the independent variables $\vec{x}$ of this individual (*Individual*) that were defined by the optimization algorithm and the general reference conditions (*Reference Conditions*) of the current optimization problem that were chosen in the setup. All the arrays and structures for the simulation are initialized in the sub-function `initHX()` and afterwards a loop over all heat exchangers and cycle phases calls the core function of the model. For each phase of each evaporator, an average over the needed pump power and over the condenser status is computed within the loop. Once the complete time array of all process variables is finished, the different efficiencies, the duration of the cycle and the economic numbers are calculated and returned.

The core function, `runHXcore()` (section 5.1.1), computes the time development of one heat exchanger during a particular cycle phase. Besides the index of the current heat exchanger (*HX*) and the current cycle phase (*phase*), the last state (temperature, pressure, working fluid mass...) of this evaporator (*state*) is required as an input. In an inner loop over each time step *j* of the current cycle phase, first the general conditions of the incoming and outgoing working fluid streams and the incoming heat source stream are calculated. Next, the heat transfer between heat source, wall and working fluid

is solved within `solveHXcore()`, where the actual differential equations for the heat transfer are handled by the finite element solver. With all the mass flows and heat flows present, the overall balances of mass and energy are calculated for the current time step $j + 1$. Finally, all other new state variables for the heat exchanger (temperature, pressure...) result from this new state of mass and energy. The loop is finished when either the lower pressure limit (discharge phase) or the cycle timing (all other phases) is reached.

The details of the single layers are further discussed in the following sections.

5.1.1 Evaporators (runHXcore)

The main goal of this model was to better understand the general progress of the MWM Cycle and to evaluate the evaporators with regard to power output, interacting temperature levels and overall efficiency. Therefore, the detailed geometric design was postponed in order to keep a reasonable computation time with the numerous function calls resulting from the genetic algorithm. Depending on the precise question, two modules with a different level of detail were available for the evaporators. The simple 0-D model was used to cover the balances for mass and energy conservation and used only basic thermodynamic relations (see section 5.1.1.1). The more advanced 1-D cell model used a finite elements approach to actually include the differential equations for local heat transfer and also took the thermal inertia of the wall material and the enclosed heat source medium into account (see section 5.1.1.2). Still, some characteristics like pressure drop and heat transfer coefficients were estimated on a generic level in order to avoid the burden of the detailed geometry. All model assumptions are summarized in section 5.3.1 on page 97 after the introduction of MWM Matlab model and the ORC Aspen model.

As already mentioned before, the working fluid side could not be approximated with common thermodynamic model processes due to the open nature of the cycle. However, the balance equations were reduced to only one cell with uniform pressure and temperature distribution and an idealized equilibrium state. Regarding research on flash evaporation in liquid pools by Miyatake et al. [68, 69], a vapor–liquid equilibrium is reached in a time scale of only a few seconds. According to Kim and Lior [70] and Saury, Harmand, and Siroux [71], also any thermal stratification is prevented in such a pool

of boiling liquid by the stirring effect of rising bubbles. The errors from this one–cell–approach are therefore expected to be small. Despite the uniformity approach, the distinction between heat transfer to the liquid pool at the bottom and the gas phase at the top of the evaporators was considered in both heat transfer models.

The overall mass balance of the working fluid in one evaporator could thereby simply be expressed by the in- and outgoing mass flow of the working fluid

$$\frac{\mathrm{d}m_{\mathrm{WF}}}{\mathrm{d}t} = \dot{m}_{\mathrm{WF,in}} - \dot{m}_{\mathrm{WF,out}}. \tag{5.1}$$

The corresponding balance of the internal energy U contained the mass–bound enthalpy transport $\dot{m} \cdot h$ during discharge and filling as well as the total heat flow rate $\dot{Q}_{\mathrm{WF}}$ that was calculated in the evaporator models:

$$\frac{\mathrm{d}U_{\mathrm{WF}}}{\mathrm{d}t} = \dot{m}_{\mathrm{WF,in}} \cdot h_{\mathrm{WF,in}} - \dot{m}_{\mathrm{WF,out}} \cdot h_{\mathrm{WF,out}} + \dot{Q}_{\mathrm{WF}}. \tag{5.2}$$

With the evaporator volume that was defined in the setup routine (or, if optimized, varied by the genetic algorithm), the mass balance directly leads to the overall specific volume v of the working fluid. So, at the end of every time step during the call of `runHXcore()`, the thermodynamic state is defined by the specific volume v and the specific internal energy $u = U/m$. All dependent thermodynamic properties like temperature, pressure and vapor quality could then be calculated with the REFPROP Library by Lemmon, Huber, and McLinden [72] as

$$T, p, q = f(u, v). \tag{5.3}$$

The used REFPROP Library is a collection of equations of state and thermodynamic correlations for numerous fluids that can be called from MATLAB and other software.

During the discharge phase, the outgoing mass flow is calculated from the vapor density of the working fluid and the volume flow to the engine, which is in turn a result of the engine displacement and the engine speed:

$$\dot{m}_{\mathrm{WF,out}} = \rho_{\mathrm{vap}} \cdot \dot{V}_{\mathrm{eng}} = \rho_{\mathrm{vap}} \cdot V_{\mathrm{eng}} \cdot n_{\mathrm{eng}}. \tag{5.4}$$

The power output of the engine could then be calculated from the mass flow

and the specific enthalpy drop over the engine by

$$P_{\text{out}} = (h_1 - h_4) \cdot \dot{m}_{\text{WF,out}}, \tag{5.5}$$

where h_1 is the specific enthalpy of the discharged working fluid and h_4 is the remaining specific enthalpy after an isotropic expansion reduced by the losses due to the given engine efficiency. As described in eq. (A.6) on page 189, the shortcut model uses the same calculation.

During the filling phase, the feed pump has to overcome the current pressure in the evaporator. The required power can be calculated from the given ingoing mass flow and the specific enthalpy difference that the working fluid experiences. The isentropic pumping power is also scaled up by the pumping efficiency.

As already introduced in eq. (2.19), the transferred heat flow is subject to a heat transfer surface area A, a temperature difference ΔT and a heat transfer coefficient. Based on this overall approach, the heat transfer between two fluids through a wall can be separated into three sub-processes. For the heat transfer from the hot fluid to the wall, the three factors are the surface area of the wall A, the temperature difference between heat source and wall ($T_{\text{HS}} - T_{\text{wall,HS}}$) and a coefficient α_{HS} for the local convective heat transfer. In a similar way, the cold side is defined be the same surface area, the temperature difference between wall and cold working fluid ($T_{\text{wall,WF}} - T_{\text{WF}}$) and the convective heat transfer coefficient for the cold side α_{WF}. For the heat conduction within the wall, the main difference is the replacement of the convective coefficients by the ratio of heat conductivity λ to wall thickness:

$$\dot{Q} = \frac{\lambda}{s} \cdot A \cdot \Delta T_{\text{wall}}. \tag{5.6}$$

For a flat plate, these three parts are typically combined to the total heat transfer as in eq. (2.19), where the total heat transfer coefficient then is

$$\frac{1}{kA_{\text{all}}} = \frac{1}{\alpha_{\text{HS}} A} + \frac{s}{\lambda_{\text{wall}} A} + \frac{1}{\alpha_{\text{WF}} A}. \tag{5.7}$$

For both model approaches, this combined total heat transfer ability kA_{all}

is used as an optimized variable in substitution for the geometry of the heat exchangers. The upper and lower boundaries for typical values were estimated from heat transfer correlations as shown in section 5.3.1 on page 97. The actual total heat flow rate for the energy balance is then either computed with the NTU–approach (section 5.1.1.1) or the more detailed finite differences approach (section 5.1.1.2).

5.1.1.1 NTU–Approach (solveHXcore)

With the assumption of a constant overall heat transfer coefficient k, constant fluid properties and a stationary flow, a stationary total heat transfer can be estimated by the NTU–approach (Number of Transfer Units) as presented for example by Polifke and Kopitz [73]. For the dynamic MWM Cycle, each time step was approximated by such an individual stationary calculation.

The non-dimensional heat transfer ability

$$NTU = \frac{k \cdot A}{\dot{C}_{\mathrm{HS}}} \tag{5.8}$$

sets the known heat transfer ability kA in relations to the available heat capacity flow of the heat source $\dot{C}_{\mathrm{HS}} = c_{p,\mathrm{HS}} \cdot \dot{m}_{\mathrm{HS}}$. For the limited duration of one time step, the working fluid temperature in the MWM Cycle could be approximated as constant and, according to [73], the stationary heat exchanger efficiency for this instant is then analytically defined by

$$\epsilon = 1 - \exp\left(-NTU\right). \tag{5.9}$$

The actual transferred heat flow $\dot{Q}(t)$ at the time t could then be calculated from the efficiency and the maximal available heat flow $\dot{Q}_{\max}$ by

$$\dot{Q}(t) = \epsilon \cdot \dot{Q}_{\max} = \epsilon \cdot \dot{C}_{\mathrm{HS}} \cdot \left(T_{\mathrm{HS,in}} - T_{\mathrm{WF}}(t)\right). \tag{5.10}$$

In order to cover the different heat transfer coefficients of boiling heat transfer and vapor-phase heat transfer, the evaporator is split in two sections in a moving boundary approach. First, the bottom part up to the liquid level (LL) is calculated with eqs. (5.8) to (5.10) and a partial surface area matching

the contact area of the liquid. The end temperature of this calculation

$$T_{\mathrm{HS,LL}} = T_{\mathrm{HS,in}} - \epsilon \cdot \left(T_{\mathrm{HS,in}} - T_{\mathrm{WF}}(t)\right) \tag{5.11}$$

is used as heat source input temperature of the analogous calculation of the top part only with the gas–phase heat transfer coefficient (see section 5.3.1) and the remaining surface area. The combined heat transfer of bottom and top section is then returned to *runHXcore* where it is used for the update of the thermodynamic state. With the progress of the cycle and the changing liquid volume, the area fraction changes for every time–step.

The stationary approximation of every time step does, however, not include the residence time of the heat source within the evaporators. When for example the heat exchangers switch from the discharge phase to the filling phase, the temperature of the heat source inlet stream instantly drops. While the hot heat source in a real heat exchanger would still need some time to be flushed out, the NTU–approach does not know about the history of the previous time-steps and would simply assume a stationary process with the current inlet temperature. While this approach is extremely fast with regard to computation time and gives a good first idea of the general process, it also causes some uncertainty of the simulation model.

5.1.1.2 Finite Differences Approach (solveHXcore)

The alternative approach which is based on finite differences allows for a much more detailed analysis of the heat transfer. Still, the evaporators were only modeled as far as necessary in order to reduce computation time. The exact dimensions and structure of the plates within the heat exchangers would only be needed for the calculation of the flow velocity and the pressure drop which, in turn, would lead to the heat transfer coefficients. With the heat transfer coefficients being directly set by the optimization algorithm, the calculation of the intermediate properties could be skipped and the required geometry inputs were reduced. With this simplification, the plate-stack and the surrounding fluid–layers of a model heat exchanger could be reduced to one single plate with the same thermodynamic dimension *kA* that showed an equivalent thermodynamic behavior (see fig. 5.2 on the facing page). In contrast to the NTU–approach, the heat transfer was actually modeled separately

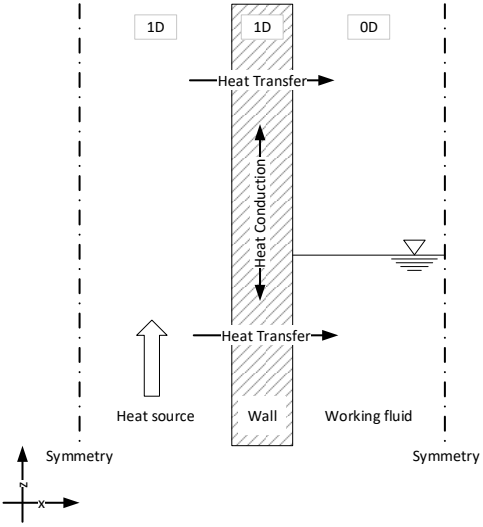

Figure 5.2: System boundaries for the finite–differences plate heat exchanger model.

for heat source, wall and working fluid.

The heat source (left-hand side in fig. 5.2) was approximated as one-dimensional forced flow (uniform along x-axis). Without any phase changes and only moderate variations in temperature and pressure, all dependent fluid properties like density and heat capacity were assumed to be constant. With the constant mass flow of an assumed incompressible fluid, the momentum equation and mass balance could also be neglected in favor of an immediate propagation of the inlet mass flow. Furthermore, the axial heat conduction was not considered as it is outweighed by the flow rate of the heat source medium. Similar to the side of the working fluid (eq. (5.2)), the equation for energy conservation thus includes the mass–bound heat transport and the heat transfer to the wall. However, the differential equations cover not only the global but also the local aspects along the z-axis and include the pressure drop caused by friction and gravitation as well.

Following the implementation of the heat source flow, the wall was also

simplified as one-dimensional part of the model. The spatial discretization along the z-axis matched the heat source. The temperature profile along the x-axis of the wall was neglected as the temperature distribution across the wall can be assumed as uniform in good approximation: The Biot-number

$$\mathrm{Bi} = \frac{\alpha}{\lambda_{\mathrm{wall}}/L_0} \tag{5.12}$$

sets the heat transfer to the plate in relation to the heat conduction within the plate [74]. The characteristic length L_0 is in this case the plate thickness s_{wall}. A small Biot Number[2] shows that the heat conduction is much faster than the heat transfer for common plate dimensions. Any transferred heat will therefore be quickly spread over the x-dimension of the wall and the error from the 1-D estimation is small. In contrast, along the height of the plate, the heat transfer is the governing effect over the minor heat conduction due to the small cross–section of the plate. Even though the heat source flow was expected to predominate the temperature profile, the longitudinal heat conduction was still implemented with regard to the heat flow near the liquid level. While simplifying the effects of heat transport, the model is focused on the conservation of heat and the thermal inertia of wall material and fluids.

The side of the working fluid (right-hand side) is again only represented by a single, homogeneous cell as it was presented for the NTU–model. However, instead of the global heat transfer calculations, the heat flow to the working fluid $\dot{Q}_{\mathrm{WF}}$ is computed in context of the wall calculations and therefore includes the local temperature differences and the influence of the transfer mechanism (boiling or gas-phase convection).

In order to provide all required data based on the rather reduced geometric input, the following relations were used:

- The virtual plate surface A_{virt} could be calculated from kA_{all} by using the estimated ratio of the heat transfer coefficients from section 5.3.1

[2] For an exemplary heat transfer coefficient $\alpha_{\mathrm{HS}} = 8000\,\mathrm{W/(m^2{\cdot}K)}$, a heat conductivity of $\lambda = 50\,\mathrm{W/(m{\cdot}K)}$ and a plate thickness of $s = 1\,\mathrm{mm}$, the small Biot-number $\mathrm{Bi} \leq 0.16$ justified the assumed uniformity.

and the wall conductivity on eq. (5.7):

$$A_{\text{virt}} = kA_{\text{all}} \cdot \left(\frac{1}{\alpha_{\text{HS}}} + \frac{s}{\lambda_{\text{wall}}} + \frac{1}{\alpha_{\text{WF}}} \right). \tag{5.13}$$

- In addition to kA_{all}, the genetic algorithm also optimizes the plate thickness s and the amplitude of the chevron structure a for the detailed model. The nomenclature of the plate geometry was chosen in accordance with the definition of Martin [75] in his heat transfer correlations (see appendix A.3.1). With these two additional inputs, the thermal mass of the wall material m_{wall} and of the enclosed heat source fluid m_{HS} can be calculated. The mass of the wall is simply defined by the volume of the wall material (surface times thickness) and its density (eq. (5.14)).

$$m_{\text{wall}} = A_{\text{virt}} \cdot d \cdot \rho_{\text{wall}} \tag{5.14}$$

$$m_{\text{HS}} = A_{\text{virt}} \cdot a \cdot \rho_{\text{HS}} \tag{5.15}$$

  The volume of the enclosed heat source was derived from the average distance of two plates. In between the connecting peaks of two neighboring plates, the wavy structure builds flow channels with an average distance of $2a$. As each of the two involved plates is associated to one half of the flow channel, the model plate is in interaction with a fluid layer of the thickness a (compare eq. (5.15) to fig. 5.3).

- The calculation of the flow velocity of the heat source medium would require the defined number, layout and size of the plates. While this velocity would be needed for the calculation of local heat transfer coefficients, the energy balance can also be satisfied with the more general residence time τ. Independently of the actual geometry, the dwell time is always, even for the single model plate, defined by the mass flow and the enclosed mass by

$$\tau = \frac{m_{\text{HS}}}{\dot{m}_{\text{HS}}}. \tag{5.16}$$

- The last step in order to omit the exact geometry is the definition of a

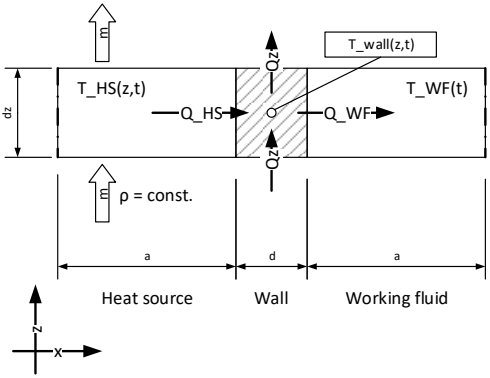

Figure 5.3: Detailed control volume of the plate heat exchanger as shown in fig. 5.2.

dimensionless z-coordinate for the differential equations. By referring the size of one finite step Δz to the whole length L, a dimensionless fraction z_{frac} and the total number of cells/steps could be set in relation:

$$z_{\text{frac}} = \frac{\Delta z}{L} = \frac{1}{N_{\text{cells}}}. \tag{5.17}$$

Again, the length of the plate would only affect the velocity and by this the heat transfer and pressure drop. As both of them are already defined otherwise, the length has no further influence on the model as long as all other factors are scaled down to the cell– or step–size using their dimensionless fraction of the whole surface area or length, respectively.

With this set of simplifications, all necessary parameters of the heat exchanger geometry could be reduced to the heat transfer ability, the plate distance and the plate thickness.

Energy Balances and Differential Equations As presented by Gleinser, Wieland, and Spliethoff [55], balancing all in- and outgoing parts of one fluid

volume of the **heat source side** as shown in fig. 5.3 leads to the energy balance

$$\frac{\partial \Delta U}{\partial t} = +\dot{H}_z - \dot{H}_{z+\Delta z} - \dot{Q}_{x,\mathrm{HS}}, \tag{5.18}$$

with the energy storage of one cell ΔU on the left-hand side and the mass–bound heat transport $\dot{H}$ as well as the heat transfer to the wall $\dot{Q}$ on the right. Following the detailed derivation in appendix A.2.1 on page 191 leads to

$$m_{\mathrm{HS}} \cdot z_{\mathrm{frac}} \cdot c_p \cdot \frac{\partial T_{\mathrm{HS}}}{\partial t} = -\dot{m}_{\mathrm{HS}} \cdot \frac{\partial h}{\partial z} \Delta z - z_{\mathrm{frac}} \cdot kA_{\mathrm{HS}} \cdot (T_{\mathrm{HS}} - T_{\mathrm{wall}}) . \tag{5.19}$$

The missing information about the detailed dimensions of the plate was compensated by applying z_{frac} from eq. (5.17) on the whole heat source mass and the whole heat transfer ability. The hot–side heat transfer kA_{HS} was derived by splitting the total heat transfer kA from eq. (5.7) according to the ratio of hot and cold heat transfer coefficients α_{HS} and α_{WF} as

$$kA_{\mathrm{HS}} = kA_{\mathrm{all}} \cdot \left(1 + \alpha_{\mathrm{HS}} \left(\frac{d}{\lambda_{\mathrm{wall}}} + \frac{1}{\alpha_{\mathrm{WF}}} \right) \right) . \tag{5.20}$$

With the assumption of an incompressible fluid, the derivative of the enthalpy can be substituted by $\mathrm{d}h = c_p \, \mathrm{d}T + v \, \mathrm{d}p$ (see for example Baehr and Kabelac [23]). Solving eq. (5.19) for the time derivative and applying the relations from eq. (5.17) where needed results in the final differential equation

$$\frac{\partial T_{\mathrm{HS}}}{\partial t} = - \underbrace{\frac{1}{\tau} \cdot L}_{\text{constant}} \cdot \left(\frac{\partial T_{\mathrm{HS}}}{\partial z} - \underbrace{\frac{1}{\rho_{\mathrm{HS}} \cdot c_p} \cdot \frac{\partial p}{\partial z}}_{\text{constant for } \partial p / \partial z = \Delta p / L} \right) - \underbrace{\frac{kA_{\mathrm{HS}}}{m_{\mathrm{HS}} \cdot c_p}}_{\text{constant}} \cdot (T_{\mathrm{HS}} - T_{\mathrm{wall}}) . \tag{5.21}$$

The change in temperature over time is subject to the flow–bound heat transport, the pressure drop along the fluid flow and the heat transfer to the wall. When the total pressure drop Δp, which is set as an input condition to the simulation, is distributed equally over the whole domain L, all the prefactors become constants and the energy balance is reduced to a solvable ordinary

differential equation.

Even though the length L is still present in this final equation, its insignificance can be explained as follows:

- The first occurrence is in context of the flow velocity

$$\mathrm{v} = L/\tau.$$

  As already explained, the velocity is not actually needed as the pressure drop and heat transfer coefficients are input parameters to the simulation and the flow speed was therefore replaced by the dwell time τ. If now two plate dimension of the same surface area (for example $a \cdot 2b$ and $2a \cdot b$) were compared, the longer one would result in a faster flow velocity. However, from the perspective of a dimensionless length, the fluid would always take the same time to reach 50 % or 100 % of the length. So when dividing the two plates into the same number of cells, the combination of longer cells but faster flow would show the exact same dimensionless wave propagation as the shorter (but wider) cells together with the slower flow. Moreover, the area-fraction of the cells would also be the same and therefore result in an identical heat transfer.
- The same logic applies to the distribution of the pressure drop. Irrespective of the actual length, the total pressure drop has to sum up to the given Δp and the proportionate, dimensionless distribution is independent of the actual dimensions. When the pressure drop is approximated by $\frac{\partial p}{\partial z} \approx \frac{\Delta p}{L}$, the length L is canceled in the pressure factor.

In fact, even the above given first occurrence of the length L will finally be canceled in the equation of the solver (eq. (5.30)). The length could therefore be set to any value (in this model $L = 1\,\mathrm{m}$) and the plate layout (number of plates, width, length) has no influence on the result as long as all further analysis and calculations are consistently based on the dimensionless z-fraction.

The fundamental differential equation for the **wall side** follows from the control volume (fig. 5.3) as

$$\frac{\partial \Delta U}{\partial t} = \dot{Q}_{x,\mathrm{HS}} - \dot{Q}_{x,\mathrm{WF}} + \underbrace{\dot{Q}_z - \dot{Q}_{z+\Delta z}}_{\text{(I)}}. \tag{5.22}$$

Similar to the equation for the heat source, the energy balance includes a storage term ΔU on the left side and the heat transfer from the heat source $\dot{Q}_{x,\mathrm{HS}}$ and to the working fluid $\dot{Q}_{x,\mathrm{WF}}$ on the right. In addition, the last term (I) represents the heat conduction along the z-axis of the plate. Rewriting the equation following the steps in appendix A.2.1 results in

$$\begin{aligned} m_{\mathrm{wall}} \cdot z_{\mathrm{frac}} \cdot c_{\mathrm{wall}} \frac{\partial T_{\mathrm{wall}}}{\partial t} = & + z_{\mathrm{frac}} \cdot kA_{\mathrm{HS}} \left(T_{\mathrm{HS}} - T_{\mathrm{wall}}\right) \\ & - z_{\mathrm{frac}} \cdot kA_{\mathrm{WF}} \left(T_{\mathrm{wall}} - T_{\mathrm{WF}}\right) \underbrace{- A_{\mathrm{cross}} \cdot \frac{\partial \dot{q}}{\partial z} \cdot \Delta z}_{\text{(I)}} . \end{aligned} \tag{5.23}$$

While the heat transfer is defined by the known factors (total heat transfer ability and temperature difference), the heat conduction (I) is composed of the cross–section of the wall A_{cross} and the heat flux gradient $\frac{\partial \dot{q}}{\partial z}$ over one cell Δz. The cold–side heat transfer was derived in analogy to its hot side counterpart in eq. (5.20) by

$$kA_{\mathrm{WF}}(z) = kA_{\mathrm{all}} \cdot \left(1 + \alpha_{\mathrm{WF}}(z) \left(\frac{1}{\alpha_{\mathrm{HS}}} + \frac{d}{\lambda_{\mathrm{wall}}}\right)\right). \tag{5.24}$$

For all cells below the liquid level of the pool of working fluid, the boiling heat transfer was used, whereas the free convection was considered for those above. When applying Fourier's law ($\vec{q} = -\lambda \operatorname{grad} T$) and solving the whole energy balance for the time derivative of the wall temperature (see again appendix A.2.1), the term (I) becomes

$$+ \frac{A_{\mathrm{cross}} \cdot \Delta z}{m_{\mathrm{wall}} \cdot z_{\mathrm{frac}}} \cdot \frac{1}{c_{\mathrm{wall}}} \cdot \lambda \frac{\partial^2 T}{\partial z^2} . \tag{5.25}$$

Applying the relations for the dimensionless length from eq. (5.17), the left factor could be rewritten as

$$\frac{A_{\mathrm{cross}} \cdot L}{m_{\mathrm{wall}}} = \frac{V_{\mathrm{wall}}}{m_{\mathrm{wall}}} = \frac{1}{\rho_{\mathrm{wall}}} \tag{5.26}$$

and the final form of the wall energy balance follows as

$$\frac{\partial T_{\text{wall}}}{\partial t} = \frac{1}{m_{\text{wall}} \cdot c_{\text{wall}}} \cdot (kA_{\text{HS}} \cdot \Delta T_{\text{HS}} - kA_{\text{WF}} \cdot \Delta T_{\text{WF}}) + \frac{\lambda}{\rho_{\text{wall}} \cdot c_{\text{wall}}} \cdot \frac{\partial^2 T_{\text{wall}}}{\partial z^2}. \tag{5.27}$$

The time derivative of the wall temperature is hence subject to the in- and out-going heat flow and to the internal temperature "diffusion" along the z-axis of the wall.

The total heat flow to the working fluid $\dot{Q}_{\text{WF}}$ for eq. (5.2) results from the integration of the heat transfer part of eq. (5.27) as

$$\dot{Q}_{\text{WF}} = \int_{z=0}^{L} kA_{\text{WF}} \cdot \Delta T_{\text{WF}}(z)\, \mathrm{d}z \tag{5.28}$$

or, in terms of a finite element approach, from the sum over all cells of the wall

$$\dot{Q}_{\text{WF}} = \sum_{n=1}^{N_{\text{cells}}} kA_{\text{WF}} \cdot \Delta T_{\text{WF}}(z) \cdot z_{\text{frac}}. \tag{5.29}$$

Model Discretization and Solver Even though all the differential equations could be rearranged in order to resemble common differential equations they cannot be solved analytically. To select the proper numerical approach, first the type of each problem has to be identified.

The heat source flow from eq. (5.21) is a flux-conservative initial value problem, where the fluid conditions propagate over time with the fluid flow. For the initial state at $t = 0$ the values from previous simulations, a steady-state approximation or simply a constant temperature and pressure can be used. Starting from the given inlet conditions at $z = 0$, the fluid propagation over time and space can then simply be calculated "step by step". According to Press [64], typical algorithms for these hyperbolic equations are the Lax method, the explicit upwind scheme and fully implicit schemes. For the rather simple flow problem on the heat source side, an explicit upwind scheme was chosen. As shown in fig. 5.4 on the facing page, the grid points were placed on the cell borders in order to better cover the flow issues and to have direct access to the inlet and outlet properties. The average temperature needed for the

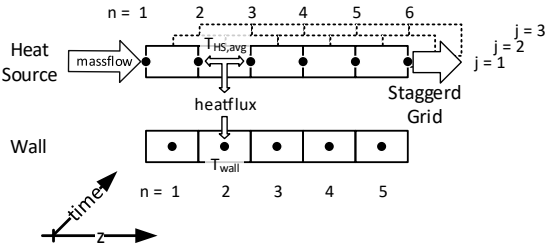

Figure 5.4: Qualitative example of a grid over the heat exchanger height z and the time t: a cell-average heat source temperature is computed for heat flux calculations.

heat transfer calculations was computed as the mean value of the cell borders by $T_{\mathrm{HS,avg}} = 1/2 \cdot (T^j_{\mathrm{HS,n-1}} + T^j_{\mathrm{HS,n}})$. The discretization for the explicit upwind approximation is defined by

$$\begin{aligned} \frac{T_n^{j+1} - T_n^j}{\Delta t} &= -\mathrm{v} \cdot \frac{T_n^j - T_{n-1}^j}{\Delta z} + C_1 \\ &= -\frac{\cancel{L}}{\tau} \cdot \frac{T_n^j - T_{n-1}^j}{z_{\mathrm{frac}} \cdot \cancel{L}} + C_1, \end{aligned} \tag{5.30}$$

where n is the spatial index and j is the time index. The flow velocity v and the further summands C_1 were taken from eq. (5.21). At this point, the last occurrence of the length L (included in the velocity) can be replaced by the fraction z_{frac} and the dwell time τ, and this leads finally to an equation that is completely independent of the plate dimensions.

In contrast to the initial flux problem of the heat source, the wall resembles a diffusive initial value problem. Without the flux–driven distinct direction of the property propagation, there is no spatial start or end for the computation. Instead, an overall equilibrium of the diffusive effects has to be found for every time–step. According to Press [64], typically fully implicit schemes or the Crank–Nicholson-Scheme should be used. In order to solve the resulting large systems of equations, advanced algorithms like the shooting method or relaxation methods become necessary. One alternative for parabolic equations

with rather simple diffusive problems is the explicit FTCS scheme (forward time centered space), where the solver is solely based on the propagation in time. While the implicit approaches tend to be more stable as they converge to the equilibrium of the transport phenomenons, the explicit schemes are more accurate regarding energy conservation [64]. The latter ones therefore not only reduce the complexity of the model, but also match the focus of this model being the thermal inertia and heat capacity. To support the model quality of the energy conservation, the grid points were placed in the center of each cell (see fig. 5.4). Applying the FTCS scheme to eq. (5.27) leads to

$$\frac{T_n^{j+1} - T_n^j}{\Delta t} = D \cdot \frac{T_{n-1}^j - 2T_n^j + T_{n+1}^j}{(\Delta z)^2} + C_2 \tag{5.31}$$

with the diffusion coefficient $D = \lambda/(\rho c_\mathrm{p})$ and the further summands C_2. The spatial temperature distribution is based on both neighboring cells $n-1$ and $n+1$. The two cells at the top and bottom edge of the wall have only one neighbor, but an adiabatic border as second condition. The discretization scheme hence simplifies to only one actual temperature difference $\left.\frac{\Delta T}{\Delta z}\right|_{\text{inside}}$ and one virtual temperature difference $\left.\frac{\Delta T}{\Delta z}\right|_{\text{edge}} = 0$ representing the adiabatic heat flux $\dot{q} = 0$ for the two ends of the plate.

At the end of the call of the solver, the array with the thermodynamic properties of the heat source and working fluid as well as the transferred heat flows of the next time–step is returned to the *runHXcore*–layer, where the new thermodynamic state of the evaporator is calculated.

5.1.2 Simulation Sequence (runHX)

It becomes apparent from the detailed description of the solvers that the input of several starting values is mandatory for the computation. All the initial values over the spatial axis for the first time–step $t = 0$ can simply be estimated from a steady–state calculation. However, the spatial initial values at $z = 0$ have to be provided for every time–step. On account of the cascaded heat source flow, only one evaporator at once is fed with the known constant temperature heat source. The calculation procedure therefore always has to

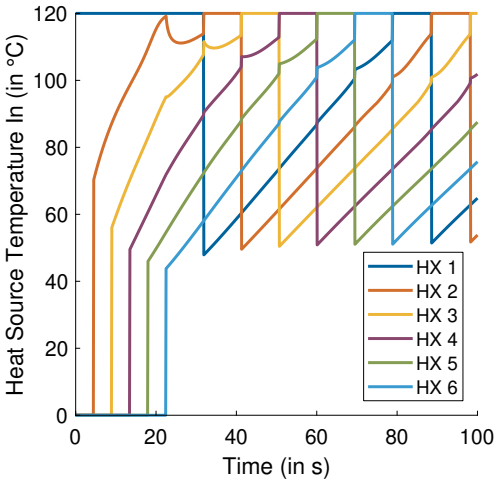

Figure 5.5: At the start-up of the process, the heat source cascade only gradually builds up due to the initial lack of fully developed states of the evaporators.

start with the respective heat exchanger and then its time dependent outlet conditions serve as input to the evaporator that is in the consecutive phase. As introduced in the cycle description in section 4.1, the hot heat source is fed to the discharge phase, passes through the evaporation phase and finally reaches the filling phase.

So, at the beginning of the computation, when all evaporators are just in their initial state, there are no evaporation phases or discharge phases to be calculated yet. During this start-up process, the first heat exchanger gets the heat source feed whatever phase it is in and the cascade only gradually builds-up (see fig. 5.5). Those first evaporation phases tend to be unstable due to the excessive heat addition of the full heat source temperature. Especially in context of the optimization, it did therefore prove to be beneficial to store the last state of the best individual of every generation. The initialization of all individuals in the next generation could then be started from this state which includes temperature and pressure distribution, current working fluid

mass, internal energy and vapor quality of all heat exchangers.

Once the first heat exchanger reaches the discharge phase, its second filling phase can be fed with the heat source outlet of the other, now also initialized, evaporators. The computation order then obviously has to be swapped for every cycle phase: always starting with the discharging evaporator and ending with the filling one, one heat exchanger after the other, and then going on to the next phase.

In contrast to the time–step–individual calculation of states (power output and feed pump power), the auxiliary components are only computed on a cycle–phase–based average. After the runs of *runHXcore* for all heat exchangers of one cycle phase are finished, the average condenser performance is computed. Due to the good mixing and the inertia of the working fluid mass in the condenser, an independent calculation for every time step could in good approximation be neglected. The outlet enthalpy after the engine h_{exp} is already known from the power calculation of the discharge in eq. (5.5). The state after the condenser h_{cond} is furthermore defined by the given heat sink properties and the chosen pinch point in the condenser (see section 6.1 on page 105). Summing up the enthalpy difference of each time step over one phase leads to the total energy that has to be dissipated by the condenser:

$$E_{\mathrm{cond}} = \sum^{\text{cycle phase}} \Big(h_{\mathrm{exp}}(t) - h_{\mathrm{cond}}(t) \Big) \cdot \dot{m}_{\mathrm{WF,\,out}}(t) \tag{5.32}$$

In order to approximate the size of the condenser, the temperature levels of the working fluid flow and the heat sink have to be compared. The averaged specific enthalpy after the engine $\overline{h}_{\mathrm{exp}}$ and the expansion pressure can be used to get the average expansion temperature $\overline{T}_{\mathrm{exp}}$ from REFPROP. The temperature levels and the sizing of the condenser can then be estimated similar to the shortcut model of the evaporator in appendix A.1. Those temperature levels finally lead to the needed heat sink mass flow and also to the required power of the according auxiliary pump (The detailed calculations are described in appendix A.2.2 on page 195). The necessary average power to compensate for the pressure drop of the heat source in the evaporators is also calculated for each cycle phase at this part of the model.

With all the mass flows, energy flows and power input/output computed, the final calculation of the efficiencies can be performed. In addition to the

thermodynamic efficiencies from section 2.1.1, the economic values from section 2.2 are calculated here. The results–structure with all efficiencies, economic indicators and characteristic values (like the cycle duration needed for the nonlinear–constraint condition) are then returned to the superordinate layer *switchHXoutput* for one complete process run (ten full cycles of the process in order to fully develop the heat source cascade and the evaporation conditions).

5.1.3 Optimization (ga)

The outer layer contains the optimization structure itself. Fed with the global target and the general requirements, the genetic algorithm creates generation after generation of sets of inputs variables and initiates them to be solved — neatly packed in a vectorized array for each generation and ready for parallel computation. While the default options of the *global optimization toolbox* can handle almost any problem, some specific adjustments drastically reduce the computation time and increase the quality of the results.

The ga expects that the call of the fitness function, here the *SwitchHXoutput*–wrapper, returns the fitness values of each individual in the same order and array–dimension as the input array. As typical for optimization algorithms, the ga minimizes the fitness value. In order to find the highest efficiency, the fitness function therefore returns the negative values of the cycles. For better handling, any fitness value is furthermore scaled to a dimension of 100 %: fitfun $= -100 \cdot \eta$. When the annuity is chosen as target of the optimization, the scaling is set to fitfun $= -10^{-4} \cdot A_{\mathrm{N}}$, which yields, in the scope of this research, a value in the same order of magnitude as for the efficiencies. If an individual causes an error in the calculation (for example when the pressure or density limits are reached), a positive penalty value is returned. A general offset of +5 ensures a distinction from possible negative annuities (which would, scaled by -10^{-4}, also give a positive fitness value). On top of that, the penalty is increased by +1 for each cycle pass that is missing to the completion of the simulation (+10 if the error occurs in the init or during the first phase, +1 if the error comes up in the last of the ten repetitions). Those dynamic penalties ensure that during the first random generations a differentiation between poor and very poor individuals is made, while for the later generations any failing sets are excluded from further consideration.

The considered range for any of the optimized input variables should be limited by a lower and upper boundary. Even when almost nothing is known about the expected optimized value, any physical value can usually at least be limited by their sign and a rough order of magnitude. An unlimited input will be varied by the algorithm in the range from $-\infty$ to $+\infty$ and numerous generations will be necessary until even a feasible region is found. For later optimizations, when the expected outcome can be narrowed down, properly set boundaries significantly improve the optimization performance. The initial boundaries were therefore always set in accordance with typical values from literature (see section 6.1 for a detailed list).

Some additional information is given to the solver in form of the linear constraints. The toolbox provides an option where equalities and inequalities between any of the optimized input variables can be defined by a matrix A of prefactors and an array b of conditions where $A * \vec{x} \leq b$ and $A_{\mathrm{eq}} * \vec{x} = b_{\mathrm{eq}}$. Those are then already considered during the creation of individuals and infeasible combinations are avoided even before the actual calculations. In this model there are no equalities and only one possible inequality constraint: if both the outlet pressure of the expansion engine and the pressure limit that marks the end of the discharge phase are optimized (even though the former one is mostly set to the minimal possible value and not varied at all), the pressure limit has to be higher than the pressure after the engine. If only one of the two is included in the optimization, the limitation is added to the static boundaries instead.

More complex relations can be given as non-linear constraints. The solver here accepts a function handle to any function that returns any number of constraints $\vec{c}$ which have to be smaller than zero. As those relations are not predictable by the solver, they are also part of the optimization. The non-linear constraints might still be violated during the first generations and will only be met in the end due to harder internal penalties. While this feature is intended for direct non-linear relations between the input variables $\vec{c} = f(\vec{x})$, it is here used to handle the limitation of the cycle timing: early optimizations showed that a rapid switching of cycle phases ($< 1\,\mathrm{s}$) sometimes lead to extremely high calculated efficiencies while not being practical at all. Simply giving those individuals a high penalty like the faulty cases might, on the other hand, completely eliminate promising individuals and therefore the non-linear constraints were chose as “soft” limitations. The solver itself only

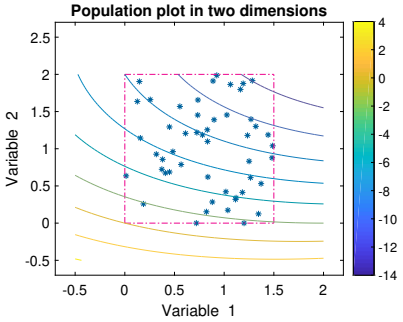

Figure 5.6: Example of an initial generation of the default creation function for two variables with boundaries. The contour plot in the background shows the fitness function. [76]

provides the varied input variables $\vec{x}$ to the constraint function as it expects a direct relation between them. The cycle duration, however, is a final result of the simulation. The handle of the non-linear constraint function therefore also leads to the *SwitchHXoutput*–wrapper and calls the full simulation run (only this time with the request for the return of the duration). The returned duration for one complete cycle t (filling, evaporation, discharge) should then at least be 4 s per phase. In terms of the solver this is expressed by $c \leq 0$, where $c = (n_{\mathrm{HX}} \cdot 4\,\mathrm{s}) - t$. The detailed functionality of the shared wrapper function is explained in section 5.1.4.

The ga toolbox also offers a functionality to optimize integer values. In terms of optimization, non-float variables like the number of heat exchangers call for a special algorithm and have therefore to be defined specifically. Simply giving their position(s) within the variables array $\vec{x}$ is enough, and they are optimized together with the "normal" inputs. However, in practice it showed that better results could be reached by running separate optimizations with a fixed number of heat exchangers.

The last peculiarity in this model is the creation function for the first generation. The default function creates random, normally distributed individuals within the boundaries (see fig. 5.6). The contour plot in the background

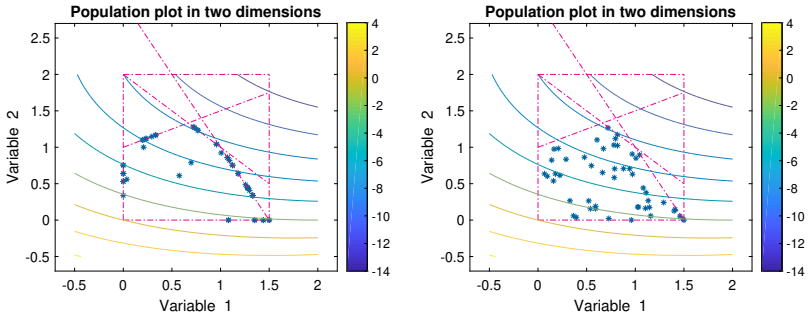

(a) Initial generation of the alternative creation function for two variables with boundaries and linear constraints.

(b) Initial generation of the custom creation function for two variables with boundaries and linear constraints.

Figure 5.7: Initial generations including linear constraints.

represents the exemplary fitness function

$$f(x) = \frac{x_1^2}{2} + x_2^2 - x_1 x_2 - 2x_1 - 6x_2 \tag{5.33}$$

as used in the MATLAB documentation [76]. The optimum—which is the minimal value— lies in the upper right corner. When linear constraints are added, a different creation function is automatically selected which assumes that the constraints are actually limiting the fitness function and places most of the initial individual on or close to those constraints (for fig. 5.7a this assumption is correct). However, if general constraints are added, they might be far away from the optimum and gathering most of the initial values there obstructs the optimization. Therefore, a custom creation function was used which scales the normal distribution of the default function to comply with the given constraints. As can be seen in the lower right corner of fig. 5.7b, this disturbs the perfect normal distribution, but still provides a better start than the generic function. With the default creation function, it repeatedly happened that the random initial generation did not include any feasible individuals and the algorithm would abort after several unsuccessful generations.

5.1.4 Parallel Computation (switchHXoutput)

From the structure of the genetic algorithm it becomes clear that the genetic optimization is perfectly suited for parallel computation. With all the individuals within one generation being completely independent of one another and also from their order of computation, these optimization problems are "embarrassingly parallel". Separating the individuals into single tasks creates a parallel problem, where absolutely no communication is needed between the tasks and almost no computational overhead is created. Hence, the total computation time scales almost directly with the number of available cores. The ga from the global optimization toolbox already provides a simple option that activates parallel computation and then runs on a local MATLAB parallel pool.

As mentioned above, both the fitness function handle and the non-linear constraints function handle point to the same function in the end. The wrapper *switchHXoutput* is the interface between the different requests from the ga and the actual model *runHX*. Except for the earliest generations, most individuals should be feasible with regard to the non-linear constraint and therefore almost any of them would be calculated twice. While this is tolerated for very fast fitness functions, one computation of *runHX* takes about 1 min to 5 min on a single core of a state-of-the-art CPU. At this speed, the overhead of caching and reloading the results is beneficial compared to a recalculation. With the call for the duration (which comes first), the individual is computed and the results (duration, efficiencies and economics) are cached. For any subsequent call of the same individual, either for the fitness value or in any later generations, the stored results are loaded and returned.

This advanced functionality is obviously not directly supported by the ga-toolbox. Therefore, the *vectorized* option is used, where the ga simply sends the whole generation to the functions in one array and lets them handle the computation. The *switchHXoutput* then checks the individuals against the cache. Any new ones are put into separate tasks and bundled into one parallel job that is solved on the workers of a local MATLAB Cluster on a multi-CPU workstation. Their results are merged with the loaded results of the previous generation and are also stored in the cache for later use.

Considering that for almost any individual the call for the duration is followed by the request of the fitness function, the caching reduces the com-

putations by $\eta_{\text{caching}} \approx 50\,\%$. The additional overhead of storing the data and looking up previous results should already be more than compensated by the recurring *elite children* that make it to the next generation and can also be loaded from the cache. The remaining half is further reduced to the fraction $\eta_{\text{parallel}} = 1/n_{\text{cores}}$. A typical number of 20 000 function calls[3] can for example be computed in about 8 %[4] of the original time on a modern workstation. With about 1 min per function call this still takes more than one day for a simple optimization. And when the solver does 5 consecutive optimizations while adjusting the penalty for the non-linear constraints, the total run–time for about 100 000 function calls increases to almost one week even with all the above computational improvements.

5.2 Benchmark ORC

Even though the ORC shortcut model is well suited for a quick estimation or qualitative comparison, the proper evaluation of the MWM Cycle required a more detailed simulation of the benchmark ORC. As the ORC is a stationary cycle, several commercial tools are available. Most prominently there are ASPEN Plus® by Aspen Technology, a simulation tool that is widely used for process engineering of chemical plants, and EBSILON® Professional by Steag Energy Services with the focus on thermodynamics and turbine simulation that is suited for power plant simulations. The better fluid database within Aspen Plus (namely REFPROP) and the focus on the heat transfer effects instead of detailed turbine models made the former option the better choice.

The only two free variables in the ORC model are the pressure after the feed pump and the pressure after the turbine. While the former one was varied in a sensitivity analysis, the latter one was always set to the minimal possible values (which was limited by the temperature of the heat sink and the demanded pinch point). Preliminary simulations confirmed that a higher turbine outlet pressure would reduce the needed mass flow of the heat sink. While this had some effect on the auxilliary power when using ambient air as heat sink, it could be neglected in cases with cooling water. With regard to a thermodynamic optimum, the influence on the turbine power did always

[3] 200 individuals * 50 generations * 2 calls (non-linear constraint and fitness value)

[4] $\eta_{\text{caching}} \cdot 1/(60\,\text{cores})$

outweigh the savings in pump power of the cold water. The variation with ambient air as heat sink was not further analyzed in this work.

The Aspen model for an exemplary case with R134a at a 120 °C heat source is shown in fig. 5.8 on the following page. Aspen uses *streams* in order to store thermodynamic states and shows their properties like composition, temperature, pressure and flow rates. Components are represented by *(simulation) blocks*. They take the state of a connected input stream and alter it according to their type: heat exchangers transfer heat, pumps and turbines change the pressure level. Like for the detailed Matlab model, each simulation block can be set up with a set of output specifications (for example outlet temperature, transferred heat, heat transfer area, pressure change …) and offers different local solvers to compute the state change. The result of each block is then written to the connected output stream. For more complex dependencies, Aspen also offers global solvers that can vary single specifications of blocks and streams with a target condition that is not directly connected to them. Furthermore, a *sensitivity analysis* can be run, where Aspen varies one or more specifications in a loop and returns the converged cycle details of each run in a list.

Starting with the conditions after the condenser (COND), the pressure p_2 is derived from the specified turbine outlet pressure $p_4 = p_{\mathrm{exp}}$ (TURBINE) and the set pressure drop over the condenser $\Delta p_{\mathrm{WF}} = 0.2\,\mathrm{bar}$ (see section 6.1 on page 105 for a summary of all reference conditions). The outlet temperature of the condenser T_2 was set to be slightly subcooled by $\Delta T_{\mathrm{WF,cond}} = 2\,\mathrm{K}$ at the calculated pressure p_2. The pump then increased the pressure to the current level given by the sensitivity analysis $p_1 = p_{\mathrm{evap}}$ with the set isentropic efficiency $\eta_{\mathrm{is,fp}}$. The evaporator (VERD) is configured to provide a fully vaporized working fluid **3** at a defined superheat of $\Delta T_{\mathrm{WF,evap}} = 2\,\mathrm{K}$ and the simulation block sets the required heat transfer area accordingly. The stream **3** then enters the turbine where it is expanded to the already mentioned outlet pressure p_4. The power output is calculated from the enthalpy stream and the isentropic engine efficiency $\eta_{\mathrm{is,eng}}$. Afterwards, the expanded vapor is fed to the condenser where it is condensed and subcooled to the initial conditions. In order to meet the given pinch point constraint of the evaporator $\mathrm{PP}_{\mathrm{hot}}$, a global solver adjusts the mass flow of the working fluid matching the fixed heat source conditions **11**. The pressure drop of the heat source is compensated by an auxiliary pump (PUMPHOT). In the condenser, the another global solver

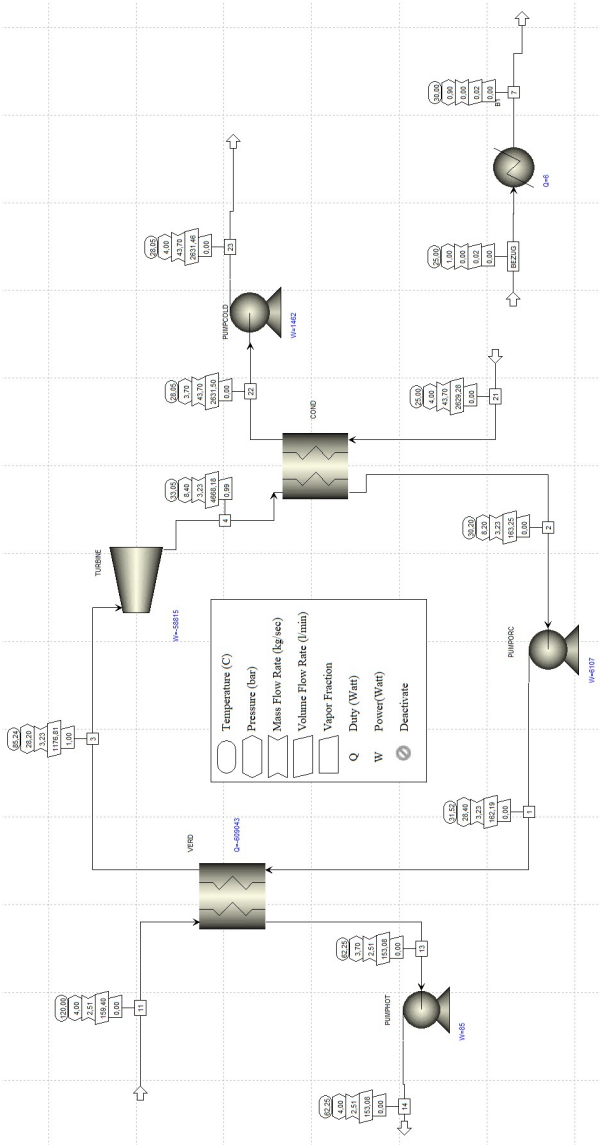

Figure 5.8: Aspen model of the Benchmark ORC.

adjusts the mass flow of the heat sink **21** to comply with the pinch point PP_{cold}. The pressure drop of the cold water is also made up for by another auxiliary pump (PUMPCOLD).

The resulting power output of the turbine and the need for the feed pump and the auxiliary pumps are used for the efficiency calculations. The available exergy from the heat source is calculated based on the reference conditions **BEZUG**. A recuperator (heat exchanger between turbine outlet and the stream before the preheater/evaporator) was not used as they, according to Bianchi and Pascale [13], only increase the internal efficiency, but the net power and hence the external efficiencies are not affected. The run of the sensitivity analysis returns the relation of evaporation pressure and efficiencies as for example shown in fig. 2.5 on page 20. In addition, the basic cycle properties (power output, pump power, heat exchanger area) are used within a MATLAB–script in order to calculate the economic numbers of all cases of the sensitivity analysis.

5.3 Model Assumptions

To provide a fair comparison between MWM Cycle and ORC, both are based on the same assumptions for the thermodynamic and economic calculations. Variable model values, like equipment efficiency or pinch points, are defined in section 6.1 on page 105. The fundamental assumptions on which the models themselves are based are summarized below.

5.3.1 Thermodynamic Model

The general thermodynamic model assumptions from the previous sections are summarized in table 5.1 on the following page.

Except for the fluid calculations and the wall model, the model assumptions for the cell–model and the Aspen model are in good agreement.

For the heat source, the thermodynamic conditions barely change and the error from using constant properties is small (also compared to the assessment of the shortcut model in appendix A.1.2). With the ORC being a stationary cycle, the inertia of the wall could easily be neglected and simply including its thermal resistance in the overall heat transfer coefficient k is justifiable.

Table 5.1: Assumptions for the heat exchanger models of the MWM Cycle.

Effect	NTU-Model	Cell-Model	ORC (Aspen)
Heat Source Fluid	incompressible, constant properties	incompressible, constant properties	REFPROP, liquid–only
Working Fluid	REFPROP, global state (batch)	REFPROP, global state (batch)	REFPROP, local state (flow)
Momentum Balances	neglected	neglected	neglected
Axial Heat Conduction	neglected	neglected	neglected
Pressure drop	neglected	friction and gravitation in energy balance	friction
Heat Transfer	pseudo stationary global estimation	local calculation with global coefficients	local calculation with global coefficients
HX Geometry	total area only	total area only	total area only
Wall	overall heat transfer only	1-D model (longitudinal)	overall heat transfer only

Table 5.2: Common dimensions for plate heat exchangers [77].

Dimension	Minimum	Maximum	Estimated Default
Length L (m)	0.4	5.0	1.0
Width W (m)	0.07	1.2	0.5
Plate Thickness s (mm)	0.5	1.2	1.0
Number of Plates N_P (-)	3	700	50
Wave Amplitude a (mm)	1.5	7.0	3.0
Wavelength Λ (mm)	1.5	7.0	5.0
Wave Angle φ (°)	10	80	45

Only the assumption of a homogeneous, global working fluid state in the MWM might result in some deviation. However, as discussed in section 5.1.1, the total error will be small due to rapid mixing. In contrast, the continuous stream through the ORC can easily—and should—be calculated with the local properties (temperature and heat transfer are dependent of the position).

The momentum balance and the axial heat conduction is neglected in all three models as their influence is estimated to be marginal.

The small influence of the pressure drop is completely neglected in the NTU–model. The pressure drop due to friction is implemented in both the cell-model and the ORC model. The effects of the gravity on the pressure are however only covered by the cell–model.

As basis for the applied total heat transfer coefficients k, the same local coefficients were used for all models. Established correlations were used on a common range of geometries from literature and significant average values were chosen (see table 5.2). The details of the correlations are given in appendix A.3 on page 198.

For a forced convective, single-phase flow in a plate heat exchanger, the correlations of Martin [75] provided a heat transfer coefficient in the range of $\alpha_{HS} \approx 8000\,\mathrm{W/(m^2{\cdot}K)}$. For flow pattern in a plate heat exchanger other than forced convection, no specific correlations are available. Instead, generic approaches for free convection and pool boiling of the working fluid were used. The pool boiling correlations from Rohsenow [78, 79] resulted in a boiling heat transfer of about $\alpha_{WF,boil} \approx 10\,000\,\mathrm{W/(m^2{\cdot}K)}$. When the temperature for

the onset of nucleate boiling is not reached [80], the correlation of Churchill and Chu [81] was used. The value of $\alpha_{\text{nat,liq}} \approx 1000\,\text{W/(m}^2\cdot\text{K)}$ was obtained for natural convection on a vertical plate in the liquid phase of both working fluid and heat source[5]. Using the fluid properties of the gaseous working fluid in the same equation, the heat transfer coefficient decreased to $\alpha_{\text{WF,vap}} \approx 150\,\text{W/(m}^2\cdot\text{K)}$. Average total heat transfer coefficients for condensation of $k_{\text{cond}} \approx 1500\,\text{W/(m}^2\cdot\text{K)}$ and cooling/subcooling of $k_{\text{cool}} \approx 750\,\text{W/(m}^2\cdot\text{K)}$ were estimated with the *Aspen Exchanger Design & Rating Tool* for the benchmark ORC. With the assumption of similar condensation requirements, the same values were used for the MWM Cycle.

All heat transfer coefficients were also validated against literature values from Shah and Sekulić [77] and further calculations by the commercial *Aspen Exchanger Design & Rating Tool*. With the above numbers, the total heat transfer for boiling in a PHE according to eq. (5.7)

$$k_{\text{PHE,boil}} = \frac{1}{\frac{1}{\alpha_{\text{HS}}} + \frac{s}{\lambda_{\text{wall}}} + \frac{1}{\alpha_{\text{WF,boil}}}} \approx 4000\,\frac{\text{W}}{\text{m}^2\cdot\text{K}} \tag{5.34}$$

lay well within the given general range of $3000\,\text{W/(m}^2\cdot\text{K)}$ to $7000\,\text{W/(m}^2\cdot\text{K)}$[77] for plate heat exchangers.

5.3.2 Economic Model

All the economic evaluations depend strongly on the initial investment K_0. The correlations of Turton [47] in section 2.2.3 use a regression to fit typical prices and depend on component–specific coefficients.

5.3.2.1 Cost Correlation Coefficients

Walter [82] collected the following numbers for the components of the Misselhorn Cycle and the ORC. As far as available, the numbers from Turton [47] were used. Some coefficients were also taken from Schlagermann [46] and Meinel, Wieland, and Spliethoff [83]. The missing information was covered by

[5] Free convective heat transfer on the heat source side takes place in phases without active circulation. See section 6.2.2 for the "unheated discharge phase".

Table 5.3: Coefficients for Module Costing Technique Basic Costs.

Component	Characteristic Dimension X	C_1	C_2	C_2
Piston Pump [47]	max. Power (kW)	3.3892	0.0526	0.1538
Heat Exchanger[6]	Area m^2	1.7540	0.8619	0.0288
Pressure Vessel [46]	Volume m^3	3.4974	0.4485	0.1074
Motor Genset[6]	max. Power (kW)	3.6894	1.4800×10^{-8}	0.1734
Turbine Genset [83]	max. Power (kW)	2.6259	1.4398	−0.1778
Power Connection [46]	max. Power (kW)		$K_k^0 = 80 \cdot X$	

[6] customized correlations

customized correlations (see appendix B on page 203). The costs from Turton [47] in $ are based on the period of May to September 2001 with a CEPCI of 397 [82]. The other correlations were set around 2015 in € with a CEPCI of 576 [84].

The needed coefficients for eq. (2.35) (basic component costs K_k^0) are listed in table 5.3. The cost estimations are based on one characteristic dimension for each component. The required "size" of each component is taken from the corresponding maximal value in the simulation. In order to cover the expected differences between the solely thermodynamic simulations and the requirements of a non-ideal, practical setup, the dimensions were increased by specific surcharge factors as proposed by Schlagermann [46]. The installed pump power is increased by a factor of 1.15 compared to the maximal occurring value from the simulation (see table 5.4 on the following page). The engine and turbine power is scaled by 120 %. The condenser is also increased to 120 % in order to provide a hold-up for the working fluid. Finally, all maximal pressure levels (feed pump, pressure vessel, evaporator and condenser) are scaled with a safety factor of 1.2.

The basis for these cost correlations is generally carbon steel and a calculation pressure of 1 bar. The up-scaling to the operation pressure and stainless steel is then handled by the pressure factor F_p and the material factor F_M (see table 5.5 for coefficients of eq. (2.36)). However, the specific correlations that

Table 5.4: Surcharge factors to cover non-ideal behavior of a real setup.

Value	Surcharge Factor
Pump Power	1.15
Engine Power	1.2
Condenser Area	1.2
Pressure Level	1.2

Table 5.5: Coefficients for Pressure and Material Correction Factors from Turton [47].

Component	$C_{p,1}$	$C_{p,2}$	$C_{p,3}$	F_M
Piston Pump	−0.245 382	0.259 016	−0.013 63	2.19
Pressure Vessel	Pressure Correction from eq. (2.37)			1.8

were developed for the custom components (heat exchangers, motor generator set, turbine generator set) already included pressure and material additions and do not need these correction factors. Besides, the coefficients for the pressure vessel are valid for a reference pressure of 15 bar.

The pressure correction factor for pressure vessels is not directly based on the pressure level, but on their wall thickness. With the use of a spherical shape in the MWM Cycle, the needed gas volume leads to the inner diameter d_i. In order to withstand the maximal pressure, the standards from *AD 2000 Regelwerk* [85] give the equation

$$s_{wall} = \frac{p \cdot d_i}{40 \cdot K/S - p} + (c_1 + c_2) \cdot \frac{40 \cdot K/S + p}{40 \cdot K/S - p} \tag{5.35}$$

for the wall thickness. The strength parameter K, the safety factor S and the two additional factors c_1 and c_2 were also taken from [85] for stainless steel as shown in table 5.6. The wall thickness is then used in eq. (2.37) to select the correlation for the calculation of the pressure correction factor.

The additional indirect costs of all components are covered by the bare module factor in eq. (2.38) which is calculated from the coefficients in table 5.7.

Table 5.6: Used Coefficients for Pressure Vessel Design from *AD 2000 Regelwerk* [85].

K	S	c_1	c_2
180	1.5	1 mm	1 mm

Table 5.7: Bare Module Coefficients from Turton [47].

Component	B_1	B_2
Piston Pump	1.89	1.35
Heat Exchanger	0.96	1.21
Pressure Vessel	2.25	1.82
Motor-Generator Set	0	1.45
Turbine-Generator Set	0	1.45
Power Connection	-	-

Finally, the costs for operation and maintenance in eqs. (2.30) and (2.31) are estimated with the coefficients in table 5.8.

5.3.2.2 Assessment of Cost Correlations

Cost estimations are always subject to a significant uncertainty. Bejan, Tsatsaronis, and Moran [48] predict a discrepancy of about ±30 % for cost estimations. Others like Spang and Roetzel [86] completely disapprove of cost estimations and recommend to only use actual offers.

For the widely used components, like the piston feed pump, the use of a literature correlation seemed justified. In contrast, no correlations at all were available for the "special" components like batch evaporator and vapor engine that are needed for the dynamic behavior of the MWM Cycle. Thus, custom correlations were set-up, which were based on actual price information in connection with the pilot plant at the Maschinenwerk Misselhorn MWM GmbH.

The biggest uncertainty might well be the costs for the pressure vessels. Even though there is extensive data for vessel prices per se, they seem to be

Table 5.8: Coefficients for Costs of Operation and Maintenance from Verein Deutscher Ingenieure [45].

Component	f_{repair} (%)	$f_{\text{s\&i}}$ (%)	Annual Operational Effort (h/a)
Piston Pump	2	1	0
Heat Exchanger	2	0	0
Pressure Vessel	2	1	0
Motor-Generator Set	6	2	100
Turbine-Generator Set	6	2	100
Power Connection	1	0	0
Instrumentation	1.5	1.5	0

very high for a simple and small "pressure storage" as needed in the MWM Cycle compared to the other components. Especially when adding the bare module factors, these correlations typically cover a process vessel with major connections, instrumentation and accessibility. However, hardly any alternative data was found for the rather simple requirements of a small and simple spherical tank. Many references do not even cover these small scales. The data for small tanks by Garrett [87] ends at 400 L, but there it lies well within the same order of magnitude as the correlation used in this work (which goes down to 100 L). Only Gebhardt, Kohl, and Steinrötter [88] have collected some actual prices for small scale tanks for pressurized hot water in the context of heating, ventilating and air-conditioning systems. Their correlation is valid down to 150 L. However, this regression again gives about the same numbers for small scale tanks[7] which justifies the use of the correlation of Schlagermann [46]. As will be further discussed in section 6.4, the price for all vessels ($\approx$ 100 000 € for 5 times 80 L at 40 bar in an exemplary scenario) therefore has a major impact on the economic optimization when compared to the costs of the same number of used evaporators ($\approx$ 1000 €) or the one feed pump ($\approx$ 10 000 €).

[7] For a cross–comparison of all three correlations, a volume of 400 L gives in 2018 for only one raw tank, stainless steel and 15 bar: Schlagermann [46] $\approx$ 3800 €, Garrett [87] $\approx$ 5800 €, Gebhardt, Kohl, and Steinrötter [88] $\approx$ 3000 €

Chapter 6

Results and Discussion

This chapter gives the results and evaluation of the MWM Cycle simulations. Section 6.1 lists the project specific, adjustable reference conditions like component properties, current interest rates and exchange rates. Section 6.2 contains the result of the thermodynamic optimizations and compares the NTU–approach to the detailed model. Both are also rated against the ORC. Section 6.3 extends the initial thermodynamic comparison to different working fluids. The last Section, 6.4, adds the results of the economic optimization. First, these economic results are compared to their thermodynamic counterparts. Second, the economic potential of the MWM Cycle is rated against the benchmark ORC and against literature values.

6.1 Project Specific Reference Conditions

In addition to the general assumptions listed in section 5.3, the final project–specific reference condition for the thermodynamic and the economic rating are given in this section

6.1.1 Plant–Specific Properties

Fluids To compare and rate the different cycles and implementations, three different reference scenarios were defined (see table 6.1 on the next page). Hot water at $T = 100\,°C$, $120\,°C$ and $140\,°C$ and 4 bar was used as heat source. These temperatures could be delivered by either a geothermal source or from industrial waste heat. Cooling water at $T_0 = 25\,°C$ and 4 bar provided the heat sink and also defined the reference temperature for the exergy calculations. In

Table 6.1: Reference Conditions of Heat Source and Heat Sink.

		Heat Source (water)		Heat Sink (water)
Temperature, T	100 °C	120 °C	140 °C	25 °C
Mass flow, $\dot{m}$	3.18 kg/s	2.51 kg/s	2.06 kg/s	variable
Pressure, p	4 bar	4 bar	4 bar	4 bar
Available Heat, $\dot{Q}_{av}$	1 MW	1 MW	1 MW	-
Available Exergy, Ex_{av}	109 kW	133 kW	155 kW	-

Table 6.2: Reference Conditions of the Cycle Components.

Component Property		Value
Pinch Point Condenser	PP_{cold}	5 K
Pinch Point Evaporator[1]	PP_{hot}	5 K
pressure drop working fluid (evaporator[1] & condenser)	Δp_{WF}	0.2 bar
pressure drop water (evaporator & condenser)	Δp_{HS}	0.3 bar
isentropic pump efficiency	$\eta_{is,pump}$	90 %
isentropic engine efficiency	$\eta_{is,exp}$	80 %

[1] ORC only

order to create three easily comparable cases with regard to overall efficiencies, the mass flow of the heat source was chosen as to always provide an available heat of $\dot{Q}_{av} = 1\,MW$. The available exergy for the three cases is also given in table 6.1. Reference for this setting was the enthalpy flow and exergy flow at the dead state $T_0 = 25\,°C$ and $p_0 = 1\,bar$.

Components The component specific properties are listed in table 6.2. As specified in detail in appendix A.2.2 on page 195, the needed temperature levels in the condenser are all dependent of the desired turbine outlet pressure: adding the required pinch point $PP_{cold} = 5\,K$ and the desired sub-cooling of the working fluid $\Delta T_{WF,cond} = 2\,K$ to the heat sink inlet leads to the minimal possible saturation temperature of the working fluid at the end of the

condenser. The corresponding saturation pressure can be calculated from Refprop. Adding the pressure drop of the working fluid Δp_{WF} over the condenser gives the minimal possible turbine outlet pressure p_{exp}. This minimal process pressure of the working fluid was always calculated in advance and set as turbine outlet pressure for each simulation. The mass flow of the cooling water was then individually adjusted to comply with the required pinch point $PP_{cold} = 5\,K$ against the turbine outlet stream at the condenser inlet (see again appendix A.2.2 for details and figures). The pressure drop of the water, heat source in the evaporator, and heat sink in the condenser, is set to $\Delta p_{HS} = 0.3\,bar$. The definition of a pinch point $PP_{hot} = 5\,K$ and a working fluid pressure drop in the evaporator $\Delta p_{WF} = 0.2\,bar$ is only necessary for the ORC. All pumps are assumed to work with an isentropic efficiency of $\eta_{is,pump} = 90\,\%$. The expander efficiency for both ORC turbine and modified diesel engine are set to $\eta_{is,exp} = 80\,\%$. Even though Fischer [11], Yari et al. [22], and Steffen, Löffler, and Schaber [40] all use an isentropic turbine efficiency of $\eta_{turb} = 85\,\%$, Steffen, Löffler, and Schaber [40] themselves state that these numbers are quite high for small scale turbines. While detailed experimental data for the engine to be used in the MWM Cycle is not available yet, higher numbers than for the two–phase expanders are expected to be possible and the same 80 % as for the turbine were chosen.

Free Variables Table 6.3 on the next page summarizes the free variables as they have been introduced in section 4.2.2 and, when using the detailed evaporator approach, in section 5.1.1.2. This results in all the variable inputs that were optimized, their lower and upper boundaries and some typical default values.

The former group in the table includes the (once selected) fixed properties of the evaporators, whereas the latter group consists of the properties that could be used to adjust the operating point. The lower bound for the switch pressure is the minimal process pressure from the previous paragraph. Its upper counterpart p_{max} is the smaller value of the critical temperature of the working fluid and the saturation pressure of the working fluid at heat source temperature.

Table 6.3: Lower and Upper Boundaries for the Independent Variables of the MWM Cycle.

Independent Variable		Min.	Max.	Default
Heat transfer per HX	kA_{all} (kW/K)	10	40	30
Free volume	$V_{\text{HX},0}$ (m^3)	0.01	0.8	0.1
Plate Thickness	s (mm)	0.5	1.2	1.0
Wave Amplitude	a (mm)	1.5	7.0	3.0
Mass flow	$\dot{m}_{\text{WF,fill}}$ (kg/s)	2	20	20
Maximum mass	$m_{\text{WF,fill}}$ (kg)	10	40	40
Switch pressure limit	$p_{\text{WF,switch}}$ (bar)	p_{exp}	p_{max}	$\frac{p_{\text{exp}}+p_{\text{max}}}{2}$
Discharge volume flow	$\dot{V}_{\text{WF,dis}}$ (m^3/s)	0.0125	0.625	0.1

Cell Size With the above defined mass flow of the heat source and the range for the heat exchanger geometry (table 5.2), the cell size of the model could be set and the stability conditions of the solver were checked. From a mathematical point of view, the stability of the differencing schemes is simply dependent on the step sizes Δz and Δt.

For the explicit upwind scheme in eq. (5.30) on page 85, the stability is guaranteed when the Courant Condition is met [64]:

$$\frac{\mathrm{v}\Delta t}{\Delta z} \leq 1. \tag{6.1}$$

In physical terms this is equivalent to a time–step Δt which is smaller than the time the wave propagation takes to cross one cell $t = \Delta z/\mathrm{v}$. Otherwise the propagated information could "skip" single cells and a computational oscillation would occur. Adapted to the reduced geometry information, this condition can be rewritten as

$$\frac{\Delta t}{\tau \cdot z_{\text{frac}}} \leq 1. \tag{6.2}$$

The stability condition for the FTCS-scheme of the wall is given by Press

[64] as

$$\frac{2D\Delta t}{(\Delta z)^2} \leq 1. \tag{6.3}$$

Again, this means that the time–step has to be smaller than the duration a physical phenomenon, here the heat conduction, takes to cross one cell $t = (\Delta z)^2/2D$.

The default geometry from table 5.2 led to a dwell time of the heat source of about $\tau = 10$ s. Following the approach of an emphasized energy conservation and an acceptable computation time over an excessively detailed modeling of transport phenomenons, a rather coarse grid with a cell size of $z_{\text{frac}} = 0.1$ along the length of the plate was chosen. This allowed for a time step of $\Delta t = 0.1$ s while still having some distance to the Courant Condition from eq. (6.1). Using the same cell size for the wall, also the second stability condition was fulfilled. Both conditions were smaller than required by a magnitude of 10^{-1} and 10^{-4}, respectively, which gave enough safety margin for the variations during the optimization.

6.1.2 Current Economic Numbers

Price Changes and Interest Rates All economic evaluations and optimizations were run for the year 2018. Therefore, the used price index for all components was set to CECPI (2018) = 603.1[84]. Based on the assumptions of Walter [82], the global interest rate was estimated with $i = 4\,\%$ which gives $q = 1.04$. With the still ongoing low-interest period, those values are in good agreement with the past values of 6.5 % in 2015 [18] and 9 % in 2011 [46]. The previously shown exchange rate of 1 € = \$1.11 in 2015[89] was also still valid for 2018/2019 [90].

The long-term estimations for the price change factors of Walter [82] are also used in this model. The assessment of the price indices for electricity, commercial products and consumer prices from the Federal Statistical Office in Germany delivered the price change factors in table 6.4. The forecast of price change factors is always subject to major uncertainties and different studies might suggest differing numbers. However, with all cases of ORC and MWM being rated on the same reference condition, the economic model quality is sufficient for the general rating and a fair comparison. As a general

Table 6.4: Price Change Factors r.

Scope	Value
General Investment	1.015
Operational Costs	1.015
Electricity	1.04

trend, the total profitability of the cycles would benefit from increasing price change factors for electricity and the increasing revenues. In contrast, rising price change factors for general investments and operational costs as well as increasing expenses due to rising exchange rates would reduce the economic efficiency. A further sensitivity analysis of the economic performance to the different forecast scenarios was well beyond the scope of this work, but could be interesting for further analysis.

Operating Hours and Service Life Time As operational experience for the MWM Cycle is still missing, its operating hours for the first plants were estimated with only 5000 h/a in correspondence with the Maschinenwerk Misselhorn MWM GmbH [91]. This reduction covers, among other things, unexpected failure and unsatisfying efficiencies of components. The well–established ORC was in contrast estimated with 7000 h/a. Most of the single components were still estimated to show a medium to long service life. Table 6.5 lists the values as given by Verein Deutscher Ingenieure [45]. Only for the customized motor-generator set, the basic literature value of a CHP plant was taken and further reduced by 30 %. The service life of the ORC turbine was taken from the AfA-tables of Bundesministerium der Finanzen [92].

Proceeds At last, one of the most important drivers for economy are the proceeds of an investment. The simulation model gives a certain amount of produced electricity, but there are different approaches for the monetization. Simplified for the overall evaluation of the MWM Cycle there are three major options.

The obvious one would be to feed the electricity to the grid and sell it. However, besides the limitation that small units cannot directly take part

Table 6.5: Service Life of Components.

Component	Service life (in a)
Piston Pump	18
Heat Exchanger	20
Pressure Vessel	25
Motor-Generator Set[2]	10
Turbine-Generator Set[3]	22
Power Connection	10
Instrumentation	15

[2] CHP reduced by 30 %
[3] AfA-tables of Bundesministerium der Finanzen [92]

in the exchange market and rather have to rely on their network operator or another third party, the achievable rates are comparably low. For 2018, the average electricity rate for intraday auctions that defines the maximal buy-back price for commercial units was only about 0.045 €/kWh [93]. And some additional fee would further be withheld by the retailer.

Once a renewable energy source is involved, the far more lucrative rates provided in context of the Renewable Energy Sources Act (German: "EEG" [94]) may become applicable. If the energy comes from a geothermal source, the guaranteed refund for the year of these simulations is 0.252 €/kWh. This price is valid for the first 20 years of a geothermal power plant. After 2020, the fixed guaranteed 20-year-rate is reduced by 5 % per year, depending on the year of commissioning and first commercial operation of a site. [94, §45]. However, using these numbers for geothermal energy in an economic evaluation requires to also consider the enormous upfront investment costs for exploration and drilling.

Somewhere in-between in terms of profitability lies the direct self–consumption of the generated electricity. Given an existing need for auxiliary power, the electricity from industrial waste heat could for example be integrated into the process and could directly be used in place. Without any actual refund, the revenue of this would come from the savings in the purchased electricity. The average electricity rate for commercial sites in 2018 was 0.1796 €/kWh

[95] in Germany. The contribution to the advancement of renewable energies ("EEG-Umlage") has still to be partly paid for electricity that is directly used on-site once it exceeds 10 kW. Therefore, the savings have to be reduced by 40 percent of the rate for 2018 (40 percent of 0.0679 €/kWh [96]) as well as another 0.0205 €/kWh of electricity taxes. The remaining savings used in the evaluation are 0.1319 €/kWh.

As discussed in section 2.2.2, a long term investment like a power plant is best evaluated by a dynamic method (internal rate of return, annuity method …). In order to conduct such a dynamic evaluation, price change factors and, most importantly, a reasonable estimation of the revenues is required. The first choice for the MWM evaluation would be the annuity method with the estimated profit from self-consumption of the generated electricity. However, most of the recent work on ORCs and advanced cycles measures the economic performance with regard to the promising rates for the funded geothermal power. They either use the guaranteed rate of 0.25 €/kWh [19, 46] or skip the dynamic approach completely and only rely on the specific investment cost (SIC) as a static method to rate the initial specific investment. While most of the authors using the SIC only consider the ORC module [18, 24, 97] and neglect the major drilling costs, Quoilin et al. [6] give a literature overview of both the module SIC and the total SIC for geothermal use and waste heat recovery. Moreover, the cited sources for geothermal power plants are based on an available heat source energy in the range of 10 MW to 30 MW [6, 18, 19, 46] rather than the 1 MW of the present MWM reference case. Compared to these dimensions, the estimated costs for drilling and exploration from about 6 MM € (for the 10 MW reservoir) [46] up to 16.5 MM € [18] and 20 MM € [19] can hardly be compensated by the introduced scale of the MWM Cycle.

In order to still benefit from this pool of information and comparison values, also the MWM Cycle and ORC in this work will initially be evaluated with the rate of 0.25 €/kWh. The comparison with the literature values in section 6.4 will still be limited to the static SIC method of these two groups:

- SIC of the large scale power cycles, but without exploration / drilling costs (Quoilin et al. [6], Heberle and Brüggemann [18], Preißinger, Heberle, and Brüggemann [19], and Meinel, Wieland, and Spliethoff [97]),

- SIC of the small scale waste heat recovery power cycles, without exploration / drilling costs (Quoilin et al. [6, 24]),

Only the comparison between the small scale benchmark ORC and the MWM cycle, both based on the models in this work, will be based on the dynamic methods. A short assessment of the effects on the MWM economy by the three approaches for the revenues (selling, funded rates, self–consumption) will also be given later on.

6.2 Optimized System Efficiency

A qualitative, figurative example of the MWM Process was already given in context of the introduction of the cycle concept in chapter 4. The following two sections will provide a detailed analysis of the different effects that take place in the MWM Cycle in context of an optimization for maximized system efficiency.

6.2.1 Thermodynamic Results of the NTU-model

The reference case for the following discussion will be the 100 °C–heat-source–case from table 6.1 on page 106 with R134a as working fluid and six heat exchangers.

6.2.1.1 General Behavior and Performance

Figure 6.1a shows the corresponding T-Q-diagram as already known from fig. 4.5 on page 60. The process has to be read from right to left: the filling phase starts at 70 %, followed by evaporation 1 to 4 and at last followed by the discharge phase. The yellow area marks the exergy destruction and the orange area marks the unused and lost exergy. Figure 6.1b shows the corresponding temporal progression of the state in the evaporator (time progression from left to right). The cycle starts at 0 s, the area left to this shows the end of the previous cycle pass.

It can be seen in fig. 6.1b that during the first seconds of the filling phase, the global vapor quality drops rapidly due to the filling with liquid working fluid. Once the final working fluid mass of about 50 kg is reached, the heating of

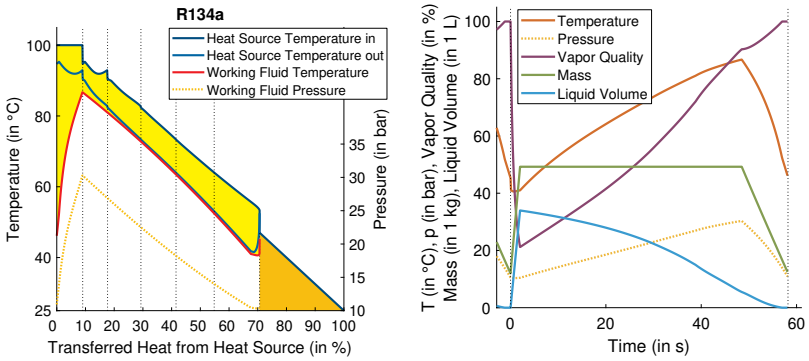

(a) Temperature-Heat-Diagram

(b) Variation of the state in one evaporator

Figure 6.1: Simulation results of the 100 °C–default–case with six heat exchangers (NTU-Model).

the enclosed working fluid causes a continuously rising pressure and boiling temperature, matching the progress in the T-Q-diagram (identical data is plotted for temperature (red), and pressure (yellow) in both figures). The ongoing isochoric evaporation also causes an increasing vapor fraction and a decreasing liquid volume. With the onset of the discharge phase at about 50 s, the mass starts to drop again. The remaining liquid working fluids still evaporates, but cannot compensate for the discharged mass flow. The pressure and boiling temperature are therefore also dropping again. The vapor fraction, however, further rises due to the re-evaporation of the working fluid. At the end of the cycle, about 15 kg of working fluid at a vapor fraction of almost 100 % remain in the evaporation which are then mixed with the liquid in the next filling phase. The corresponding liquid volume of the working fluid at this time is close to zero. The end of this cycle gives the initial state for the next cycle pass.

Figure 6.1b also shows that the period of actual filling is much shorter than the total filling phase (for six heat exchangers each cycle phase here is about 10 s long). With the two input variables “working fluid mass flow” and “maximum added working fluid mass”, the optimization algorithm could

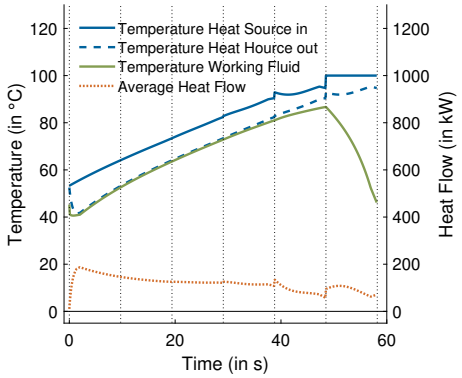

Figure 6.2: Temperature levels and heat flow of the 100 °C–default–case with six heat exchangers (NTU-Model).

adjust the filling time independently of the cycle timing. For all cases of thermodynamic optimization, the final results showed more or less the same behavior: A very high mass close to the upper boundary was filled in with a high filling mass flow (but not as high as the boundary). For the evaporators, this results in nearly constant temperature and pressure levels during the filling phase. Their values match the lower pressure limit within the evaporators at the end of the discharge phase. For a slower filling, using the whole filling phase, the feed pump would have to work against the ongoing evaporation and increasing pressure. An even faster filling is obviously not necessary and would furthermore spend the already available pressure for the next cycle pass. With regard to the practical implementation, this effect could also be observed with the pilot plant of Maschinenwerk Misselhorn MWM GmbH. A first adaption was to feed the working fluid to a prebuffer and to load it into the evaporators at the start of the filling phase at once.

Having a look at the heat flow and temperature levels in fig. 6.2 gives some further insight, especially at the transition from one discharge phase to the next filling phase. Like in fig. 6.1b, the temporal progress in this figure has to be read from left to right. It can be seen that, while the four evaporation phases show a constant and smooth heat flow, the very first and last seconds of the cycle only have a minor heat flow. The discharge phase to the right furthermore

shows the constant inlet temperature of the fresh heat source whereas the working fluid is cooling down. The decreasing heat flow in opposition to the rising temperature difference can be explained by the dropping liquid volume. The NTU-model (section 5.1.1.1) uses the moving liquid level in order to distinguish between the fast pool–boiling heat transfer and the poor vapor–phase heat transfer. With an almost completely evaporated working fluid at the end, even the higher temperature difference cannot produce any relevant heat transfer. Only when the liquid level rises again, the heat flow rapidly increases during the next filling phase. In addition, fig. 6.2 visualizes the lack of any heat capacity of the wall material and residence time of the heat source medium in the NTU-model. With the start of the filling phase, the heat source properties, inlet and outlet temperature, immediately drop to the new values without any thermal inertia.

6.2.1.2 Comparison to a Common ORC

The thermodynamic optimization of the above given reference case results in a net power output of 49.9 kW for the MWM Cycle. Based on the available exergy of 109 kW, this equals to a second law efficiency of $\eta_{II} = 45.8\,\%$. The benchmark ORC with the same reference conditions and R134a as working fluid (which is also the highest rating working fluid for this temperature, see section 6.3) yields only 33.7 kW ($\eta_{II} = 30.9\,\%$). This gives the MWM Cycle a thermodynamic advantage over a common ORC of 48 % at 100 °C. In detail, the MWM Cycle excels by transferring more heat and exergy from the heat source ($\eta_{II,ext}$: MWM 90 % vs. ORC 75 %) and simultaneously providing a better conversion efficiency ($\eta_{II,int}$: MWM 51 % vs. ORC 41 %). Of course the operating point of the ORC could be shifted to improve one of the two former efficiencies. However, the parameters are already optimized for a maximal system efficiency.

While the power consumption of the feed pump is reduced for the MWM Cycle due to the low filling pressure (P_{feed}: MWM 0.8 kW vs. ORC 3.1 kW), the total power consumption is almost equalized by the auxiliary pump power for the pressure loss in the six heat exchangers (P_{aux}: MWM 2.4 kW vs. ORC 0.9 kW).

Regarding the six heat exchangers of the MWM Cycle, the total heat transfer area exceeds that of the ORC by a factor of about 4.4 (A_{total}: MWM 58.1 m^2

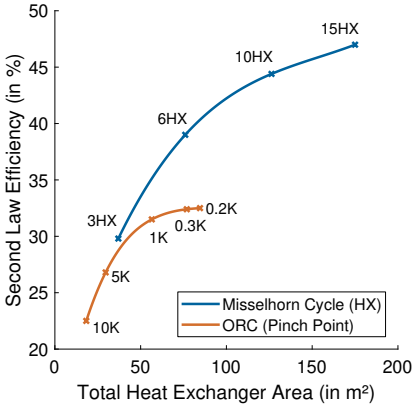

Figure 6.3: Comparison of the second law efficiency of MWM and ORC depending on the total heat transfer area for a heat source at 85 °C as shown by Gleinser and Wieland [98].

vs. ORC 13.1 m^2). A comparison at slightly different reference conditions by Gleinser and Wieland [98] (heat source flow 7 kg/s at 85 °C) shows that simply increasing the heat exchanger area for the ORC would not lead to the same performance (see fig. 6.3). Even though the pinch point could be decreased by this measure, it would still limit the overall efficiency. In contrast, adding more heat exchangers to the MWM Cycle still significantly improves its performance. As a result, the optimization algorithm always ended up at the upper bound when the number of evaporators was included in the thermodynamic optimization. As long as there were no limiting costs included in the optimization, the number of evaporators was therefore always set to a decent number of six for all the following cases. A comparable optimized case with the present reference conditions and only three evaporators would give a net power output of 41.1 kW, which is still 22 % better than the benchmark ORC ($\eta_{II,int}$: MWM 37.7 % vs. ORC 30.9 %). The economic rating of the number of heat exchangers will follow in section 6.4.

The results of these reference cases are summarized together with those of the following basic optimization cases in table 6.6 on page 123.

6.2.2 Influence of Thermal Inertia

Covering the weaknesses of the NTU-model, the detailed model adds thermal inertia of wall material and heat source medium to the simulation.

6.2.2.1 Thermodynamic Results of the Detailed Model

Running with the same reference conditions as the already presented NTU-case, the results from the detailed model can be seen in fig. 6.4 on the next page. In direct comparison between the heat–flow–figures for the NTU–case (fig. 6.2 on page 115) and the detailed model (fig. 6.4a), a few differences of the plot layout become apparent. In addition to the temperature and pressure levels of the fluids, the average temperature of the wall material was added to the plot. Also, the heat flow is now separated for the amount flowing from the heat source to the wall and the one going from the wall to the working fluid.

These additional plot–lines visualize two new effects during the discharge phase and at the transition to the next filling phase. The working fluid temperature is still dropping during the discharge (70 s to 85 s), following the boiling pressure of the system. In contrast, the wall almost keeps the temperature of the heat source. Even though the temperature difference at the working fluid gets gradually larger, the poor heat transfer to the working fluid vapor and the good heat transfer on the heat source side keep the heat flow on both sides of the wall balanced and therefore keep the wall temperature high.

With the start of the following filling phase (0 s to 15 s), the fresh cold working fluid is fed to the hot–walled evaporator which is also still filled with hot heat source medium. Therefore, an enormous heat flow to the working fluid balances these temperature levels during the first few seconds (peaking heat flow shown by orange line) and causes thermal stress to the wall material. In addition, even the now applied, colder heat source medium (last phase of heat source cascade) is slightly heated by the wall (negative heat flow shown by purple line). Figure 6.6 on page 120 shows the temperature profiles within one evaporator shortly after the start of the filling. In the lower part, where the wall is already in contact with the liquid working fluid, the heat is rapidly transferred to the cold working fluid by means of a boiling heat transfer and the wall is cooled down. The heat source, entering the evaporator from the bottom, at some point also reaches a height where the wall is still hot and heat

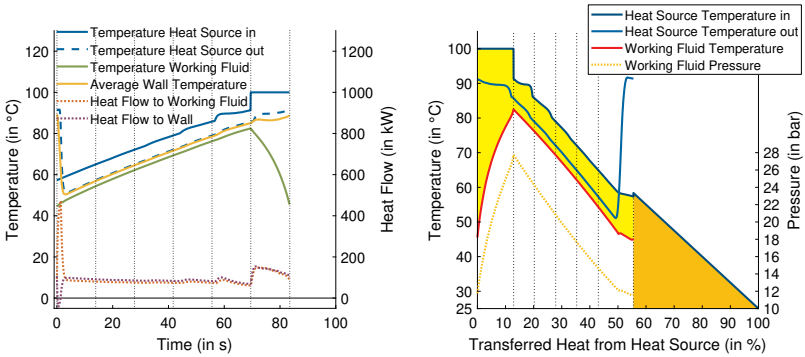

(a) Temperature levels and heat flow

(b) Temperature-Heat-Diagram

Figure 6.4: Simulation results of the detailed model at 100 °C with six heat exchangers.

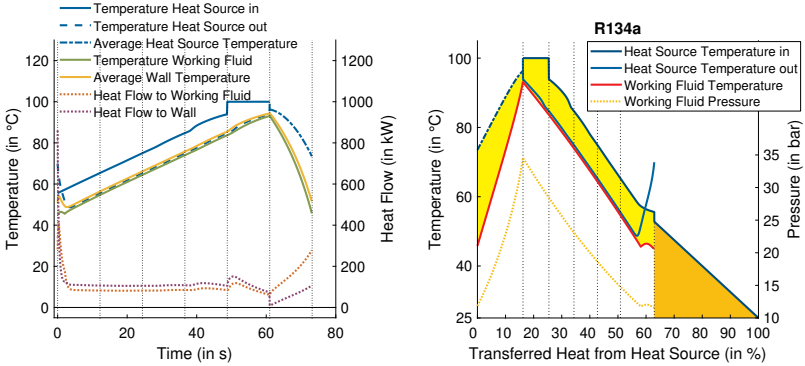

(a) Temperature levels and heat flow

(b) Temperature-Heat-Diagram

Figure 6.5: Simulation results of the detailed model at 100 °C with six heat exchangers and unheated discharge.

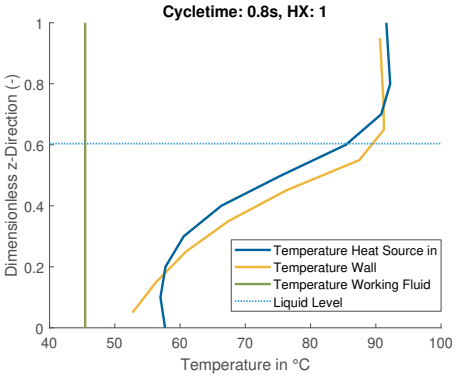

Figure 6.6: Temperature profiles within one evaporator shortly after the start of the filling phase.

is transferred from wall to heat source. The top of the evaporator, however, is not affected during these first seconds. The heat source leaving the heat exchanger is therefore still hot due to its residence time. As the evaporator in the filling phase is the last one in the heat source cascade, the unused exergy of this fraction of the heat source will be completely lost. The resulting high excess temperature and the increased lost exergy can also be seen in fig. 6.4b at around 55 %.

In the attempt to compensate the included inertia of the system, the optimization resulted in a slower timing of the whole cycle. With a cycle duration of 83 s instead of 58 s, there is more time for the heat transfer and the leveling of the temperatures. However, while the total amount of net energy per cycle is about the same for both models (about 3 MJ, see table 6.6 on page 123), the longer duration of the detailed model results in a reduced net power of only 37.2 kW ($\eta_{II} = 34.1\,\%$). Even though this is still better than the benchmark ORC ($\eta_{II} = 30.09\,\%$), the predicted advantage of the MWM is now significantly reduced.

6.2.2.2 Unheated Discharge

To overcome the influence of the thermal inertia, the system behavior was adjusted by an unheated discharge phase. The discharge phase was excluded from the heat source cascade and only the filling and evaporation phases were actively heated. Once an evaporator reached the last phase, the prior heat source medium simply remained enclosed inside. Its average temperature is visualized in fig. 6.5a on page 119 by the blue dash–dotted line. Without the forced flow, the heat transfer then merges to a moderate natural convection. The corresponding heat flow to the wall therefore immediately drops at this point (purple line at around 60 s) and only rises once the temperature difference grows.

With the lack of the further active heating, both the wall and the enclosed heat source medium now also cool down and follow the temperature trend of the working fluid during discharge. When the fresh working fluid is then fed to the evaporator in the next filing phase, the temperature differences between feed flow, wall and heat source are much smaller than for the previous setup. The initial peak of the boiling heat transfer and the thermal stress would be reduced, but instead an initial peak in the heat flow from heat source to the cold wall occurs now.

Still, the unheated discharge phases increases the cycle performance by three means. First, the colder heat source outlet at the end of the cascade (during filling phase) reduces the exergy losses (see exergy losses in fig. 6.5b on page 119). Second, the hottest heat source is not wasted to the large temperature difference during the discharge phase anymore and the exergy destruction is reduced (see exergy destruction in the left region in fig. 6.5b). Last, the maximal process temperature and pressure at the end of the evaporation could be further increased by applying the hottest heat source in this phase instead. Increasing the maximal temperature by 10 K to 92.5 °C, the peak pressure rises from 27.8 bar to 34.2 bar. Gaining some boost from these three measures, the optimization ended up at a faster cycle timing again. While the total energy output per cycle is again in the same range range (3.4 MJ), the shorter cycle duration of 73 s resulted in a net power output of 46.8 kW (η_{II} = 42.9 %). Especially the reduced exergy destruction and the higher process pressure support an increased internal efficiency (see table 6.6). The advantage over the benchmark ORC is hereby at a competitive +39 % again.

The idea of further leveling the temperatures by an additional unheated filling phase did not prove advantageous. By not feeding hot heat source medium to the filling phase, the wall temperature indeed further approached the working fluid temperature. The thermal gradients were minimized by the moderate heat transfer rates of the natural convective flow and also the residual exergy from the enclosed heat source was almost completely used. At the same time, the vanishing heat flow reduced the thermodynamic cycle efficiency, as most of the filling phase did not contribute to the total heat transfer. The faster cycle time of 72.5 s could not compensate the slightly reduced amount of transferred energy (3.3 MJ). This setup therefore resulted in a slightly lower net power output of only 46.1 kW ($\eta_{II} = 42.3\,\%$, see table 6.6).

6.2.2.3 Assessment of the Optimization Results

The major reason for the longer cycle duration with the inertia–models can be explained with a closer look at the optimization results. During the filling phase, most of the stored heat is lost either in form of unused hot water or as heat transfer from the wall to the colder heat source. In order to minimize those losses, the optimization ended up reducing the heat capacity of the heat exchangers. Thinner walls reduce the mass of the wall material, thinner wall gaps reduce the mass of the enclosed heat source medium (see table 6.6, bottom part). When the lower boundaries for those two variables were reached, the final measure was a reduced heat transfer area. On one hand this further reduced the thermal masses, but on the other hand the heat transfer was also limited. Evaporating one batch of liquid working fluid (roughly about 50 kg for all cases) always takes about the same amount of energy. However, with the reduced heat transfer, the cycle duration had to be longer and the power output was reduced. The optimization thus had to find a compromise between a small heat capacity and a sufficient heat transfer area.

By introducing the unheated discharge, most of the stored energy could be transferred during the discharge phase. With less losses caused by thermal inertia, the optimized evaporators became bigger again, the increased heat transfer allowed for a faster cycle timing and the advantageous power output was restored.

In addition, the trend for less inertia shifts the whole cycle closer to the

Table 6.6: Cycle performance for the different simulation approaches with a heat source at 100 °C using R134a as working fluid.

Model				Inertia Models		
		NTU	ORC	Basic	Cold Out	Cold In
Section		6.2.1	6.2.1.2	6.2.2	6.2.2.2	6.2.2.2
Transferred exergy	$\dot{E}x_{\text{in}}$ (kW)	97.7	82	84.9	91.8	92.5
Net power	P_{net} (kW)	49.9	33.7	37.2	46.8	46.1
Self consumption	P_{self} (kW)	3.2	4.0	3.0	3.4	3.2
Second law efficiencies	$\eta_{\text{II,int}}$ (%)	51.1	41.2	43.8	51.0	49.8
	$\eta_{\text{II,ext}}$ (%)	89.7	75.0	77.9	84.2	84.8
	η_{II} (%)	**45.8**	**30.9**	**34.1**	**42.9**	**42.3**
Net energy per pass	E_{net} (MJ)	2.9	-	3.1	3.4	3.3
Cycle duration	t (s)	58.1	-	83.4	73.1	72.5
Heat transfer per HX	kA_{all} (kW/K)	39.5	-	13.5	19.7	21.7
Free volume	$V_{\text{HX},0}$ (m^3)	0.24	-	0.26	0.10	0.086
Plate thickness	s (mm)	-	-	0.6	1	0.9
Wave amplitude	a (mm)	-	-	1.5	1.5	1.5
Mass flow	$\dot{m}_{\text{WF,fill}}$ (kg/s)	19	-	20	20	20
Maximum mass	$m_{\text{WF,fill}}$ (kg)	36	-	40	40	40
Switch pressure	$p_{\text{WF,switch}}$ (bar)	10.8	-	11.7	11.7	11.9
Discharge flow	$\dot{V}_{\text{WF,dis}}$ (m^3/min)	5.55	-	4.35	4.88	4.95

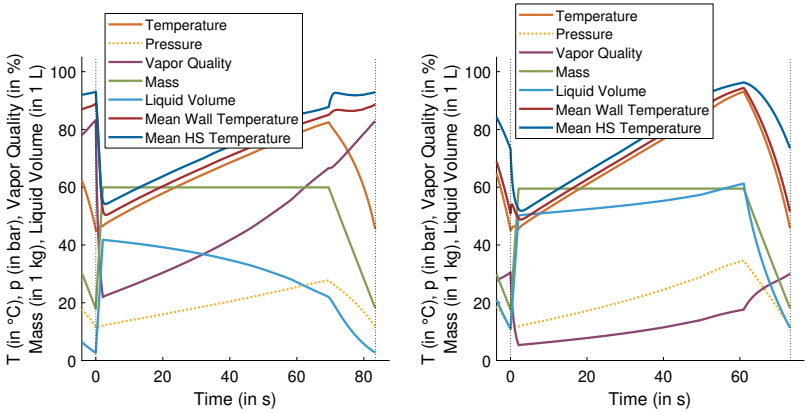

(a) Heated discharge

(b) Unheated discharge

Figure 6.7: Progress of the thermodynamic states in the evaporators of the detailed model.

liquid saturation line. As can be seen in fig. 6.7, re-evaporation still takes place during both the heated and unheated discharge phase (the vapor quality further rises during the last phase of both cycles). The required heat is taken from the hot heat source for the heated discharge in fig. 6.7a. For the unheated discharge in fig. 6.7b, the heat is taken from the thermal capacity of the wall and the enclosed heat source. For the NTU-model, stored heat was not an issue and therefore the optimized cycle ended with all the working fluid vaporized and fed to the engine as can be seen in the T-s-diagram in fig. 6.8a on the next page (this special type of T-s-diagram was introduced and explained in section 4.1.1 on page 54, fig. 4.3). Only when the thermal inertia was introduced, it became crucial to utilize more of the stored energy. The optimization therefore ended up with more working fluid per batch. More liquid led to a more efficient heat transfer area (smaller share of gas–phase heat transfer due to the higher liquid level) and a better cooling of the wall. However, the cycle now ended with a significant amount of liquid working fluid that used energy to be heated, but was not evaporated and discharged (fig. 6.8b). Apparently, on a global scope it was advantageous to have the additional heat transfer area during

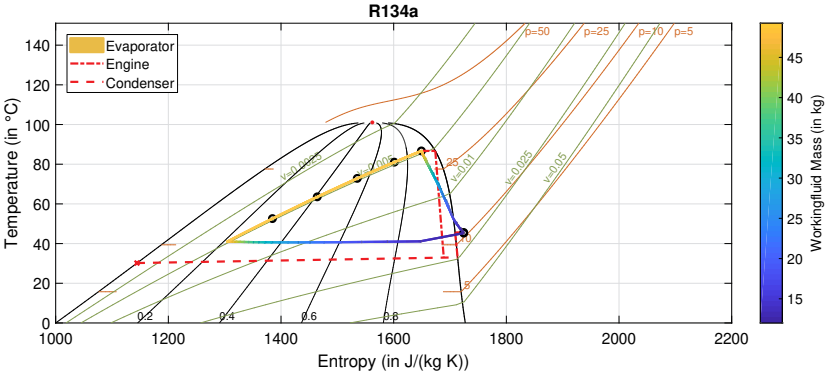

(a) NTU model

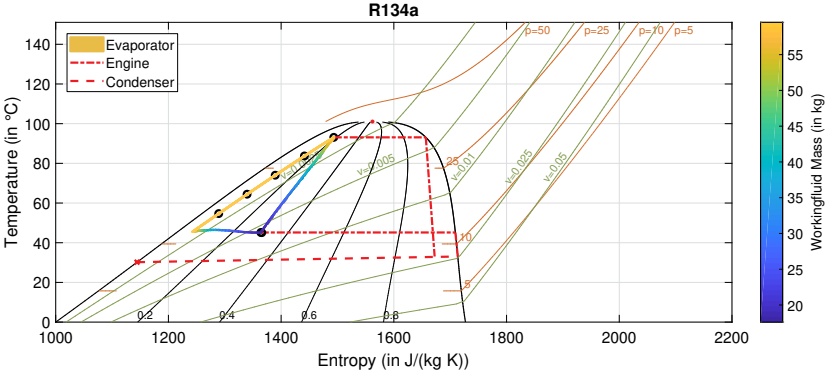

(b) Detailed model - unheated discharge

Figure 6.8: Comparison of an optimized cycle progress for different evaporator models.

Table 6.7: Selection of promising working fluids for ORC and MWW Cycle.

R-Number -	Composition -	T_{boil} °C	T_{crit} °C	p_{crit} bar	ASHRAE -	ODP -	GWP_{100} -
R134a	CH_2FCF_3	−26.1	101.1	40.6	A1	0	1430
R227ea	CF_3CHFCF_3	−16.3	101.8	29.3	A1	0	3580
R1234yf	CH_2CFCF_3	−29.5	94.7	33.8	A2L	0	<1
R1234ze(E)	$CHFCHCF_3$	−19.0	109.4	36.4	A2L	0	6
R1233zD(E)	$C_3ClF_3H_2$	18.3	165.6	35.7	-	0	1
-	Isobutylene	−6.9	144.8	40.0	-	-	-

the discharge and accept the unused remaining liquid working fluid.

6.3 Comparison of Working Fluids

All previous examples and simulations were performed with R134a as working fluid in order to exclude the influence of another free variable. In the previous section this was desired for the sake of comparability. However, with the discussed impact of a matching working fluid on the ORC (section 2.1.3.1), a wider comparison of different working fluids for both ORC and MWM will be presented in this section.

With regard to the extensive computation time of the MWM optimizations, a restricted preselection of working fluids had to be made. Kolbeck [99] performed a specific screening for the MWM Cycle and identified a dozen promising fluids. Based on his evaluation, the best ones for 100 °C, 120 °C and 140 °C, respectively, were used for the further optimizations. The analyzed fluids and their properties are presented in table 6.7. The thermodynamic data is taken from REFPROP [72]. General information on the recent low–GWP refrigerants is taken from the manufacturers materiel safety data sheets (Honeywell [100]). Where available, the physical properties were also validated against literature values [101–104].

6.3.1 Heat Source at 100 °C

An overview of the best results of an ORC at a heat source temperature of 100 °C is given in table 6.8 on the next page. For reference, the already known case with R134a from section 6.2.1.2 is shown again in the first column. As a second entry, the promising R227ea from fig. 2.7 is selected. Even though it is not recommended anymore due to its high GWP, it is presented for thermodynamic comparison. As a currently recommended replacement–fluid in this temperature range, R1234ze(E) is added to the table. As last, the flammable, but environmentally interesting isobutylene is added.

R227ea showed an impressive performance at 120 °C according to the short-cut model. The detailed results from ASPEN show a rather small advantage over R134a of only 1 % at 100 °C. With a process pressure of 14.2 bar, the evaporation temperature is obviously too far away from the fluids critical temperature. Anyway, due to their environmental influence both these fluids were only included as thermodynamic benchmark. The net power of the case with the currently recommended R1234ze(E) is only 2 % smaller than the reference case and therefore proves to be a suitable alternative. The lower process pressure, compared to R134a, is another advantage with regard to equipment costs and complexity. The last entry, isobutylene, shows a rather weak performance that is about 8 % smaller than the others. Even though the low process pressure saves some power for the feed pump (see P_{self}), this case cannot compete with the others. It was still added to the list as it shows very good results in the MWM Cycle.

The corresponding results of the MWM Cycle are summarized in table 6.9 on page 129. Based on the discussion in section 6.2.2, all further cases were optimized with an unheated discharge phase and six heat exchangers. Again, the ORC with R134a is added in the first column as thermodynamic benchmark, followed by the same four fluids as for the ORC–cases.

The results in the second column for the MWM Cycle with R134a are already known from table 6.6. Despite the moderate heat transfer ability of only 20 kW/K, the high net power leads to an advantage over the ORC of +38.8 %.

Similar to the ORC cases, the MWM Cycle with R227ea does not perform as good as expected. Even though the optimization resulted in a higher heat trans-

Table 6.8: Cycle performance of the ORC for different working fluids at a heat source temperature of 100 °C.

Fluid		R134a	R227ea	R1234ze(E)	Isobutylene
Net power	P_{net} (kW)	33.7	34.2	33.1	30.9
Self consumption	P_{self} (kW)	4.0	4.2	3.7	2.3
Second law efficiencies	$\eta_{II,int}$ (%)	41.2	39.6	40.0	39.4
	$\eta_{II,ext}$ (%)	75.0	79.1	75.9	71.9
	η_{II} (%)	**30.9**	**31.4**	**30.4**	**28.3**
Evaporation pressure	p_{evap} (bar)	20.0	14.2	15.0	9.1
Condensation pressure	p_{exp} (bar)	8.4	5.9	6.4	4

Table 6.9: Cycle performance of the MWM Cycle for different working fluids at a heat source temperature of 100 °C (unheated discharge and six heat exchangers).

Cycle		ORC	MWM			
Fluid		R134a	R134a	R227ea	R1234ze(E)	Isobutylene
Net power	P_{net} (kW)	33.7	46.80	41.80	46.70	50.10
Self consumption	P_{self} (kW)	4.0	3.40	3.20	3.00	2.20
Second law efficiencies	$\eta_{\text{II,int}}$ (%)	41.2	51.00	48.20	50.10	51.60
	$\eta_{\text{II,ext}}$ (%)	75.0	84.20	79.50	85.40	89.00
	η_{II} (%)	**30.9**	**42.90**	**38.30**	**42.80**	**46.00**
Heat transfer per HX	kA_{all} (kW/K)	-	19.70	24.81	20.45	33.47
Free volume	$V_{\text{HX},0}$ (m^3)	-	0.10	0.07	0.11	0.80
Plate thickness	s (mm)	-	1.00	0.60	0.98	1.20
Wave amplitude	a (mm)	-	1.50	1.50	1.50	1.50
Mass flow	$\dot{m}_{\text{WF,fill}}$ (kg/s)	-	20	20	20	20
Maximum mass	$m_{\text{WF,fill}}$ (kg)	-	40	40	40	40
Switch pressure	$p_{\text{WF,switch}}$ (bar)	-	11.70	9.67	8.85	5.07
Discharge flow	$\dot{V}_{\text{WF,dis}}$ (m^3/min)	-	4.88	5.93	6.45	10.95

fer ability, the external second law efficiency is lower. The higher discharge flow and the slightly lower needed pump power can still not compensate this drawback.

The third case shows that, like for the ORCs, R1234ze(E) in a MWM Cycle performs almost as well as R134a. A slightly lower internal efficiency is outweighed by an increased heat transfer. The total net power ($P_{\text{net}} = 46.7\,\text{kW}$) and system efficiency ($\eta_{\text{II}} = 42.8\,\%$) thereby are 38.5 % higher than the ORC benchmark. With regard to its environmental properties, R1234ze(E) clearly is a suitable replacement for R134a.

Isobutylene in the last column, which was not efficient at all in the ORC, shows very promising results in the MWM Cycle. A good heat transfer, high internal efficiency and low self consumption combine to a total net power of $P_{\text{net}} = 50.1\,\text{kW}$ ($\eta_{\text{II}} = 46.0\,\%$). This is an improvement of almost 49 % over the ORC with R134a. The optimization results indicate that the high efficiency was reached at the cost of bigger equipment. While the thermodynamic performance benefits from the increased heat transfer ability, free volume and discharge flow, the corresponding component costs will have a negative impact on the economic rating as will be discussed in section 6.4.

From a purely thermodynamic point of view, the MWM Cycle with Isobutylene is the recommended pick that clearly outperforms any of the compared ORCs at a heat source temperature of 100 °C. If the flammability of the fluid is an issue, the MWM cycle with R1234ze(E) is a good-performing and environmentally suitable alternative.

6.3.2 Heat Source at 120 °C

The detailed numbers for all optimizations with a heat source temperature of 120 °C can be found in appendix C.1 on page 207. In addition to the previously discussed fluids, R1233zd was added as a current replacement-fluid with a critical temperature above 100 °C. In the ORC, the maximal process temperature is considerably lower than the heat source temperature due to the pinch point. In contrast, the working fluid in the MWM Cycle reaches peak temperatures close to the heat source. Therefore, the higher heat source temperatures of 120 °C and 140 °C made it necessary to consider some additional working fluids.

The ORC with R134a yields a net power of $P_{\text{net}} = 51.2\,\text{kW}$ (see table C.1), which is more than 50 % better than at 100 °C. About half of this can be correlated to the increased heat source temperature and the gain of the available exergy by 22 %. Consequently, the second law efficiency merely increases by 25 % from $\eta_{\text{II}} = 30.9\,\%$ to 38.5 %. Only this latter improvement can actually be accounted to a better temperature match, which supports the commonly recommended temperature range for R134a of 120 °C to 160 °C.

According to Liu et al. [25], 120 °C is the optimal heat source temperature for R227ea. The corresponding optimized case does in fact reach a net power output of $P_{\text{net}} = 53.8\,\text{kW}$ and an efficiency of $\eta_{\text{II}} = 40.4\,\%$ which is even better than R134a by 5 %. However, the predicted second law efficiency of the shortcut model (61 %) is not achieved. A matching working fluid typically can be found with a critical temperature close to the heat source temperature. As the shortcut model assumes constant fluid properties, its errors become larger in this near–critical range. Still, the prediction of the general suitability was correct.

The results of the cycle with R1234ze(E) lie again close to, but lower than R1234a and R227ea. The provided net power of $P_{\text{net}} = 49.6\,\text{kW}$ results in a second law efficiency of $\eta_{\text{II}} = 37.2\,\%$ (3 % less than R134a). With regard to the environmental limitations, this setup still proves to be the best performing viable ORC at this temperature range.

Isobutylene does again not perform too well in the ORC. With a net power of only $P_{\text{net}} = 44.8\,\text{kW}$ ($\eta_{\text{II}} = 33.7\,\%$) it cannot compete with the other fluids. Its critical temperature of 145 °C is already an indicator that it would be better suited for higher temperature ORCs.

Regarding the even higher critical temperature of R1233zd, the low net power output of $P_{\text{net}} = 41.9\,\text{kW}$ was expected. Even the low process pressure of only 6.4 bar and the resulting remarkably low auxiliary power of $P_{\text{self}} = 1.9\,\text{kW}$ cannot provide a competitive cycle efficiency ($\eta_{\text{II}} = 33.7\,\%$).

The results for the MWM Cycle are again benchmarked against the ORC with R134a. Its MWM counterpart yields a net power output of $P_{\text{net}} = 59.3\,\text{kW}$ (summary in table C.2). The improvement over the ORC ($P_{\text{net}} = 51.2\,\text{kW}$) was ascribed in equal parts to an increased heat transfer efficiency (ORC: $\eta_{\text{II,ext}} = 82.5\,\%$ vs. MWM: $\eta_{\text{II,ext}} = 89.3\,\%$) and a reduced self consumption

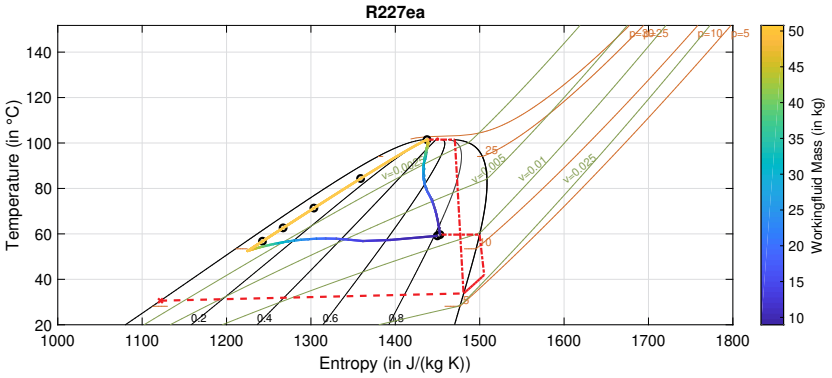

Figure 6.9: T-s-diagram of an optimization where the working fluid reached its critical temperature.

(ORC: 7.6 kW vs. MWM: 3.5 kW). However, the optimization ended up very close to the critical temperature of the working fluid and with a distinct wet expansion. The second law efficiency of $\eta_{\mathrm{II}} = 44.6\,\%$ is therefore rather a theoretical than practically achievable number.

The two following fluids, R227ea and R1234ze(E), are typically used for even lower temperatures than R134a and, as expected, also reach their critical temperatures in the MWM Cycle with a 120 °C-heat source. The results of their optimized cycles are still shown in table C.2 for completeness. The exemplary T-s-diagram in fig. 6.9 however illustrates that these cases are not recommended for practical implementation. The evaporation phase ends at a slightly supercritical state and the major part of the expansion takes place in the two–phase region. Neither the simulation model nor the introduced expansion engine are intended for these conditions. The basic idea of the MWM Cycle, a simple expansion engine compared to two–phase expanders and supercritical turbines, is therefore violated. With the comparably low cycle efficiencies of $\eta_{\mathrm{II}} = 40.1\,\%$ (R227ea) and $\eta_{\mathrm{II}} = 41.6\,\%$ (R1234ze(E)), these cases are not favorable anyways.

Without the limitation by their critical temperature, the higher–temperature fluids can show their potential. Isobutylene yields a net power output of $P_{\mathrm{net}} = 65.9\,\mathrm{kW}$, which is about 29 % higher than the ORC. The efficiency of

η_{II} = 49.6 % comes again at the cost of the requirements for an above–average gas volume and engine displacement.

The thermodynamic results with R1233zD are identical to the numbers of R134a: a net power output of P_{net} = 59.3 kW leads to a cycle efficiency of η_{II} = 44.6 %. The low process pressure allows for a further reduced pump power (P_{self} = 2.6 kW), but also causes an increased volume demand (free gas volume and discharge flow). In the thermodynamic context, this fluid still has a lead over the ORC of about 16 %.

In summary, the advantage of the MWM Cycle over the ORC becomes smaller with the increased heat source temperature. However, this is not caused by poor performing MWM Cycles, but rather by the boosting ORCs. The second law efficiencies of the MWM Cycles did only slightly increase, as the temperature match was already quite good for the 100 °C–cases. In contrast, the previous lack of matching working fluids for the ORC had now vanished and they could catch up to a proper performance.

6.3.3 Heat Source at 140 °C

The results of the ORC and MWM optimizations at 140 °C can also be found in appendix C.1 on page 207. For the ORC, the previous five working fluids are again presented. With the further increased heat source, the first three of the ORC cases even came close to the critical temperature of the working fluids. The evaporation temperature in the Aspen model was therefore limited to purely sub–critical cycles. The MWM cases will only be presented for the higher–temperature fluids as the low–temperature ones were already limited in their performance at 120 °C.

The benchmark ORC with R134a was one of the cases limited by the critical temperature of the working fluid. With the additional superheating, the highest feasible evaporator pressure was found at 30.4 bar (see table C.3). The net power output at these conditions was P_{net} = 72.2 kW, which equals a further increase over the 120 °C-case of 41 % (R134a with heat source at 120 °C: P_{net} = 65.9 kW). While most of this rise results from the increased available exergy, the second law efficiency still increases from η_{II} = 38.5 % to η_{II} = 46.4 %. This improvement is mainly based on the almost ideal heat transfer efficiency of $\eta_{II,ext}$ = 96 %. With the process pressure being that

close to the critical temperature of the working fluid, the cycle starts to profit from the improved temperature match that is also the motivation for trans– and supercritical ORC implementations. If the typical ORC turbines are still suitable for this state should be checked for the individual designs.

The other fluids show the same general behavior as for 120 °C: R227ea performs slightly better than R134a (P_{net} = 76 kW, η_{II} = 48.4 %) with an outstanding external efficiency of $\eta_{II,ext}$ = 98.4 %. R1234ze(E) yields an output somewhere in between and thus lies higher than R134a this time (P_{net} = 72.7 kW, η_{II} = 46.7 %). The two higher–temperature fluids improve their performance compared to the 120 °C-cases, but still cannot compete with the previous three fluids. Isobutylene reaches a second law efficiency of η_{II} = 38.7 %, whereas R1233zD(E) only reaches η_{II} = 36.2 %. For even higher heat source temperatures, the limitation to subcritical conditions would affect the first three fluids. Only under these circumstances are these two medium–temperature fluids expected to excel.

R1234ze(E) has proven to be a high-performing alternative for the established low–temperature fluids R227ea and R134a in the range of 100 °C to 140 °C. With its uncritical environmental numbers it is expected to replace those two soon.

The MWM cases show no major changes at this heat source temperature. Regarding the limitation by their critical temperatures, only R1233zD(E) and Isobutylene are presented in table C.4.

The advantage over the ORCs is further reduced and Isobutylene can only reach a lead of about 11 % (P_{net} = 80.2 kW, η_{II} = 51.6 %). While this is still the highest performance of all conducted optimizations, the major advantage of the lowest temperature could not be maintained for the higher temperature levels.

R1233zD(E) that was previously already lower–performing than Isobutylene now only produces a net power of P_{net} = 72.9 kW and hence matches the ORC.

6.3.4 Summary of the Thermodynamic Results

As already discussed in the section about the fundamentals of working fluids (section 2.1.3.1), several studies put the lower temperature limit for reasonable

power generation around 80 °C to 100 °C [2, 6, 25]. The main reason, as elaborated by Lecompte et al. [2], is the current lack of environmentally friendly, but yet high–performing working fluids at and below this limit.

With regard to the thermodynamic evaluation, the MWM Cycle fills this gap. Due to the adjusted temperature profile, the recent environmental replacement fluid R1234zE(E) and the olefin Isobutylene already start to perform well at 100 °C. At higher temperatures, these fluids also reach their recommended temperature range in the ORC and the advantage of the MWM Cycle decreases. This behavior of the MWM Cycle supports the statement of Lecompte et al. [2] that advanced cycles can primarily show their full potential in low temperature applications.

In summary, the thermodynamic results, especially at low temperatures, are promising for the MWM Cycle. The final decision about any practical implementation will, however, almost always be based on the economic performance. Both the ORC and MWM show a second law efficiency of about 30 % to 45 % at 100 °C. This is a reasonable conversion rate of the available exergy for a low temperature application. Still, their absolute power output is quite small. A net power output of about 50 kW means that only 5 % (first law efficiency η_{I}) of the available energy ($\dot{Q}_{\mathrm{av}} = 1\,\mathrm{MW}$) are converted to power. Even though both cycles perform well regarding the theoretical thermodynamic limitations, their profitable operation is therefore challenging.

6.4 Economic Evaluation

While the previous section rated and compared the cycles on their purely thermodynamic performance, this section finally evaluates the economic performance of MWM against ORC. First, the important economic figures will be introduced based on the example of the reference ORC (100 °C, R134a). Second, the results will be rated against literature values in order to validate the economic model. At last, the results of ORC and MWM will be compared. In addition, the influence of the working fluid selection and different heat source temperatures will be shortly addressed.

Table 6.10: Economic performance of the ORC at a heat source temperature of 100 °C (R134a).

Evaporation pressure	p_{evap} (bar)	20	16	24
Annuities	$A_{N,C}$ (€)	−8358	−7970	−7968
	$A_{N,O}$ (€)	−14 972	−14 628	−14 681
	$A_{N,P}$ (€)	55 936	51 292	51 631
	A_N (€)	**32 606**	**28 693**	**28 982**
Bare Module Costs	pump (€)	21 964	20 346	22 790
	turbine (€)	45 163	41 909	42 304
	condenser (€)	6267	7671	4869
	evaporator (€)	1333	1430	1198
Initial Investment	K_0 (€)	110 060	104 940	104 710

6.4.1 Details of the Economic Key Performance Indicators at the Example of the Reference ORC

All cases were optimized targeting the total annuity A_N. The global and project specific reference conditions were the same for all ORC cases. The only free variable was therefore the evaporation pressure. The data from the sensitivity analysis of the ORC was now also used for the economic evaluation.

6.4.1.1 Economic versus Thermodynamic Optimum

For all the analyzed ORC cases, the economic optimum was identical to the thermodynamic one. The data for the optimized reference ORC (20 bar - table 6.10) shows the total annuity A_N and its single elements: annuities of capital-related costs $A_{N,C}$, operation-related costs $A_{N,O}$ and proceeds $A_{N,P}$. In addition, the bare module costs of all components are given as the source of the capital related costs. The two main factors are the turbine (45 163 €) and the feed pump (21 984 €). The heat exchangers (evaporator and condenser) only account for 1333 € and 6267 €, respectively. Adding the additional costs for the grid connection and the percentages for engineering, auxiliary construction and the instrumentation leads to the total initial investment K_0.

It can be seen in fig. 6.10 on the next page that the variation of the evapora-

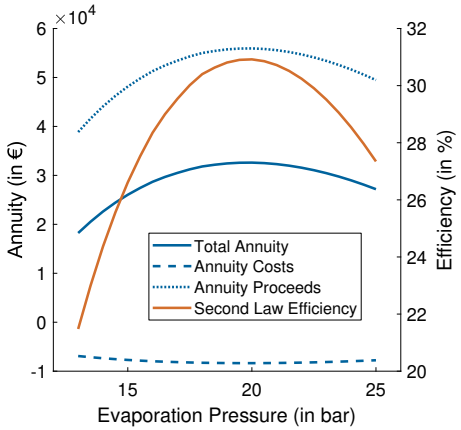

Figure 6.10: ORC sensitivity analysis of economic figures and efficiency over evaporation pressure.

tion pressure has a major impact on the proceeds (which are directly dependent on the power output) and only a minor impact on the costs. As known from the thermodynamic evaluation, a higher evaporation pressure (see column "24 bar" in table 6.10) would increase the internal efficiency, but reduce the totally transferred energy and the internal flow rate of the working fluid. This would require smaller and therefore cheaper heat exchangers, but also a more expensive feed pump due to the higher pressure. The costs of the turbine would also be increased by the higher pressure level, but this effect is almost completely outweighed by the smaller required dimensions for the reduced throughput of the cycle. A lower evaporation pressure (see column "16 bar" in table 6.10) would reduce the internal efficiency, but would increase the transferred heat. The reduced costs for pumps and turbine (lower pressure) would be opposed to an increasing size of evaporator and condenser. In summary, it can be seen that the case with the highest efficiency is also the most expensive one. With regard to the annuities, the optimized 20 bar-cases has about 400 € higher annual costs than the other two examples. Nevertheless, the higher investment pays off in form of a major increase in power production and proceeds of about 4000 €/a. For all the optimized ORCs, the case with the

highest thermodynamic efficiency consistently also provided the highest total annuity.

The operation related costs are also partly based on the initial investment. The influence on the optimal evaporation pressure however is small. For the exemplary 20 bar-cases, the major part (about 63 %) consist of the estimated fixed personnel expenses for the operation. Only 27 % and 10 % are allotted to the capital–cost–dependent shares for maintenance and inspection. The operation related annuities are therefore almost identical for the three cases in table 6.10 and do not distinctly affect the total annuity.

6.4.1.2 Comparison of Annuity and Internal Rate of Return for Different Fluids

Table 6.11 on the facing page shows the economic figures for optimized ORC cases at 100 °C with different working fluids. The first rows show the already known thermodynamic figures from table 6.8. For the following comparison, the economic figures from the previous section as well as three additional ones were added: the specific investment costs (SIC), the internal rate of return (IRR) and the dynamic payback time (dPBT).

As discussed in section 2.2, the annuity rates the total absolute cash output over the whole observation period. The reference case shows a high annuity of $A_N = 32\,606\,€$ compared to the other fluids. Together with the also high–performing R227ea ($A_N = 33\,476\,€$), these two investments would yield the highest absolute profit from the given heat source. Comparing these results with the thermodynamic efficiencies from table 6.8 on page 128 shows that these two cases are also the ones with the highest power output. However, the higher power output requires higher initial investment costs K_0. Simply put, the first two cases have their optimum at larger cycle layouts which produce more power but are also more expensive and therefore bind more capital. With regard to the total annuity, the gain from the higher power output outweighs the additional costs (Similar to the sensitivity analysis in fig. 6.10).

In contrast, the case with Isobutylene shows a lower annuity of only $A_N = 29\,940\,€$. Due to the thermodynamic limitations with this fluid, this setup can not access the full potential of the heat source. On the upside, neglecting the inaccessible heat, the cycle design can be smaller and less expensive. Comparing the bare module costs in table 6.11 shows that all components

Table 6.11: Economic performance of different fluids in the ORC at a heat source temperature of 100 °C.

Working fluid		R134a	R227ea	R1234ze(E)	Isobutylene
Evaporation pressure	p_{evap} (bar)	20.0	14.2	15.0	9.1
Annuities	$A_{N,C}$ (€)	−8358	−8314	−7982	−7098
	$A_{N,O}$ (€)	−14 972	−14 963	−14 757	−14 277
	$A_{N,P}$ (€)	55 936	56 754	54 976	51 266
	A_N (€)	**32 606**	**33 476**	**32 236**	**29 940**
Economics	SIC (€/kW)	3266	3206	3177	3035
	IRR (%)	41.8	42.8	43.0	44.6
	dPBT (a)	2.5	2.5	2.5	2.4
Bare Module Costs	pump (€)	21 964	20 869	20 107	16 936
	turbine (€)	45 163	45 361	43 716	39 764
	condenser (€)	6267	6588	6298	5800
	evaporator (€)	1333	1547	1300	1098
Initial Investment	K_0 (€)	110 060	109 610	105 230	93 738

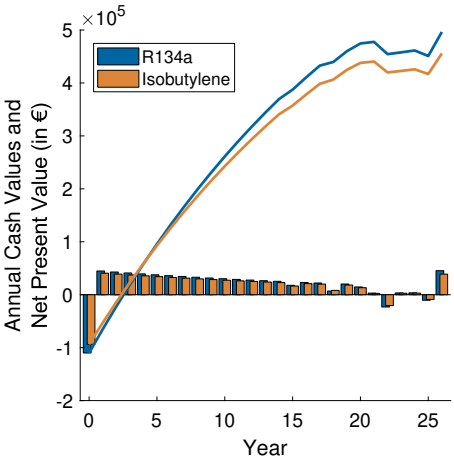

Figure 6.11: Annual cash values (bars) and net present value (lines) of two optimized ORCs with R134a and Isobutylene.

are cheaper than for the other three cases. The reduced transferred heat only needs smaller heat exchangers, the lower power output requires a smaller turbine and the lower process pressure leads to a cheaper feed pump. The total initial investment K_0 is therefore almost 15 % smaller than for R134a. As expected, the annuity of the proceeds is significantly reduced by the smaller cycle design and can not be compensated by the lower costs. However, with regard to a short–term evaluation, the net present value (NPV) of this small design gains faster during the first years and leads to a shorter payback time (dPBT) of only 2.38 a.

In summary, the recommendations for the selection of a setup can be visualized in Figure 6.11. The bars show the individual annually cash values for a large (R134a) and a smaller (Isobutylene) ORC. The accumulated cash values (net present value, shown as lines) start with the negative initial investment and rises with the annual proceeds. The point where the net present values becomes positive marks the dynamic payback time. The upcoming replacement costs for the equipment can clearly be seen at for example 15 a or 21 a as dent in the annual cash values. At the end of the observation time T, the

residual value R_W of the single components is returned which causes a final rise in the net present value.

If there was unlimited or at least sufficient capital, the more expensive designs would still pay off as they are able to harness more of the heat source potential (especially for long–term projects). In the dynamic economic evaluation, they yield higher total annuities (and cash values) and therefore would return the highest absolute profit over the whole observation period (final value of accumulated cash values). However, the initial investment for these analyzed cases was so much higher than their improved power output that the specific investment costs (SIC) were increased. Consequently, it took longer to make up for the first investment and the payback times were longer (accumulated cash values reaches zero).

If the capital was limited and there were other promising investments, the smaller and more cost–efficient designs might be advantageous. They can not utilize the full potential of the given heat source and some of the available energy and exergy will be lost. But already the static evaluation method of specific investment costs (SIC) predicts a better cost efficiency. Not only do they have a better start due to the smaller initial investment (see shorter payback time). Also the dynamic internal rate of return method (IRR) confirms a higher cost efficiency for the long–term observation. They do not achieve the same absolute amount of profit as the larger designs, but instead leave some capital for other investments (which will also provide some additional profit).

The final decision for or against an investment is therefore highly dependent on available capital, company strategies and the expected development of the market.

6.4.1.3 Influence of Assumed Compensation

The comparison in the previous two sections showed that the total profitability is primarily subject to the proceeds of a setup. So far, all previous economic numbers were calculated with an assumed high revenue from the EEG–funded rates for geothermal renewable power. As the feasible size of a MWM Cycle is expected to be limited, this cycle might not be best suited for the scales of a geothermal power plant. Especially the high initial costs for exploration and drilling will most likely not be covered by the electricity sales. In order to

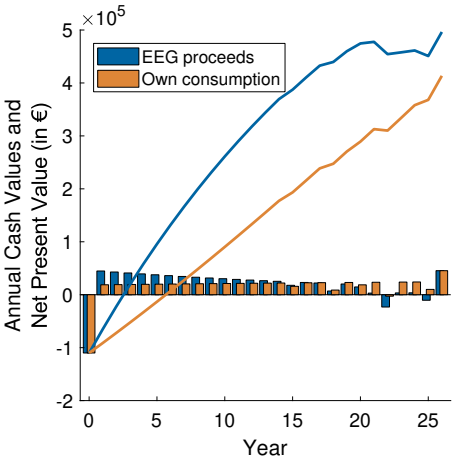

Figure 6.12: Annual cash values (bars) and net present value (lines) of the optimized ORCs with R134a: Proceeds based on subsidized rates for geothermal power and savings by self-consumption.

cover the alternatives, this section will evaluate the self-consumption of the produced electricity with the proceeds being the saved expenses.

The benchmark was the already known ORC with R134a (100 °C). The optimized operation point was identical for the thermodynamic optimization from section 6.2.1.2 , for the case with the EEG–subsidized "Geo"-proceeds from section 6.4.1.1 and for the here presented direct use of the produced power. For all following ORC cases and fluids, the minor changes of the economic reference conditions did not shift the optimized operation point. Like for the varied process pressure in section 6.4.1.1, the achieved power output of the thermodynamic optimum would obviously define the perfect operation point over any variations of component costs, proceeds or operation hours.

Figure 6.12 shows again the cash values for the reference case from fig. 6.11, but compares them to the cash values with the reduced revenues. As also shown in table 6.12 on the facing page, both cases start with the same initial investment of about 100 000 €. At the beginning, the EEG–based revenues of

Table 6.12: Economic performance of the ORC at a heat source temperature of 100 °C with different models for the proceeds.

Proceeds		Geo	self-consumption
Annuities	$A_{N,C}$ (€)	−8358	−8358
	$A_{N,O}$ (€)	−14 972	−14 972
	$A_{N,P}$ (€)	55 936	49 797
	A_N (€)	**32 606**	**26 466**
Economics	SIC (€/kW)	3266	3266
	IRR (%)	41.80	22.50
	dPBT (a)	2.54	5.66
Initial Investment	K_0 (€)	110 060	110 060

0.25 €/kWh (blue) clearly outperform the estimated savings for self-consumption of 0.132 €/kWh (orange). However, the cash values with the original proceeds decrease over the years as the annual fixed rates had to be discounted for the dynamic model. In addition, the guaranteed refund rate ends after 20 a and only the estimated market price was used for the last 5 years. In contrast, the initially lower savings slightly rise over the years, because the discounting with the interest rate ($q = 1.04$) is balanced by the assumed price change factor for electricity ($r_{elec} = 1.04$). The discounting of the operational costs then outweighs the assumed corresponding price change factor $r_O = 1.015$ and causes the moderately increasing values. The final net present value ends up being a reasonable positive number. Still, the longer payback time of 5.7 a, the reduced annuity ($A_N = 26\,466$ €) and the smaller internal rate of return (22.5 %) emphasize the major influence of the proceeds (see table 6.12).

Most studies about the profitability of geothermal powered ORCs separate two different economic considerations as will be seen in section 6.4.2.2. The static method of specific investment costs is used for the rating of the initial costs of the bare ORC module. This facilitates to compare different concepts and cycle layouts with regard to their efficiency. The substantial share of costs for exploration and drilling is only then added to another, dynamic method. For example, the annuity or the total levelized costs of electricity (LCOE) are used to evaluate the economic viability of the whole plant, including all auxiliary

costs. Using the combination of EEG compensations for geothermal power, but neglecting the drilling costs in the reference case does therefore not give a reliable conclusion about the overall profitability ("Geo" in table 6.12). Adding the immense drilling costs to the evaluation of the small scale MWM Cycles would not be productive. Instead, using the savings from self-consumption in the economic evaluation leads to a much more realistic assessment ("self-consumption" in table 6.12). A payback time of about 6 years lies for example closer to literature values for other ORC cases. Preißinger, Heberle, and Brüggemann [19] for example report payback times in the range of 9 years to 13 years in their study about a ORC with a 35 MW geothermal heat source. It was previously shown that the selection of proceeds does not affect the optimal operation point and has therefore no influence on the static numbers like initial costs and SIC of the current model. The previous optimizations can thus still be used for comparison among themselves and for a rating against specific investment costs from literature in the next section.

6.4.2 Validation of the Economic Model Against Literature

In order to validate the presented economic model, the results for all ORC cases were rated against literature values. The exact details, like observation time and interest rates, vary from study to study and complicate an objective comparison. Avoiding the different dynamic factors leaves the static economical methods. Consequently, the specific investment costs were compared to a range of ORC evaluations from literature.

6.4.2.1 Overview over the Optimized ORC Cases

The detailed results for the economic optimization of the further ORC cases can be found in appendix C.2 on page 207. In the lines of table 6.11, the numbers for 120 °C and 140 °C are summarized in table C.5 and table C.7, respectively.

The best operation points for all cases are almost identical to their thermodynamic optimum. As expected, the increased power output of the higher temperature cases causes improved economic figures. The high thermodynamic performance of the case with R227ea at 120 °C, for example, leads to

an annuity of the proceeds of $A_{N,P} = 88\,266\,€$, which is an increase of 55 % over the best performing ORC at 100 °C (R227ea: $A_{N,P} = 56\,754\,€$). With the rising costs of only 40 % (from $K_0 = 110\,060\,€$ to $K_0 = 153\,620\,€$), the total annuity as well as the internal rate of return could also be increased. The better thermodynamic performance can also be seen in the lower specific investment costs and the reduced payback time. This general trend can be observed for all fluids. Still, the different fluids within this temperature range can be grouped into cases with higher total profit and cases with higher economic efficiency like for the 100 °C run. Again, R134a and R227ea show the higher initial costs, but achieve the highest total output in a long term observation. Isobutylene and also the added R1233zD have the lower investment, shorter payback time and better internal rates of return, but can not compete in terms of total annuity.

For the highest analyzed heat source temperature of 140 °C, the results show the same behavior. The general level of power output is further increased and the economic numbers are positively affected. The best performing fluid is again R227ea with a total annuity of $A_N = 89\,448\,€$. The detailed bare module costs in table C.7 show that the already discussed very good temperature match of this fluid requires a larger heat exchanger area. The evaporator area for R227ea ($A = 47.0\,m^2$) is almost doubled compared to R134a ($A = 29.2\,m^2$). However, compared to the other costs for turbine and pump, the costs for the heat exchangers (R227ea: $K_{0,evap} = 4434\,€$, R134a: $K_{0,evap} = 2819\,€$) are small and the specific investment costs are hardly affected.

6.4.2.2 Comparison to Literature

Table 6.13 on the following page summarizes different economic studies of ORCs for geothermal power production and waste heat recovery. While most of them cover a wider range of temperatures and dimensions, only the data most relevant for the present model was selected.

The thermo–economic evaluation of zeotropic mixtures of Heberle and Brüggemann [18] also includes the results for some pure fluids. Their reference is a geothermal heat source at 120 °C with about 15 MW of available energy. Their dynamic evaluation of the electricity generation costs (EGC) is based on an observation period of 20 a, but their calculations of the SIC do match the definition from section 2.2. Depending on the fluid, they reach a SIC between

Table 6.13: Comparison of literature values and model results for specific investment costs.

		Scale (MW)	Source (°C)	SIC (€/kW)
Heberle and Brüggemann [18]	Geo	15	120	3000 to 4000
Astolfi et al. [105]	Geo	90	120	1900
Preißinger, Heberle, and Brüggemann [19]	Geo	35	150	1250
Quoilin et al. [6]	WHR	1	n/a	2500
Quoilin et al. [24]	WHR	0.1	180	2100 to 4200
Meinel, Wieland, and Spliethoff [97]	WHR	1	240	2400
Imran et al. [106]	WHR	1	180	3500 to 5000
Current ORC cases	generic	1	100	3000 to 3300
	generic	1	120	2600 to 2900
	generic	1	140	2350 to 2700

3000 €/kW and 4000 €/kW. Astolfi et al. [105] consider the same temperature at a much larger scale of 90 MW. For this temperature they only show the specific investment costs including drilling and exploration with 3750 €/kW. However, based on their presented detailed numbers for 150 °C, a share of about 50 % can be assigned to the power block. This leads to about 1900 €/kW for the bare ORC module.

The scaling of different components can, according to Turton [47], be estimated by

$$\frac{K_a}{K_b} = \left(\frac{X_a}{X_b}\right)^n, \tag{6.4}$$

where K are the absolute costs and X are the characteristic dimensions of the two components a and b. A typical value for $n = 0.6$, leading to the name "six–tenth–rule". Applying this rather rough estimation to the specific costs of the whole ORC module predicts a ratio of $SIC_{90\,MW}/SIC_{15\,MW} = 0.49$, which

applies surprisingly well to the previously shown values.[4]

Preißinger, Heberle, and Brüggemann [19] use the payback time and a mean cash flow as dynamic evaluation methods for their ORC on a 35 MW geothermal heat source. The differing heat source temperature of 150 °C prevents a direct comparison, but adds to the pool of a valid range for specific investment costs. The low number of 1250 €/kW conforms to the model results from the previous section, where a higher temperature drastically improves the economic numbers.

The techno-economic survey of ORC systems from Quoilin et al. [6] gives a good overview of various fields of application for ORCs. Even though this survey does not contain any detailed calculations, a collection of data from "a non-exhaustive set of ORC manufacturers and from scientific publications" is given. A typical WHR application with a power output of 50 kW is given with total specific costs of 4000 €/kW and 2500 €/kW corresponding to the bare module. The estimated equal split from above between module costs and auxiliary costs is supported by these numbers. Typical system efficiencies of about 5 % for WHR applications allow concluding for a 1 MW heat source. Unfortunately, no exact temperatures and dimensions are given in this summary.

The former work of Quoilin et al. [24] includes a detailed optimization of a small scale WHR cycle. With a 180 °C gaseous heat source of only 100 kW, the challenges are to design a most simple and cost–efficient ORC. Using volumetric expanders like scroll and screw expanders together with suitable working fluids allows for specific module costs of 2100 €/kW to 4200 €/kW.

The following two WHR cases are also based on a medium temperature gaseous heat source and both evaluate a 1 MW variant of it. Meinel, Wieland, and Spliethoff [97] introduce alternative cycle designs as for example an ORC with regenerative preheating. The specific costs are only given including maintenance and operating costs. However, from the given system efficiency of about 13 %, the net power output of 130 kW can be deduced. With the given component costs, the initial investment follows as 315 000 € which finally leads to specific module costs of 2400 €/kW. At last, the work of Imran et al. [106] covers several working fluids and cycles setups. The power output between 30 kW and 120 kW equals a heat source in the range of 1 MW. The

[4] With SIC $= K/X$ follows $\mathrm{SIC_a}/SIC_\mathrm{b} = X_\mathrm{b}/X_\mathrm{a} \cdot \left(\frac{X_\mathrm{a}}{X_\mathrm{b}}\right)^{n}$

corresponding specific costs range between 3000 €/kW and 3300 €/kW.

The ORC cases from the previous sections are again listed in this table. Starting from 3500 €/kW to 5000 €/kW at 100 °C, the specific costs drop to lower numbers of 2350 €/kW to 2700 €/kW at 140 °C as expected. It could thereby be shown that the economic model fits the range of typical cost estimations found in literature. In comparison to the large scale geothermal ORCs, the presented costs of the small benchmark ORCs might seem marginally to small. A detailed comparison of the calculations demonstrated the mentioned uncertainties in the cost estimation. The shell and tube heat exchangers as used by Heberle and Brüggemann [18] yield for example a drastically lower heat transfer coefficient and lead to an increase of the total specific heat transfer area by the factor of 4. The plate heat exchangers represented by the correlation from section 5.3.2.1 do not only provide a better heat transfer but can also show lower specific costs. When comparing the presented model to the WHR cases, one has to keep in mind that the gaseous heat source requires an additional heat transfer loop. The actual temperature level that is available to the power cycle is therefore somewhat lower than the one shown for 180 °C. In addition, the intermediate thermal oil cycle requires another pump and an extra exhaust gas heat exchanger which both cause extra costs. Directly connecting to the heat source without the heat transfer loop would also be possible, but would further reduce the heat transfer and cause even more expensive heat exchangers.

In conclusion, it can be said that the results of the present economic model do fit the range of literature values and the model can be considered as validated. While the absolute numbers of any cost estimation are known to show a considerable uncertainty, the presented quality is sufficient for the comparison of the MWM Cycle to the benchmark ORCs and in order to give a general idea if a MWM plant would be profitable.

6.4.3 Economic Rating of the MWM Cycle

With the ORC benchmark being discussed and the economic model being validated, the economic performance of the MWM concepts can finally be rated. First, the detailed results of the MWM Cycle with the default reference conditions will be shown. In the end, some “what if?” scenarios of varied working fluids, adjusted operation hours and the different refund rates will be

given.

6.4.3.1 Economic versus Thermodynamic Optimum

In contrast to the ORC cases, the optimization of the MWM cycles was quite sensitive to the selected objective. For the ORCs, both thermodynamic and economic optimization led to the same operation point. For the MWM Cycle, the computations maximizing the annuity did result in a significantly different cycle setup and different operation conditions. An example is given in table 6.14 on the next page. The reference ORC with R134a at 100 °C is again shown as baseline. In addition, the best thermodynamic and the best economic MWM with R134a are opposed.

As already discussed, the thermodynamic optimized MWM Cycle yields a higher second law efficiency and higher power output than the ORC. With six evaporators and a total heat transfer of about $kA_{\mathrm{all}} = 20\,\mathrm{kW/K}$ per evaporator, an output of $P_{\mathrm{net}} = 46.8\,\mathrm{kW}$ is produced. However, with the assumed lower operation hours from section 6.1.2 of only 5000 h/a, the annuities of the revenues $A_{\mathrm{N,P}}$ are still slightly lower than the ones of the ORC (with 7000 h/a). In order to reach this thermodynamic maximum, the cycle layout ended up at a maximized working fluid mass per cycle and the required increased free volume. The resulting bare module costs show a slightly higher value for the feed pump of the MWM. The lower feed pressure in the MWM Cycle should lead to a cheaper feed pump, as the inputs to the cost correlation are only pump power and pressure factor. However, as discussed in section 6.2.1.1, the inlet of the fresh working fluid does not use the whole filling phase in the current model. A short, but intense feed burst helped to keep a constant pressure level during the filling. While this helped to reduce the total needed pumping energy, the costs of the pump (defined by the maximal rated capacity) increased. Therefore, the already mentioned prebuffering should also be considered economically. In contrast, the customized expansion engine of the MWM Cycle is actually cheaper than the ORC turbine. Compared to the order of magnitude of these values, the heat exchangers generate about the same costs for both ORC and MWM, even though the MWM Cycles uses six of them with a higher total surface area. At last, the vessel that is needed for the previously mentioned free volume (section 4.2.2) outranges all other costs and accounts for 105 000 € for the six heat exchangers. This leads to a

Table 6.14: Optimized results of the MWM Cycle for different objectives at a heat source temperature of 100 °C (R134a).

Cycle		ORC	MWM	
Objective		all	η_{II}	A_N
Net power	P_{net} (kW)	33.70	46.80	41.70
Self consumption	P_{self} (kW)	4.00	3.40	3.30
Second law efficiencies	$\eta_{II,int}$ (%)	41.20	51.00	48.10
	$\eta_{II,ext}$ (%)	75.00	84.20	79.60
	η_{II} (%)	**30.90**	**42.90**	**38.30**
Evaporators	(-)	1	6	4
Heat transfer per HX	kA_{all} (kW/K)	36.50	19.70	23.70
Free volume	$V_{HX,0}$ (m^3)	-	0.10	0.08
Plate thickness	s (mm)	-	1.00	0.70
Wave amplitude	a (mm)	-	1.50	1.60
Mass flow	$\dot{m}_{WF,fill}$ (kg/s)	-	20	7
Maximum mass	$m_{WF,fill}$ (kg)	-	40	37
Switch pressure	$p_{WF,switch}$ (bar)	-	11.70	13.10
Discharge flow	$\dot{V}_{WF,dis}$ (m^3/min)	-	4.88	4.43
Annuities	$A_{N,C}$ (€)	−8358	−21 454	−13 321
	$A_{N,O}$ (€)	−14 972	−18 689	−15 345
	$A_{N,P}$ (€)	55 936	54 660	48 746
	A_N (€)	**32 606**	**14 518**	**20 080**
Economics	SIC (€/kW)	3266	5698	3573
	IRR (%)	41.80	13.10	24.60
	dPBT (a)	2.54	7.44	4.22
Bare Module Costs	pump (€)	21 964	25 727	22 015
	expander (€)	45 163	38 887	35 566
	vessel (€)	-	105 040	31 390
	condenser (€)	6267	7286	6669
	evaporator (€)	1333	3215	2466
Initial Investment	K_0 (€)	110 060	266 650	149 120

total initial investment of almost 267 000 € and a high SIC of 5700 €/kW. The total annuity of the "thermodynamic" MWM is accordingly at a low value of only $A_N = 14\,518$ € compared to the $A_N = 32\,606$ € of the ORC. The resulting payback time of 7.44 a and the internal rate of return of 13.1 % can also not compete with the ORC.

The economic optimization of the MWM Cycle considered these main cost factors accordingly. The best case used only four heat exchangers and did also not completely utilize the maximal working fluid mass. Consequently, the needed free volume is significantly reduced by 20 %. These reduced dimension limited the possible net power output to $P_{net} = 41.7$ kW. The annuity of the proceeds was thereby even further reduced to $A_{N,P} = 48\,746$ €. The costs, however, could also be drastically cut down: pump and expander are slightly reduced and the heat exchangers stay almost the same. Most importantly, the costs of the four vessels are reduced to 31 390 €. This combination leads to a more feasible SIC of 3573 €/kW. The annuity of the costs is over-proportionally high compared to the ORC because the estimated lifespan of the expansion engine is only half of the turbine. While the SIC is only based on the one–time initial costs, the cost annuity does also include the replacement procurements. The operational costs are again hardly affected by the initial investment as most of them originate from the wages. The total annuity of the "economic" MWM Cycle reaches $A_N = 20\,080$ €. The resulting payback time of 4.2 a and the internal rate of return of 24.6 % are still lower than the ORC, but much better than the numbers of the thermodynamic optimum.

The magnitude of the vessel costs raises the question of the validity of the cost estimation for this component. As discussed in section 5.3.2.2, the data availability in literature is rather thin for simple pressure tanks. Even though several compared correlations did result in the same cost range, the values seem over-proportionally expensive. Where a vessel with a volume of 0.1 m^3 would lead to bare module costs of 8600 €, even a more complex plate exchanger with the same free volume would only be at 6150 €. The significant difference between the two examples in table 6.14 is also mainly caused by the correlation itself. The thermodynamic cases uses a slightly bigger free volume and also reaches an increased maximal process pressure of 41 bar compared to the 38 bar of the economic case. This small variation results in a calculated wall thickness of more than 6.3 mm for the former one. According to eq. (2.37), the pressure factor F_p then jumps from a constant 1 to a pressure dependent

Table 6.15: General sensitivity of the MWM optimizations to the thermodynamic reference conditions.

Variation	P_{net}	η_{II}	K_0	SIC	A_N
Number of Heat Exchangers ↑	↑	↑	↑	↗[5]	⊗[6]
Heat Source Temperature ↑	↑	↑	↑	↘	↗

[5] general trend with exceptions
[6] no clear trend

factor of 2.8 in this case.

Obviously, the cost correlations of the custom components have to be checked and refined based on actual prices before a more detailed prediction of the profitability can be made. Also, the cost estimations for the feed pump can only be more detailed once the practical implementation of the feed phase is analyzed.

6.4.3.2 Overview over all Optimized MWM Cases

As a consequence of the findings in the previous section, an additional economic optimization was run for all MWM cases. Here, the influence of the temperature and the number of heat exchangers will be discussed. The general sensitivity to these reference conditions is summarized in table 6.15. As will be seen, the economic optimum was not found with a maximized number of heat exchangers, but is dependent on the reference conditions.

100 °C Heat Source Table 6.16 on the next page shows the most important thermodynamic numbers and the detailed economic figures of the 100 °C MWM cases with 3 to 6 evaporators and R134a as working fluid. As expected, the second law efficiency rises with the number of heat exchangers. Only the case with six evaporators poses as an outlier here. In contrast to the purely thermodynamic optimization, most of the free variables in these cases did not end up at their limits but rather somewhere in between. The most prominent examples are the total heat transfer and the working fluid mass flow which are not maxed out. For most of the free variables, no clear trend can be seen and

Table 6.16: Optimized economic results of the MWM Cycle for different numbers of heat exchangers (R134a with a 100 °C heat source).

Cycle		ORC	MWM			
Number of evaporators		1	3	4	5	6
Net power	P_{net} (kW)	33.70	38.10	41.70	42.10	38.30
Self consumption	P_{self} (kW)	4.00	2.90	3.30	3.30	4.10
Second law efficiency	η_{II} **(%)**	**30.90**	**35.00**	**38.30**	**38.60**	**35.10**
Heat transfer per HX	kA_{all} (kW/K)	36.50	20.60	23.70	16.90	39.50
Free volume	$V_{HX,0}$ (m^3)	-	0.10	0.08	0.05	0.07
Plate thickness	s (mm)	-	1.20	0.70	1.10	0.70
Wave amplitude	a (mm)	-	1.50	1.60	1.60	1.90
Mass flow	$\dot{m}_{WF,fill}$ (kg/s)	-	11	7	9	3
Maximum mass	$m_{WF,fill}$ (kg)	-	40	37	29	39
Switch pressure	$p_{WF,switch}$ (bar)	-	11.70	13.10	11.50	16.99
Discharge flow	$\dot{V}_{WF,dis}$ (m^3/min)	-	4.45	4.43	4.44	3.81
Annuities	$A_{N,C}$ (€)	−8358	−12 443	−13 321	−13 982	−14 141
	$A_{N,O}$ (€)	−14 972	−14 971	−15 345	15 640	15 582
	$A_{N,P}$ (€)	55 936	44 530	48 746	49 151	44 737
	A_N **(€)**	**32 606**	**17 116**	**20 080**	**19 529**	**15 015**
Economics	SIC (€/kW)	3266	3605	3573	3755	4320
	IRR (%)	41.80	23.50	24.60	23.10	18.60
	dPBT (a)	2.54	4.38	4.22	4.48	5.44
Initial Investment	K_0 (€)	110 060	137 440	149 120	158 030	165 480

their values vary due to the seemingly chaotic nature of the genetic algorithm. With the increasing number of evaporators, also the initial investment is gradually rising. The major impact originates from the additionally needed pressure vessel. The improved power output can compensate these additional cost for the 4–HX–case and leads to a better total annuity. The single values of this case were already discussed in detail in section 6.4.3.1. For the even larger setups, the costs could not be compensated and the economic figures get worse. The cases with five and six heat exchangers show a lower total annuity, smaller internal rate of return and a longer payback time. Interestingly, in contrast to the different ORC cases, the MWM setup with the highest total annuity (4 HX) is simultaneously also the most efficient one with regard to internal rate of return, payback time and specific costs.

120 °C Heat Source The corresponding numbers for a heat source temperature of 120 °C are given in the appendix in table C.6 on page 213. The results show the same trend as for 100 °C: the large setups yield a higher net power output and a higher second law efficiency, but are also more expensive with regard to their initial investment. The improved proceeds, however, shift the best case from four to five heat exchangers. With five rather small evaporators and a low pressure limit for the cycle timing, the lowest self consumption of only 3.4 kW leads to the highest net power output of 55.7 kW at this temperature level (ORC: 51.2 kW). While the resulting proceeds of $A_{N,P} = 65\,000\,€$ lead to good total annuity of $A_N = 26\,599\,€$, the high initial costs of 245 000 € result in the lowest internal rate of return and an increased payback time and SIC. Like for the ORCs, the highest total profit and the economically most efficient setup are again not identical. The small–scale alternative with only three heat exchangers provides almost the same total annuity ($A_N = 26\,320\,€$) at drastically reduced investment costs. Even though the lower net power output affects the proceeds, both the total annuity and the efficiency-factors SIC (3100 €/kW), IRR (30 %) and dPBT (3.5 a) are high–performing. Still, the ORC outperforms all of these numbers due to the higher assumed operation hours. While the initial investment and the SIC are actually quite close, the missing production hours of the MWM Cycle prevent a competitive overall economy.

140 °C Heat Source For the economic cases with a heat source temperature of 140 °C, R1233zD(E) was chosen as working fluid for the same reasons as for the thermodynamic optimizations (limitation by critical temperature of fluid). A direct comparison of single values of the various temperatures becomes therefore difficult. Table C.8 on page 215 shows for example that the lower pressure level of the feed pump changed from about 11 bar to 18 bar with R134a (table C.6) to 4 bar with R1233zD(E) (table C.8). The needed pump power is therefore lower and the cost correlations predicted cheaper feed pumps. The lower vapor density of R1233zD(E) leads on the other hand to a significantly higher volume flow through the expander. The cost correlations for expansion engine and turbine are however only dependent on the power and are therefore not sensitive to the volume flow. At the current state, correlations at this level of detail are not available for the MWM Cycle. Once more, the economic model can give an answer to the general profitability of the cycle, but more practical experience is needed in order to make more detailed cost estimations.

For these MWM cases with the higher–temperature heat source of 140 °C, the further increased power output outweighs the additional costs for further components. The smaller three MWM-cases thus have a lower SIC than the ORC ($SIC_{ORC} = 2675\,€/kW$). Only the largest setup with six heat exchangers, that also reaches the highest annuity, shows an equal SIC of 2676 €/kW. Due to the comparably low component costs of the lower-pressure components, these MWM cases even have lower initial investment costs than most of the other analyzed cycles. The low process pressure not only leads to cheaper pumps, but also reduces the auxiliary power to a range close to 1 kW. Still, as seen for the thermodynamic optimizations, R1233zD(E) seems not to be the ideal fluid and even the best performing case hardly reaches the power output of the ORC (MWM: 72.0 kW, ORC: 72.2 kW). With the higher annuities for the costs (due to the component replacements) and the lower proceeds (reduced operation hours), the total annuity of the MWM Cycle ($A_N = 49\,541\,€$) can still not compete with the ORC ($A_N = 83\,928\,€$).

6.4.3.3 Sensitivity to Economical Reference Conditions

A full sensitivity analysis for the MWM Cycle was well beyond the scope of this work. While for example for the ORC a sweep over evaporation pressure and expansion pressure is only a matter of minutes on a desktop PC, the

search for even one single operation point of the MWM already takes several days on a workstation. The following section therefore only shows some selected variations in order to give at least an idea of the influence of reference conditions on the MWM cycles. The general trends for the sensitivity to the economic reference conditions are summarized in table 6.18 on page 158.

The operation hours seem to be the most important aspect of the economic evaluation. Even for the MWM cycles with the higher power output, the reduced active time inevitably limits the proceeds. Therefore, individual optimizations with adjusted operation hours of the MWM cycle were conducted for 100 °C with R134a. The results for this individual optimization are shown in the last column of table 6.17 on the next page. For comparison, the original 5000 h/a-optimization, as presented in table 6.16, was also evaluated with 5000 h/a, 6000 h/a and 7000 h/a. Even though the operation points of the different optimizations varied, they both showed an almost identical total annuity for the corresponding operation hours within the typical scatter of the genetic algorithm optimizations. It was therefore concluded that the base–case could be used for the evaluation of different operation hours and no individual optimizations were necessary.

Of course the resulting total annuities were highly affected by this variation. Table 6.17 shows the reference ORC, the variations based on the original 5000 h/a-case and the MWM cycle explicitly optimized for 7000 h/a. As expected, when choosing the same base-case, the operation hours only affect the dynamic economic numbers and neither the thermodynamic values nor the static economic numbers change. Increasing the producing time from 5000 h/a to 7000 h/a consequently only leads to a rising annuity of the proceeds and a rising total annuity. In addition, also the dynamic payback time is improved. In contrast, considering the explicit optimization in the last column shows that this longer running setup ended up at a higher power output at the cost of an increased initial investment. In the end, both 7000 h/a-cases yield a high total annuity of 39 579 € (original case) and 40 069 € (longer–running case), respectively. At this rate, the higher initial investment of the MWM finally pays off, and they both outperform the reference ORC by about 20 %. As already known from previous comparisons, the smaller and initially cheaper ORC still results in the better efficiency as rated by the internal rate of return. The

Table 6.17: Results of the MWM Cycle for different operation hours (heat source temperature of 100 °C with R134a).

Cycle		ORC	MWM (optimized for 5000 h/a)			MWM
Operation hours	(h)	7000	5000	6000	7000	7000
Net power	P_{net} (kW)	33.70	41.70	41.70	41.70	42.71
Self consumption	P_{self} (kW)	4.00	3.30	3.30	3.30	3.10
Second law efficiency	η_{II} **(%)**	**30.90**	**38.30**	**38.30**	**38.30**	**39.20**
Evaporators	(-)	1	4	4	4	4
Annuities	$A_{N,C}$ (€)	−8358	−13 321	−13 321	−13 321	−14 114
	$A_{N,O}$ (€)	−14 972	−15 345	−15 345	−15 345	−15 671
	$A_{N,P}$ (€)	55 936	48 746	58 495	68 244	69 855
	A_N **(€)**	**32 606**	**20 080**	**29 830**	**39 579**	**40 069**
Economics	SIC (€/kW)	3266	3573	3573	3573	3691
	IRR (%)	41.80	24.60	32.30	39.70	38.40
	dPBT (a)	2.54	4.22	3.26	2.66	2.75
Initial Investment	K_0 (€)	110 060	149 120	149 120	149 120	157 660

Table 6.18: General sensitivity of the MWM optimizations to the economic reference conditions.

Variation	P_{net}	η_{II}	K_0	SIC	A_N
Operation Hours ↑	↗	↗	↗	→	↑
Refund Rates ↑	↗	↗	→	↓	↑
Suitable Working Fluid ↑	↑	↑	↑	→	↗

break–even between a 7000 h/a–ORC and the MWM lies at around 6300 h/a. A practical implementation has to show if these annual operation hours can be realized with the MWM Cycle.

The refund rates are the second major influence factor on the proceeds. The above cases were all optimized based on the rather optimistic rates for funded geothermal power sales. For comparison, individual optimizations with adjusted rates for self-consumption of the produced power and also for selling the produced power were added for 100 °C with R134a. Again, the results showed that the individually optimized annuities were almost identical to the ones based on the original cases presented in table 6.16. Table 6.19 on the facing page shows the reference ORC and the exemplary MWM cycles with the alternative rates for electricity sales. The variations with the original case are presented in the middle three columns, whereas the individual optimizations are added in the last two columns.

As mentioned, the difference of the total annuity for the original case with adjusted refund rates and the corresponding individual optimization is small. Actually, for both examples, the adjusted original cases were even slightly better. In absolute numbers, the effects on the profitability of the MWM cycles are obvious. The adjusted refund rate for self-consumption ("refund rate" = saving the costs for electrical power, see section 6.1.2) reduces the annuity of the proceeds by about 10 % from 48 746 € to 44 054 €. As the setup of the cycle is not changed, all thermodynamic numbers as well as the initial costs stay the same. Consequently, also the annuities for capital costs 13 321 € and operational costs 15 345 € are identical to the base case. The remaining total annuity then results at 15 389 €. Compared to the initial investment, this leads

Table 6.19: Results of the MWM Cycle for different refund options (heat source temperature of 100 °C with R134a).

Cycle		ORC		MWM (case for Geo rates)			MWM	
Refund Rates		Self	Sell	Geo	Self	Sell	Self	Sell
Net power	P_{net} (kW)	33.70	33.70	41.70	41.70	41.70	42.60	33.80
Self consumption	P_{self} (kW)	4.00	4.00	3.30	3.30	3.30	3.00	3.90
Second law efficiency	η_{II} **(%)**	**30.90**	**30.90**	**38.30**	**38.30**	**38.30**	**39.00**	**31.00**
Evaporators	(-)	1	1	4	4	4	4	4
Annuities	$A_{N,C}$ (€)	−8358	−8358	−13 321	−13 321	−13 321	−14 121	−12 308
	$A_{N,O}$ (€)	−14 972	−14 972	−15 345	−15 345	−15 345	−15 735	−14 799
	$A_{N,P}$ (€)	49 797	16 983	48 746	44 054	15 025	44 921	12 174
	A_N **(€)**	**26 466**	**−6346**	**20 080**	**15 389**	**−13 640**	**15 065**	**−14 933**
Economics	SIC (€/kW)	3266	3266	3573	3573	3573	3691	4170
	IRR (%)	22.50	-	24.60	13.10	-	12.60	-
	dPBT (a)	5.66	∞	4.22	10.90	∞	11.30	∞
Initial Investment	K_0 (€)	110 060	110 060	149 120	149 120	149 120	157 080	141 010

to a lower internal rate of return of only 13.1 % and a longer payback time of over 10 a.

Calculating with the rates for selling the produced electricity leads to an annuity for the proceeds of 15 025 €. Regarding the constant expenses, the total annuity results to be a negative −13 640 €. The used internal rate of return and dynamic payback time are not defined for negative values. The negative value indicates anyway that this setup is not profitable at all compared to an investment at the capital market.

Comparing these numbers to the ORC with its lower initial investment and the longer run–time shows a familiar outcome. For self consumption, the total annuity is higher than for the MWM (26 466 €), but the absolute level is still limited. When selling the electricity, the ORC also ends up with a negative, unprofitable total annuity (−6346 €) due to the reduced proceeds.

The MWM cycle can again only compete with the ORC when a higher annual operation time is assumed. Table 6.20 on the next page shows the comparison of the two concepts, but with 7000 h/a for both cycles. Like in the previous paragraph the MWM then shows a significantly higher total annuity of 33 011 € (+24.7 % over ORC: 26 466 €) as the increased total investment pays off in form of the higher power output. SIC and internal rate of return indicate that the ORC still shows the better economic efficiency and shorter payback time.

The working fluid is the final analyzed influencing factor for the economics of the cycles. In addition to the reference cases, ORC and MWM with R134a, table 6.21 on page 162 shows two more selected fluids: R1234ze(E) and Isobutylene.

The case with R1234ze(E) only marginally differs from the base–case in every aspect. An identical power output at the same initial costs leads to identical total annuities of 20 080 € and 20 598 €, respectively. The feasibility of R1234ze(E) as a replacement fluid for R134a is thereby also confirmed for the economic considerations. It is also expected that R1234ze(E) shows the same behavior as R134a with regard to the other reference conditions like operation hours and refund rates.

Isobutylene, which was already used for all MWM cases at 140 °C, also shows the expected results. The lower vapor pressure reduces the pressure

Table 6.20: Economic results of the MWM Cycle based on self consumption at an operation of 7000 h/a (heat source temperature of 100 °C with R134a).

Cycle		ORC	MWM	MWM
Refund Rates		Self	Self	Self
Fluid		R134a	R134a	Isobut.
Operation hours	(h)	7000	7000	7000
Net power	P_{net} (kW)	33.70	41.70	45.50
Self consumption	P_{self} (kW)	4.00	3.30	2.10
Second law efficiency	η_{II} **(%)**	**30.90**	**38.30**	**41.70**
Evaporators	(-)	1	4	4
Annuities	$A_{N,C}$ (€)	−8358	−13 321	−14 714
	$A_{N,O}$ (€)	−14 972	−15 345	−15 991
	$A_{N,P}$ (€)	49 797	61 676	67 212
	A_N **(€)**	**26 466**	**33 011**	**36 507**
Economics	SIC (€/kW)	3266	3573	3647
	IRR (%)	22.50	21.70	21.67
	dPBT (a)	5.66	5.61	5.61
Initial Investment	K_0 (€)	110 060	149 120	165 830

factor in the cost correlations and allows for a cheaper feed pump. The better thermodynamic performance on the other hand requires higher mass flows and larger equipment. The increased power output of 45.5 kW therefore comes at the costs of an increased initial investment of 165 830 €. In terms of the total annuity, the additional investment pays off as the obtained revenues outweigh the expenses. The highly promising thermodynamic results of Isobutylene (section 6.3.1) can fully be transferred to the economic numbers. The increased second law efficiency of 41.7 % (+8.9 % over R134a) leads to a rise of the total annuity to 22 416 € (+11.6 % over R134a). However, this rise does still not suffice to catch up with the reference–ORC. Again, the limited operation hours of the MWM Cycle restrain its profitability. Without an individual optimization, the previous case was computed again with 7000 h/a. Pitching the annuity of the sales to 74 370 €, the total annuity would rise to

Table 6.21: Optimized results of the MWM Cycle for selected working fluids at a heat source temperature of 100 °C (R134a).

Cycle		ORC	MWM		
Fluid		R134a	R134a	R1234ze(E)	Isobutylene
Net power	P_{net} (kW)	33.70	41.70	42.20	45.50
Self consumption	P_{self} (kW)	4.00	3.30	2.80	2.10
Second law efficiency	η_{II} (%)	**30.90**	**38.30**	**38.70**	**41.70**
Evaporators	(-)	1	4	4	4
Annuities	$A_{N,C}$ (€)	−8358	−13 321	−13 354	−14 714
	$A_{N,O}$ (€)	−14 972	−15 345	−15 371	−15 991
	$A_{N,P}$ (€)	55 936	48 746	48 324	53 121
	A_N (€)	**32 606**	**20 080**	**20 598**	**22 416**
Economics	SIC (€/kW)	3266	3573	3540	3647
	IRR (%)	41.80	24.60	24.90	24.40
	dPBT (a)	2.54	4.22	4.16	4.25
Bare Module Costs	pump (€)	21 964	22 015	21 170	17 633
	expander (€)	45 163	35 566	35 890	39 789
	vessel (€)	-	31 390	32 000	39 809
	condenser (€)	6267	6669	6741	7706
	evaporator (€)	1333	2466	2467	3667
Initial Investment	K_0 (€)	110 060	149 120	149 490	165 830

43 665 € which is about +33.9 % more than the corresponding ORC. As shown in table 6.20, even with the reduced refund rate for self consumption, the absolute numbers of A_N = 36 507 € would be a significant advantage over the ORC from (A_N = 26 466 €, +37.9 %). Still, the feasibility of these operation hours have yet to be proven for the MWM Cycle.

6.4.4 Summary of the Economic Results

Picking up on the thermodynamic assessment of the MWM Cycle in section 6.3.4, the economic numbers show a less favorable picture. The high power output of the MWM Cycle could still be reached at the economically optimized operation points, but the expected limited operation hours for the dynamic cycle drastically reduce the accessible revenues. The MWM Cycle can therefore only top the ORC if comparable operation hours can be realized.

In addition, both cycles struggle with the low exergy content of the low–temperature heat source. If the advantageous refund rates for geothermal power can be used, the profit is satisfactory for both cycles. However, if only the current market price for electricity is available, both ORC and MWM do not reach a positive total balance. Only when the produced power can be used on site, they both end up with a still satisfactory positive final score.

At last, if a durable operation can be realized and a well-suited working fluid is selected, the MWM setup can outperform the benchmark ORC in both thermodynamic (ORC: η_{II} = 30.9 %, MWM: η_{II} = 41.7 %, +40.7 %) and economic results (ORC: A_N = 26 466 €, MWM: A_N = 36 507 €, +37.9 %).

Chapter 7

Summary and Recommendations

In this work, the MWM Cycle was analyzed and evaluated by means of a specifically developed dynamic simulation model. The gained understanding contributes to the current state of knowledge in the field of low temperature heat source utilization and fills the research gap of a *realizable* power cycle for *very low to low temperatures*.

7.1 Summary

The thermodynamically limited usability of low–temperature heat sources requires advanced power cycles in order to reach acceptable efficiencies. All known concepts aim to combine a maximized heat source utilization with a high internal conversion efficiency of heat to power. In addition to the thermodynamic challenges, a profitable concept depends on its feasibility and the availability of the needed components.

Cycle Analysis In contrast to most other advanced cycles, the MWM Cycle provides both a promising performance and an implementation with commercially available parts. The batch evaporation within simple plate heat exchangers leads to a gradually increasing boiling temperature of the working fluid. By the implementation of at least three evaporators, their shifted batch operation can provide a working fluid stream for the continuous operation of expansion engine, condenser and feed pump. When routing the heat source

stream through all evaporators in a cascaded manner, an almost perfect temperature match with the working fluid is obtained. This reduces internal losses and allows for very high second law efficiencies. The gained working fluid vapor can, without the need for a two–phase expander, directly be expanded in an expansion engine. The major challenge with the MWM Cycle, however, is the process control of the transient operation: the duration of the batch phases define the achievable pressure levels and the obtained power output.

Simulation Model The custom dynamic MATLAB model was designed to map the major features of the MWM Cycle. The batch evaporation and pool boiling of the working fluid, the flow of the heat source medium, as well as the heat transfer and total energy balances within each evaporator are handled by an inner layer of the model. An intermediate layer controls the process sequence, the interaction of the heat exchangers and the continuous parts like expansion engine and condenser. In order to initially find the perfect combination of the process parameters (dimensions, mass flows, heat transfer…) for specific reference conditions, an optional outer layer with a genetic algorithm optimization was added. The economic performance of the optimized cycles was rated by dynamic methods for the absolute profitability (annuity method) and for the economic efficiency (internal rate of return and dynamic payback time).

Thermodynamic Performance Based on the simulation results, it could be shown that a thermodynamically optimized MWM setup shows a major advantage over a common ORC in terms of net power output and second law efficiency at all investigated conditions.

The greatest advantage of the MWM cycle could be observed at 100 °C due to the lack of a well suited working fluid for the ORC. With the benchmark fluid R134a, the second law efficiency of the MWM Cycle outperformed the ORC by about 39 % (ORC: $\eta_{II} = 30.9\,\%$, MWM: $\eta_{II} = 42.9\,\%$). A MWM setup with Isobutylene was even 49 % better than the ORC. With regard to ecological aspects, the feasibility of the environmentally recommended "replacement–fluid" R1234ze(E) could also be confirmed for both the ORC and the MWM Cycle.

Only at higher temperature levels could other fluids further improve the

ORC-efficiency. As widely recommended by literature for 120 °C, R227ea led to a good performance of the ORC and results in a second law efficiency of $\eta_{II} = 40.4\,\%$. The advantage of the most suitable MWM case shrunk to 16 % (R1233zD: $\eta_{II} = 44.6\,\%$). For the highest analyzed heat source temperature of 140 °C, the further improvement of matching working fluids allowed the ORC to almost catch up with the MWM and the advantage dropped to 11 % (ORC: $\eta_{II} = 46.4\,\%$, MWM:$\eta_{II} = 51.6\,\%$).

Economic Performance For all ORC cases, the optimized thermodynamic and economic operation points were identical. For the MWM Cycle, the optimized economic setups differed from their thermodynamic counterparts. Especially the number of evaporators and the size of the pressure vessels were reduced by the optimization once their costs were taken into account.

In direct comparison, as summarized in table 7.1 on the next page, the results showed that even the "economic" MWM variants still had a thermodynamic advantage over the benchmark ORC. However, with the assumed reduced operation hours of the MWM Cycle (increased maintenance), the higher net power output could not compensate its higher investment costs. Consequently, the benchmark ORC showed higher annuities, higher internal rates of return and a shorter payback time for all heat source temperatures.

By increasing the operation hours, the MWM Cycle at 100 °C could compete with the ORC. Assuming the same period for both cycles, the higher investment of the MWM pays off and the higher power output leads to a 21 % better total annuity (ORC: 33 000 €, MWM: 40 000 €). The ORC shows the better economic efficiency (internal rate of return and payback time), but could not provide the same total net present value at the end of the observation time.

In accordance with the major share of literature on this topic, the initial economic evaluations were calculated with the feed-in tariff for geothermal power sales according to the Renewable Energy Sources Act. While these high refund rates are attractive for large–scale geothermal plants, the smaller MWM modules can most probably not cover the enormous costs for exploration and drilling. Therefore, both ORC and MWM were also evaluated with the reduced rates for self consumption (savings from reducing the purchased electricity) and selling at the electricity market. While the cases with self consumption still resulted in moderately positive results, the comparatively low rates at

Table 7.1: Summary of selected economic results of ORC and MWM Cycle.

Cycle	T_{HS} (°C)	HX (-)	Rate (-)	Fluid (-)	Hours (h)	P_{net} (kW)	η_{II} (%)	A_N (€)	IRR (%)
Reference:									
ORC	100	1	Geo	R134a	7000	33.7	30.9	32 606	41.8
MWM	100	4	Geo	R134a	5000	41.7	38.3	20 080	24.6
Variations:									
ORC	100	1	Geo	**R1234**	7000	33.1	30.4	**32 236**	43.0
ORC	100	1	Geo	**Isobut.**	7000	30.9	28.3	29 940	**44.6**
MWM	100	**3**	Geo	R134a	5000	38.1	35.0	17 116	23.5
MWM	100	**5**	Geo	R134a	5000	42.1	38.6	19 529	23.1
MWM	100	4	Geo	**R1234**	5000	42.2	38.7	20 598	24.9
MWM	100	4	Geo	**Isobut.**	5000	**45.5**	41.7	22 416	24.4
MWM	100	4	Geo	R134a	**6000**	41.7	38.3	29 830	32.2
MWM	100	4	Geo	R134a	**7000**	41.7	38.3	**39 579**	39.7
ORC	100	1	**self**	R134a	7000	33.7	30.9	26 466	22.5
ORC	100	1	**sell**	R134a	7000	33.7	30.9	−6346	-
MWM	100	4	**self**	R134a	5000	41.7	38.3	15 389	13.1
MWM	100	4	**sell**	R134a	5000	41.7	38.3	−13 640	-
MWM	100	4	**self**	R134a	**7000**	41.7	38.3	33 011	21.7
MWM	100	4	**self**	**Isobut.**	**7000**	**45.5**	41.7	**36 507**	21.7
ORC	**120**	1	Geo	R134a	7000	51.2	38.5	**55 391**	50.1
ORC	**120**	1	Geo	**R1234**	7000	49.6	37.2	53 795	51.9
ORC	**120**	1	Geo	**Isobut.**	7000	44.8	33.7	48 971	**54.2**
MWM	**120**	4	Geo	R134a	5000	52.1	39.2	25 788	22.0
MWM	**120**	**5**	Geo	R134a	5000	**55.7**	41.9	26 599	20.4
ORC	**140**	1	Geo	R134a	7000	72.2	46.4	83 298	57.0
ORC	**140**	1	Geo	**R1234**	7000	**72.2**	46.7	**85 341**	59.2
ORC	**140**	1	Geo	**Isobut.**	7000	60.2	38.7	69 940	**61.5**
MWM	**140**	4	Geo	**R1233**	5000	66.9	43.0	46 426	41.7
MWM	**140**	**6**	Geo	**R1233**	5000	72.0	46.3	49 541	38.5

the electricity market led to unprofitable, negative annuities for both ORC and MWM Cycle. For the self consumption, the MWM Cycle can again only compete with the ORC with the higher operation hours, but then reaches a 25 % higher value (ORC: 26 500 €, MWM: 33 000 €).

The most promising working fluids from the thermodynamic optimization were again evaluated with regard to the economics. For both ORC and MWM Cycle, the best performing working fluids from the thermodynamic optimization also led to the best economic numbers. Assuming increased operation hours and the refund rates for self consumption, the MWM Cycle with Isobutylene could gain an advantage of 38 % over the ORC at 100 °C (ORC: 26 500 €, MWM: 36 500 €).

With a given geothermal heat source at a temperature of 100 °C, three typical strategic investment decisions might be:

- An investor with the focus on a fast and efficient return of the investment would go for an ORC with Isobutylene as working fluid. Even though the power output is limited, the reduced initial costs lead to a high-performing internal rate of return and a short payback time.
- A conservative investor with the focus on a maximal long–term monetary return would go for the ORC with R134a or, more ecological, with R1234ze(E). While the IRR is lower than for Isobutylene, the total annuity is the highest one of the conservative options (ORC or MWM Cycle with limited operation hours) for 100 °C.
- A risk–oriented investor would chose the MWM Cycle with R134a and expect operational hours of nearly 7000 h/a. Even though the initial investment of the MWM Cycle is high and the IRR is lower, the high power output would allow for the highest net present value from this given heat source at the end of the observation time.

The decisions for a non-geothermal heat source and self-consumption would be based on the same influence factors: The ORC shows the better short-term performance and cost efficiency while the MWM Cycle, assuming adequate operation hours, provides the higher net present values.

Even though these numbers and options look quite promising, both cycles struggle with the rather small absolute power output. At these low temperatures, the first law efficiency is thermodynamically limited to about 5 %. Even when the heat source is free of charge (like waste heat), the exemplary 50 kW power output from a 1 MW heat source can hardly cover any investment costs

at the current low electricity prices. The funded rates for geothermal power are mostly only attractive for large scale projects. So for small scale plants, selling the heat instead of the electricity is often the more promising approach. Distributing the top 50 % of the 1 MW heat source[1] to district heating at a typical price of 0.06 €/kWh to 0.09 €/kWh [107] would easily exceed the proceeds from 50 kW electricity sales. While this business depends on the seasonal demand for heat and the costly heating infrastructure, the low risk and the solid cash flow will often make it more attractive to investors than a risky, innovative power cycle.

In conclusion, the results showed that small scale waste heat recovery is, at this time, almost only profitable if electricity is needed on-site and that the distribution of small scale installations in the industry are slowed down due to the missing monetary incentives.

7.2 Contribution

With regard to the defined objectives, this work contributes to a deeper understanding of the MWM Cycle and a theoretical basis for further analysis. The stationary and the transient sub-processes were visualized side-by-side in specifically adapted temperature–heat– and temperature–entropy–diagrams. Based on these theoretical fundamentals, the originally proposed setup was improved by a cascaded heat source flow for a better temperature match and an unheated discharge phase in order to compensate the negative effects of thermal inertia on the dynamic cycle.

The developed simulation model covers all relevant effects of the MWM Cycle. Besides the typical features of power cycle models (heat transfer coefficients, discretization schemes and solvers), the model also included the thermal inertia of the wall material and heat source medium to especially take the dynamic behavior of the cycle into account.

The results of the simulation model were used to rate the MWM Cycle against a benchmark ORC with regard to its thermodynamic and economic performance. In addition to a default set of reference conditions, selected properties like working fluid, possible operation time and different refund rates were varied in order to give a comprehensive idea of the cycle's behavior.

[1] Using the range from 100 °C to 60 °C gives about 530 kW of heat.

7.3 Outlook

By giving many answers to the topic of low temperature cycles and especially the MWM Cycle, this work provides a basis to be considered by further research.

- It would be advantageous to build a test rig of the MWW Cycle including the findings from this work. This pilot plant could provide further insights about the feasibility of the control of the dynamic cycle. In addition, it should be used to analyze the process of pool boiling in plate heat exchangers and to validate the estimated heat transfer coefficients.
- Based on this test rig, the cost correlations of the pressure vessels, the custom expansion engine and the pump could be checked against the real costs. Based on this data, the correlations might be refined if necessary and the dependency of the volume flow could be added. If, for example, the actual costs for the pressure vessels were smaller, the economics of the MWM Cycle would be considerably boosted. The experience from the operation of the test plant will also allow for a better estimation of the achievable operational hours.
- The initial sensitivity analysis of the MWM Cycle in this work can be a basis for extensive analysis including further working fluids and different scenarios for the trend of energy costs and refund rates.
- In extension to the here discussed stationary heat sources, first results indicated an advantage with regard to dynamic heat sources. With its several independent process parameters, which can even be adjusted online, the MWM Cycle seems to be better suited for an off-design behavior than the ORC.

Bibliography

[1] Umweltbundesamt, ed. *Europäische Energie- und Klimaziele*. 2019. URL: https://www.umweltbundesamt.de/daten/klima/europaeische-energie-klimaziele (visited on May 21, 2020).

[2] S. Lecompte, H. Huisseune, van den Broek, M., and M. de Paepe. "Methodical thermodynamic analysis and regression models of organic Rankine cycle architectures for waste heat recovery". In: *Energy* 87 (2015), pp. 60–76. ISSN: 03605442. DOI: 10.1016/j.energy.2015.04.094.

[3] F. Campana, M. Bianchi, L. Branchini, A. de Pascale, A. Peretto, M. Baresi, A. Fermi, N. Rossetti, and R. Vescovo. "ORC waste heat recovery in European energy intensive industries. Energy and GHG savings". In: *Energy Conversion and Management* 76 (2013), pp. 244–252. ISSN: 01968904. DOI: 10.1016/j.enconman.2013.07.041.

[4] Owen Bailey and Ernst Worrell. *Clean Energy Technologies: A Preliminary Inventory of the Potential for Electricity Generation*. Ed. by Lawrence Berkeley National Laboratory. 2005. URL: https://escholarship.org/uc/item/3418w4kv (visited on Feb. 17, 2017).

[5] Umweltbundesamt, ed. *Treibhausgas-Emissionen in der Europäischen Union*. 2019. URL: https://www.umweltbundesamt.de/daten/klima/treibhausgas-emissionen-in-der-europaeischen-union#gase (visited on May 21, 2020).

[6] Sylvain Quoilin, Martijn Den van Broek, Sébastien Declaye, Pierre Dewallef, and Vincent Lemort. "Techno-economic survey of Organic Rankine Cycle (ORC) systems". In: *Renewable and Sustainable Energy Reviews* 22 (2013), pp. 168–186. ISSN: 13640321. DOI: 10.1016/j.rser.2013.01.028.

[7] Herbert Paschen, Dagmar Oertel, and Reinhard Grünwald. *Möglichkeiten geothermischer Stromerzeugung in Deutschland*. TAB Arbeitsbericht, 2003. URL: https://www.tab-beim-bundestag.de/de/pdf/publikationen/berichte/TAB-Arbeitsbericht-ab084.pdf.

[8] S. Eyerer, C. Schifflechner, S. Hofbauer, W. Bauer, C. Wieland, and H. Spliethoff. "Combined heat and power from hydrothermal geothermal resources in Germany: An assessment of the potential". In: *Renewable and Sustainable Energy Reviews* 120 (2020), p. 109661. ISSN: 13640321. DOI: 10.1016/j.rser.2019.109661.

[9] A. I. Kalina. "Combined-Cycle System With Novel Bottoming Cycle". In: *Journal of Engineering for Gas Turbines and Power* 106 (4 1984), p. 737. ISSN: 07424795. DOI: 10.1115/1.3239632.

[10] A. Schuster, S. Karellas, and R. Aumann. "Efficiency optimization potential in supercritical Organic Rankine Cycles". In: *Energy* 35 (2 2010), pp. 1033–1039. ISSN: 03605442. DOI: 10.1016/j.energy.2009.06.019.

[11] Johann Fischer. "Comparison of trilateral cycles and organic Rankine cycles". In: *Energy* 36 (10 2011), pp. 6208–6219. ISSN: 03605442. DOI: 10.1016/j.energy.2011.07.041.

[12] Tony Ho, Samuel S. Mao, and Ralph Greif. "Comparison of the Organic Flash Cycle (OFC) to other advanced vapor cycles for intermediate and high temperature waste heat reclamation and solar thermal energy". In: *Energy* 42 (1 2012), pp. 213–223. ISSN: 03605442. DOI: 10.1016/j.energy.2012.03.067.

[13] M. Bianchi and A. de Pascale. "Bottoming cycles for electric energy generation. Parametric investigation of available and innovative solutions for the exploitation of low and medium temperature heat sources". In: *Applied Energy* 88 (5 2011), pp. 1500–1509. ISSN: 03062619. DOI: 10.1016/j.apenergy.2010.11.013.

[14] Yiping Dai, Jiangfeng Wang, and Lin Gao. "Parametric optimization and comparative study of organic Rankine cycle (ORC) for low grade waste heat recovery". In: *Energy Conversion and Management* 50 (3 2009), pp. 576–582. ISSN: 01968904. DOI: 10.1016/j.enconman.2008.10.018.

[15] Ronald DiPippo. “Second Law assessment of binary plants generating power from low-temperature geothermal fluids”. In: *Geothermics* 33 (5 2004), pp. 565–586. ISSN: 03756505. DOI: 10.1016/j.geothermics.2003.10.003.

[16] Emanuel Feru, Bram de Jager, Frank Willems, and Maarten Steinbuch. “Two-phase plate-fin heat exchanger modeling for waste heat recovery systems in diesel engines”. In: *Applied Energy* 133 (2014), pp. 183–196. ISSN: 03062619. DOI: 10.1016/j.apenergy.2014.07.073.

[17] J. G. Andreasen, U. Larsen, T. Knudsen, L. Pierobon, and F. Haglind. “Selection and optimization of pure and mixed working fluids for low grade heat utilization using organic Rankine cycles”. In: *Energy* 73 (2014), pp. 204–213. ISSN: 03605442. DOI: 10.1016/j.energy.2014.06.012.

[18] Florian Heberle and Dieter Brüggemann. “Thermo-Economic Evaluation of Organic Rankine Cycles for Geothermal Power Generation Using Zeotropic Mixtures”. In: *Energies* 8 (3 2015), pp. 2097–2124. ISSN: 1996-1073. DOI: 10.3390/en8032097.

[19] Markus Preißinger, Florian Heberle, and Dieter Brüggemann. “Advanced Organic Rankine Cycle for geothermal application”. In: *International Journal of Low-Carbon Technologies* 8 (suppl 1 2013), pp. i62–i68. ISSN: 1748-1317. DOI: 10.1093/ijlct/ctt021.

[20] P. J. Mago, K. K. Srinivasan, L. M. Chamra, and C. Somayaji. “An examination of exergy destruction in organic Rankine cycles”. In: *International Journal of Energy Research* 32 (10 2008), pp. 926–938. ISSN: 0363907X. DOI: 10.1002/er.1406.

[21] Tony Ho, Samuel S. Mao, and Ralph Greif. “Increased power production through enhancements to the Organic Flash Cycle (OFC)”. In: *Energy* 45 (1 2012), pp. 686–695. ISSN: 03605442. DOI: 10.1016/j.energy.2012.07.023.

[22] M. Yari, A. S. Mehr, V. Zare, S.M.S. Mahmoudi, and M. A. Rosen. “Exergoeconomic comparison of TLC (trilateral Rankine cycle), ORC (organic Rankine cycle) and Kalina cycle using a low grade heat source”. In: *Energy* 83 (2015), pp. 712–722. ISSN: 03605442. DOI: 10.1016/j.energy.2015.02.080.

[23] Hans Dieter Baehr and Stephan Kabelac. *Thermodynamik. Grundlagen und technische Anwendungen.* 14. Aufl. Springer-Lehrbuch. Berlin, Heidelberg: Springer-Verlag Berlin Heidelberg, 2009. 1 online resource (xix, 667. ISBN: 978-3-642-00555-8.

[24] Sylvain Quoilin, Sébastien Declaye, Bertrand F. Tchanche, and Vincent Lemort. "Thermo-economic optimization of waste heat recovery Organic Rankine Cycles". In: *Applied Thermal Engineering* 31 (14-15 2011), pp. 2885–2893. ISSN: 13594311. DOI: 10.1016/j.applthermaleng.2011.05.014.

[25] Wei Liu, Dominik Meinel, Moritz Gleinser, Christoph Wieland, and Hartmut Spliethoff. "Optimal Heat Source Temperature for thermodynamic optimization of sub-critical Organic Rankine Cycles". In: *Energy* 88 (2015), pp. 897–906. ISSN: 03605442. DOI: 10.1016/j.energy.2015.07.040.

[26] M. Chys, van den Broek, M., B. Vanslambrouck, and M. de Paepe. "Potential of zeotropic mixtures as working fluids in organic Rankine cycles". In: *Energy* 44 (1 2012), pp. 623–632. ISSN: 03605442. DOI: 10.1016/j.energy.2012.05.030.

[27] Huijuan Chen, D. Yogi Goswami, and Elias K. Stefanakos. "A review of thermodynamic cycles and working fluids for the conversion of low-grade heat". In: *Renewable and Sustainable Energy Reviews* 14 (9 2010), pp. 3059–3067. ISSN: 13640321. DOI: 10.1016/j.rser.2010.07.006.

[28] Chao He, Chao Liu, Hong Gao, Hui Xie, Yourong Li, Shuangying Wu, and Jinliang Xu. "The optimal evaporation temperature and working fluids for subcritical organic Rankine cycle". In: *Energy* 38 (1 2012), pp. 136–143. ISSN: 03605442. DOI: 10.1016/j.energy.2011.12.022.

[29] Sebastian Eyerer, Peter Eyerer, Markus Eicheldinger, Beatrice Tübke, Christoph Wieland, and Hartmut Spliethoff. "Theoretical analysis and experimental investigation of material compatibility between refrigerants and polymers". In: *Energy* 163 (2018), pp. 782–799. ISSN: 03605442. DOI: 10.1016/j.energy.2018.08.142.

[30] Junhyun Cho, Munkyoung Choi, Young-Jin Baik, Gilbong Lee, Ho-Sang Ra, Byunghui Kim, and Minsung Kim. "Development of the turbomachinery for the supercritical carbon dioxide power cycle". In: *International Journal of Energy Research* 40 (5 2016), pp. 587–599. ISSN: 0363907X. DOI: 10.1002/er.3453.

[31] Sotirios Karellas, Andreas Schuster, and Aris-Dimitrios Leontaritis. "Influence of supercritical ORC parameters on plate heat exchanger design". In: *Applied Thermal Engineering* 33-34 (2012), pp. 70–76. ISSN: 13594311. DOI: 10.1016/j.applthermaleng.2011.09.013.

[32] Oyeniyi A. Oyewunmi, Simó Ferré-Serres, Steven Lecompte, Martijn van den Broek, Michel de Paepe, and Christos N. Markides. "An Assessment of Subcritical and Trans-critical Organic Rankine Cycles for Waste-heat Recovery". In: *Energy Procedia* 105 (2017), pp. 1870–1876. ISSN: 18766102. DOI: 10.1016/j.egypro.2017.03.548.

[33] Anish Modi and Fredrik Haglind. "Performance analysis of a Kalina cycle for a central receiver solar thermal power plant with direct steam generation". In: *Applied Thermal Engineering* 65 (1-2 2014), pp. 201–208. ISSN: 13594311. DOI: 10.1016/j.applthermaleng.2014.01.010.

[34] Jiangfeng Wang, Yiping Dai, and Lin Gao. "Exergy analyses and parametric optimizations for different cogeneration power plants in cement industry". In: *Applied Energy* 86 (6 2009), pp. 941–948. ISSN: 03062619. DOI: 10.1016/j.apenergy.2008.09.001.

[35] Geothermie Unterhaching GmbH & Co KG. *Daten & Fakten: Geothermie Unterhaching*. 2017. URL: https://www.geothermie-unterhaching.de/cms/geothermie/web.nsf/id/pa_daten_fakten.html (visited on June 10, 2018).

[36] Marc Schreib. "Pilotprojekt gescheitert. Das Kalina-Kraftwerk der Geothermie Unterhaching soll stillgelegt werden. Einst war die Anlage ein Leuchtturm-Projekt. Nun ist Schluss." In: *Münchner Merkur* 2017 (Dec. 12, 2017). URL: https://www.merkur.de/lokales/muenchen-lk/unterhaching-ort29619/kalina-kraftwerk-in-unterhaching-wird-stillgelegt-9444051.html#idAnchComments (visited on June 10, 2018).

[37] Florian Heberle, Markus Preißinger, and Dieter Brüggemann. "Zeotropic mixtures as working fluids in Organic Rankine Cycles for low-enthalpy geothermal resources". In: *Renewable Energy* 37 (1 2012), pp. 364–370. ISSN: 09601481. DOI: 10.1016/j.renene.2011.06.044.

[38] Ngoc Anh Lai and Johann Fischer. "Efficiencies of power flash cycles". In: *Energy* 44 (1 2012), pp. 1017–1027. ISSN: 03605442. DOI: 10.1016/j.energy.2012.04.046.

[39] Hiroshi Kanno and Naoki Shikazono. "Experimental and modeling study on adiabatic two-phase expansion in a cylinder". In: *International Journal of Heat and Mass Transfer* 86 (2015), pp. 755–763. ISSN: 00179310. DOI: 10.1016/j.ijheatmasstransfer.2015.02.059.

[40] Michael Steffen, Michael Löffler, and Karlheinz Schaber. "Efficiency of a new Triangle Cycle with flash evaporation in a piston engine". In: *Energy* 57 (2013), pp. 295–307. ISSN: 03605442. DOI: 10.1016/j.energy.2012.11.054.

[41] Michael Löffler. "Batch Processes in Heat Engines". In: *Energy* 125 (2017), pp. 788–794. ISSN: 03605442. DOI: 10.1016/j.energy.2017.02.105.

[42] Jürgen Misselhorn. "Wärmekraftmaschine". Schutzrecht DE 10 2008 023 793 A1 (Deutschland). Maschinenwerke Misselhorn GmbH, 80336 München, DE. Dec. 3, 2009.

[43] Manfred Moullion. "Anlage und Verfahren zur Rückgewinnung von Energie aus Wärme in einem thermodynamischen Kreisprozess". Schutzrecht DE 10 2013 009 351 B3 (Deutschland). Maschinenwerk Misselhorn GmbH - MWM. Jan. 16, 2014.

[44] Thomas Hutzschenreuter. *Allgemeine Betriebswirtschaftslehre. Grundlagen mit zahlreichen Praxisbeispielen*. ger. 6., überarb. Aufl. Lehrbuch. Hutzschenreuter, Thomas (author.) Wiesbaden: Springer Gabler, 2015. 517 pp. ISBN: 978-3-658-08564-3. DOI: 10.1007/978-3-658-08564-3.

[45] Verein Deutscher Ingenieure. *Wirtschaftlichkeit gebäudetechnischer Anlagen: Grundlagen und Kostenberechnung*. VDI 2067. Sept. 1, 2012. 45 pp.

[46] Pascal Schlagermann. “Exergoökonomische Analyse geothermischer Strombereitstellung am Beispiel des Oberrheingrabens”. Lehrstuhl für Energiesysteme. Dissertation. München: Technische Universität München, 2014. 276 pp.

[47] Richard Turton. *Analysis, synthesis, and design of chemical processes*. 4th ed. Prentice Hall international series in the physical and chemical engineering sciences. Upper Saddle River, NJ: Prentice Hall, 2012. 228 pp. ISBN: 978-0-13-261872-4.

[48] Adrian Bejan, George Tsatsaronis, and Michael J. Moran. *Thermal design and optimization*. A Wiley-Interscience publication. New York: Wiley, 1996. 542 pp. ISBN: 978-0-471-58467-4.

[49] Kenneth M. Guthrie. *Process plant estimating evaluation and control*. Solana Beach, Calif.: Craftsman, 1974. 604 s. ISBN: 9780910460224.

[50] Alexander Buttler, Julia Hentschel, Steffen Kahlert, and Michael Angerer. *Statusbericht Flexibilitätsbedarf im Stromsektor. Eine Analyse der aktuellen marktwirtschaftlichen und technischen Herausforderungen an Speicher und Kraftwerke im Zuge der Energiewende*. Ed. by Technische Universität München - Lehrstuhl für Energiesysteme. 2015. URL: https://www.es.mw.tum.de/fileadmin/w00bhq/www/pdf/Statusbericht_Flexibilitaetsbedarf_2014_Final.pdf (visited on Dec. 7, 2017).

[51] Joachim Nitsch et al. *Langfristszenarien und Strategien für den Ausbau der erneuerbaren Energien in Deutschland bei Berücksichtigung der Entwicklung in Europa und global*. BMU - FKZ 03MAP146. Ed. by Bundesumweltminsterium. 2012. URL: http://elib.dlr.de/76043/ (visited on Dec. 7, 2017).

[52] Sylvain Quoilin, Richard Aumann, Andreas Grill, Andreas Schuster, Vincent Lemort, and Hartmut Spliethoff. “Dynamic modeling and optimal control strategy of waste heat recovery Organic Rankine Cycles”. In: *Applied Energy* 88 (6 2011), pp. 2183–2190. ISSN: 03062619. DOI: 10.1016/j.apenergy.2011.01.015.

[53] Valentina Orlandini, Leonardo Pierobon, Signe Schløer, Andrea de Pascale, and Fredrik Haglind. “Dynamic performance of a novel offshore power system integrated with a wind farm”. In: *Energy* 109 (2016), pp. 236–247. ISSN: 03605442. DOI: 10.1016/j.energy.2016.04.073.

[54] Jakob Munch Jensen. "Dynamic Modeling of Thermo-Fluid Systems. With Focus on Evaporators for Refrigeration". Department of Mechanical Engineering. Dissertation. Lyngby: Technical University of Denmark, 2003. 215 pp.

[55] Moritz Gleinser, Christoph Wieland, and Hartmut Spliethoff. "Batch evaporation power cycle. Influence of thermal inertia and residence time". In: *Energy* 157 (2018), pp. 1090–1101. ISSN: 03605442. DOI: 10.1016/j.energy.2018.05.145.

[56] Ian H. Bell, Sylvain Quoilin, Emeline Georges, James E. Braun, Eckhard A. Groll, W. Travis Horton, and Vincent Lemort. "A generalized moving-boundary algorithm to predict the heat transfer rate of counterflow heat exchangers for any phase configuration". In: *Applied Thermal Engineering* 79 (2015), pp. 192–201. ISSN: 13594311. DOI: 10.1016/j.applthermaleng.2014.12.028.

[57] Daijin Li, Kai Luo, and Jianjun Dang. "A moving boundary model for two-phase flow heat exchanger incorporated with relative velocities between boundaries and fluid". In: *International Journal of Heat and Mass Transfer* 95 (2016), pp. 35–44. ISSN: 00179310. DOI: 10.1016/j.ijheatmasstransfer.2015.11.095.

[58] Valerio Lo Brano, Giuseppina Ciulla, Antonio Piacentino, and Fabio Cardona. "Finite difference thermal model of a latent heat storage system coupled with a photovoltaic device. Description and experimental validation". In: *Renewable Energy* 68 (2014), pp. 181–193. ISSN: 09601481. DOI: 10.1016/j.renene.2014.01.043.

[59] G. D. Mandrusiak and V. P. Carey. "A finite difference computational model of annular film-flow boiling and two-phase flow in vertical channels with offset strip fins". In: *International Journal of Multiphase Flow* 16 (6 1990), pp. 1071–1096. ISSN: 03019322. DOI: 10.1016/0301-9322(90)90107-T.

[60] Adriano Desideri, Andres Hernandez, Sergei Gusev, Martijn van den Broek, Vincent Lemort, and Sylvain Quoilin. "Steady-state and dynamic validation of a small-scale waste heat recovery system using the ThermoCycle Modelica library". In: *Energy* 115 (2016), pp. 684–696. ISSN: 03605442. DOI: 10.1016/j.energy.2016.09.004.

[61] Sylvain Quoilin, Ian Bell, Adriano Desideri, Pierre Dewallef, and Vincent Lemort. “Methods to Increase the Robustness of Finite-Volume Flow Models in Thermodynamic Systems”. In: *Energies* 7 (3 2014), pp. 1621–1640. ISSN: 1996-1073. DOI: 10.3390/en7031621.

[62] J.W. MacArthur and E.W. Grald. “Unsteady compressible two-phase flow model for predicting cyclic heat pump performance and a comparison with experimental data”. In: *International Journal of Refrigeration* 12 (1 1989), pp. 29–41. ISSN: 01407007. DOI: 10.1016/0140-7007(89)90009-1.

[63] Satyam Bendapudi, James E. Braun, and Eckhard A. Groll. “A comparison of moving-boundary and finite-volume formulations for transients in centrifugal chillers”. In: *International Journal of Refrigeration* 31 (8 2008), pp. 1437–1452. ISSN: 01407007. DOI: 10.1016/j.ijrefrig.2008.03.006.

[64] William H. Press. *Numerical recipes. The art of scientific computing*. Cambridge [Cambridgeshire] and New York: Cambridge University Press, 1986. xx, 818. ISBN: 0521308119.

[65] David E. Goldberg. *Genetic algorithms in search, optimization, and machine learning*. 30. print. Addison-Wesley series in artificial intelligence. Boston: Addison-Wesley, 2012. 412 pp. ISBN: 978-0201157673.

[66] Christoph Wieland, Moritz Gleinser, Hartmut Spliethoff, and Manfred Moullion. “Anordnung mit mehreren Wärmeübertragern und Verfahren zur Verdampfung eines Arbeitsmediums”. Schutzrecht DE 10 2014 006 909 B3. Maschinenwerk Misselhorn MWM GmbH, 80992 München and Technische Universität München, 8033 München. July 9, 2015.

[67] Jürgen Misselhorn and Christian Freese. “Wärmetauscher”. Schutzrecht DE 10 2011 108 094 A1 (Deutschland). Maschinenwerk Misselhorn GmbH. Jan. 24, 2013.

[68] Osamu Miyatake, Kentaro Murakami, Yoichi Kawata, and Tetsu Fujii. “FUNDAMENTAL EXPERIMENTS WITH FLASH EVAPORATION.” In: *Heat Transfer - Japanese Research* 2 (4 1973), pp. 89–100.

[69] Osamu Miyatake, Tetsu Fujii, Toshiaki Tanaka, and Tsutomu Nakaoka. “FLASH EVAPORATION PHENOMENA OF POOL WATER”. In: *Heat Transfer - Japanese Research* 6 (2 1977), pp. 13–24.

[70] Jong-Il Kim and Noam Lior. “Some critical transitions in pool flash evaporation”. In: *International Journal of Heat and Mass Transfer* 40 (10 1997), pp. 2363–2372. ISSN: 00179310. DOI: 10.1016/S0017-9310(96)00296-7.

[71] D. Saury, S. Harmand, and M. Siroux. “Flash evaporation from a water pool. Influence of the liquid height and of the depressurization rate”. In: *International Journal of Thermal Sciences* 44 (10 2005), pp. 953–965. ISSN: 12900729. DOI: 10.1016/j.ijthermalsci.2005.03.005.

[72] E. W. Lemmon, M. L. Huber, and M. O. McLinden. *NIST Standard Reference Database 23: Reference Fluid Thermodynamic and Transport Properties-REFPROP*. Standard Reference Data Program. Version 9.1. Gaithersburg, USA: National Institute of Standards and Technology, 2013.

[73] Wolfgang Polifke and Jan Kopitz. *Wärmeübertragung. Grundlagen, analytische und numerische Methoden*. Maschinenbau : Wärmeübertragung. München and Boston [u.a.]: Pearson Studium, 2005. 492 S. ISBN: 9783827371041.

[74] Rudi Marek and Klaus Nitsche. *Praxis der Wärmeübertragung. Grundlagen - Anwendungen - Übungsaufgaben*. 3., aktualisierte Auflage. München: Fachbuchverl. Leipzig im Hanser Verl., 2012. 343 S. ISBN: 978-3-446-43241-3.

[75] Holger Martin. “A theoretical approach to predict the performance of chevron-type plate heat exchangers”. In: *Chemical Engineering and Processing: Process Intensification* 35 (4 1996), pp. 301–310. ISSN: 02552701. DOI: 10.1016/0255-2701(95)04129-X.

[76] MathWorks. *Population Diversity. Custom Plot Function and Linear Constraints in ga*. 2019. URL: https://de.mathworks.com/help/gads/population-diversity.html (visited on May 6, 2019).

[77] R. K. Shah and Dušan P. Sekulić. *Fundamentals of heat exchanger design*. Hoboken, NJ: John Wiley & Sons, 2003. 1 online resource (xxxii, 941. ISBN: 0-471-32171-0.

[78] Warren Max Rohsenow. *A method of correlating heat transfer data for surface boiling of liquids*. Massachusetts: MIT, 1951. URL: http://hdl.handle.net/1721.1/61431 (visited on Jan. 28, 2016).

[79] Warren Max Rohsenow. “A method of correlating heat transfer data for surface boiling of liquids”. In: *Trans. ASME* 74 (1952), p. 969.

[80] R. A. Smith. *Vaporisers. Selection, design & operation.* Harlow, Essex, and England, New York: Longman Scientific & Technical and Wiley, 1986. xviii, 341. ISBN: 0470207094.

[81] Stuart W. Churchill and Humbert H.S. Chu. “Correlating equations for laminar and turbulent free convection from a vertical plate”. In: *International Journal of Heat and Mass Transfer* 18 (11 1975), pp. 1323–1329. ISSN: 00179310. DOI: 10.1016/0017-9310(75)90243-4.

[82] Raimund Walter. “Gegenüberstellung der Wirtschaftlichkeit von Organic Rankine Cycle und Misselhorn-Prozess”. Lehrstuhl für Energiesysteme. Forschungspraktikum. München: Technische Universität München, 2016. 75 pp.

[83] Dominik Meinel, Christoph Wieland, and Hartmut Spliethoff. “Economic Analysis of Geothermal Combined Heat and Power Processes”. In: *Proceedings of ECOS 2015.* The 28th international conference on Efficiency, Cost, Optimization, Simulation and Environmental Impact of Energy Systems (Pau, France, June 29–July 3, 2015). 2015. ISBN: 978-2-9555539-0-9.

[84] Scott Jenkins. *Chemical Engineering Plant Cost Index: 2018 Annual Value.* Ed. by Chemical Engineering. 2019. URL: https://www.chemengonline.com/2019-cepci-updates-january-prelim-and-december-2018-final/ (visited on July 13, 2019).

[85] *AD 2000 Regelwerk. Taschenbuch - Ausgabe 2018.* ger. 11. Auflage. Berlin: Beuth, 2018. 1043 pp. ISBN: 9783410283072.

[86] Bernhard Spang and Wilfried Roetzel. “Kosten und Wirtschaftlichkeit von Wärmeübertragern”. In: *VDI-Wärmeatlas. Mit 320 Tabellen.* Ed. by VDI e.V. 11., bearb. und erw. Aufl. Vol. C6. VDI-Buch. Berlin, Heidelberg: Springer Berlin Heidelberg, 2013.

[87] Donald E. Garrett. *Chemical Engineering Economics.* eng. Garrett, Donald E. (author.) Dordrecht: Springer Netherlands, 1989. 432 pp. ISBN: 9789401165464. DOI: 10.1007/978-94-011-6544-0.

[88] M. Gebhardt, H. Kohl, and Th. Steinrötter. *Preisatlas. Ableitung von Kostenfunktionen für Komponenten der rationellen Energienutzung*. Duisburg-Rheinhausen: Institut für Energie- und Umwelttechnik e.V., 2002. URL: http://www.stenum.at/media/documents/preisatlas_komplett.PDF (visited on Nov. 24, 2018).

[89] X-Rates, ed. *Monthly Average USD to Euro*. 2015. URL: https://www.x-rates.com/average/?from=USD&to=EUR&amount=1&year=2015 (visited on May 6, 2016).

[90] X-Rates, ed. *Monthly Average USD to Euro*. 2018. URL: https://www.x-rates.com/average/?from=EUR&to=USD&amount=1&year=2018 (visited on Aug. 9, 2019).

[91] Manfred Moullion. *Motor in einer Misselhornanlage*. In collab. with Raimund Walter. call. Garching bei München, May 12, 2016.

[92] Bundesministerium der Finanzen. *AfA-Tabelle für den Wirtschaftszweig Energie- und Wasserversorgung*. Table IV A 8-S 1551-9/95, 45-S 1551-20. Jan. 24, 1995. 5 pp. URL: https://www.bundesfinanzministerium.de/Content/DE/Standardartikel/Themen/Steuern/Weitere_Steuerthemen/Betriebspruefung/AfA-Tabellen/AfA-Tabelle_Energie-und-Wasserversorgung.html.

[93] Bruno Burger, ed. *Jährliche Börsenstrompreise in Deutschland 2018*. Fraunhofer-Institut für Solare Energiesysteme ISE. 2018. URL: https://www.energy-charts.de/price_avg_de.htm?price=nominal&period=annual&year=2018 (visited on Aug. 18, 2019).

[94] Bundesregierung Deutschland. *Gesetz für den Ausbau erneuerbarer Energien*. Erneuerbare-Energien-Gesetz - EEG 2017. Ed. by FNA 754-27. Jan. 1, 2017. URL: https://www.buzer.de/gesetz/11230/index.htm.

[95] Bundesverband der Energie-Abnehmer, ed. *Industriestrompreise* (inklusive Stromsteuer) in Deutschland in den Jahren 1998 bis 2019*. Statista. 2019. URL: https://de.statista.com/statistik/daten/studie/252029/umfrage/industriestrompreise-inkl-stromsteuer-in-deutschland/.

[96] Bundesnetzagentur, ed. *EEG-Umlage 2018*. press report. 2017. URL: https://www.bundesnetzagentur.de/SharedDocs/Pressemitteilungen/DE/2017/16102017_EEG-Umlage.html.

[97] Dominik Meinel, Christoph Wieland, and Hartmut Spliethoff. "Economic comparison of ORC (Organic Rankine cycle) processes at different scales". In: *Energy* 74 (2014), pp. 694–706. ISSN: 03605442. DOI: 10.1016/j.energy.2014.07.036.

[98] Moritz Gleinser and Christoph Wieland. "The Misselhorn Cycle: Batch-Evaporation Process for Efficient Low-Temperature Waste Heat Recovery". In: *Energies* 9 (5 2016), p. 337. ISSN: 1996-1073. DOI: 10.3390/en9050337.

[99] Michael Kolbeck. "Arbeitsmedien für verschiedene Kreisprozesse im Niedertemperaturbereich". Lehstuhl für Energiesysteme. Semesterarbeit. Garching: Technische Universität München, 2016.

[100] Honeywell. *Products. Refrigerants.* 2019. URL: https://www.honeywell-refrigerants.com/europe/product/tag/all-refrigerants/ (visited on Nov. 29, 2019).

[101] Ryan J. Hulse, Rajat S. Basu, Rajiv R. Singh, and Raymond H. P. Thomas. "Physical Properties of HCFO-1233zd(E)". In: *Journal of Chemical & Engineering Data* 57 (12 2012), pp. 3581–3586. ISSN: 0021-9568. DOI: 10.1021/je300776s.

[102] Dong Luo, Ahmad Mahmoud, and Frederick Cogswell. "Evaluation of Low-GWP fluids for power generation with Organic Rankine Cycle". In: *Energy* 85 (2015), pp. 481–488. ISSN: 03605442. DOI: 10.1016/j.energy.2015.03.109.

[103] Laura Fedele, Giovanni Di Nicola, J. Steven Brown, Sergio Bobbo, and Claudio Zilio. "Measurements and Correlations of cis-1,3,3,3-Tetrafluoroprop-1-ene (R1234ze(Z)) Saturation Pressure". In: *International Journal of Thermophysics* 35 (1 2014), pp. 1–12. DOI: 10.1007/s10765-013-1553-5.

[104] ASHRAE. *ASHRAE HANDBOOK 2017. Fundamentals i-p and si editions.* [S.l.]: ASHRAE, 2017. ISBN: 978-1939200594.

[105] Marco Astolfi, Matteo C. Romano, Paola Bombarda, and Ennio Macchi. "Binary ORC (Organic Rankine Cycles) power plants for the exploitation of medium–low temperature geothermal sources – Part B. Techno-economic optimization". In: *Energy* 66 (2014), pp. 435–446. ISSN: 03605442. DOI: 10.1016/j.energy.2013.11.057.

[106] Muhammad Imran, Byung Sik Park, Hyouck Ju Kim, Dong Hyun Lee, Muhammad Usman, and Manki Heo. "Thermo-economic optimization of Regenerative Organic Rankine Cycle for waste heat recovery applications". In: *Energy Conversion and Management* 87 (2014), pp. 107–118. ISSN: 01968904. DOI: 10.1016/j.enconman.2014.06.091.

[107] Bundesverband der Energie-Abnehmer e. V. *Fernwärme-Preis. VEA-Vergleich 2020*. Ed. by IHK Schleswig-Holstein. 2020. URL: https://www.ihk-schleswig-holstein.de/innovation/energie/themen/fernwaermepreisvergleich-1379476 (visited on July 10, 2020).

[108] Frank P. Incropera, David P. DeWitt, Theodore L. Bergman, and Adrienne S. Lavine. *Principles of heat and mass transfer*. eng. 7. ed., international student version. Singapore: Wiley, 2013. 1048 pp. ISBN: 978-0-470-64615-1.

[109] Frank P. Incropera, David P. DeWitt, Theodore L. Bergman, and Adrienne S. Lavine. *Fundamentals of heat and mass transfer*. eng. 6th ed. Hoboken, NJ: Wiley, 2007. 997 pp. ISBN: 978-0-471-45728-2.

[110] Warren Max Rohsenow. "Boiling". In: *Handbook of heat transfer fundamentals*. Ed. by Warren Max Rohsenow, James Patrick Hartnett, and Ejup N. Ganić. 2nd ed. Rev. ed. of: Handbook of heat transfer. New York, London, and Paris: McGraw-Hill, 1985, Chapter 12. ISBN: 0-07-053554-x.

[111] Björn Felgenhauer. *Kosten von Plattenwärmetauschern*. In collab. with Raimund Walter. E-Mail. Garching bei München, June 14, 2016.

[112] Hardydiesel, ed. *Prices of Diesel Generators*. 2016. URL: www.hardydiesel.com (visited on May 17, 2016).

Appendix A

Simulation Models

A.1 Cycle Shortcut Model

A shortcut model was implemented in MATLAB in order to get a quick, qualitative idea of temperature and pressure levels of Rankine and Organic Rankine Cycles under different reference conditions.

A.1.1 Model Description

The model needs nine input values:

- Heat source temperature T
- Heat sink temperature T_0
- Mass flow of the heat source $\dot{m}_{\mathrm{HS}}$
- Pinch Point on hot and cold side ($\mathrm{PP}_{\mathrm{hot}}$ and $\mathrm{PP}_{\mathrm{cold}}$)
- Evaporation pressure p_{evap}
- Engine efficiency η_{exp}
- Working fluid and heat source fluid

and returns the temperature-over-heatflow arrays for heat source and working fluid as well as a results structure with values of

- Available and transferred energy
- Available and transferred exergy
- State variables of the working fluid over the expansion engine
- Turbine power
- Cycle efficiencies.

The following assumptions were made:

- constant heat capacity of all fluids

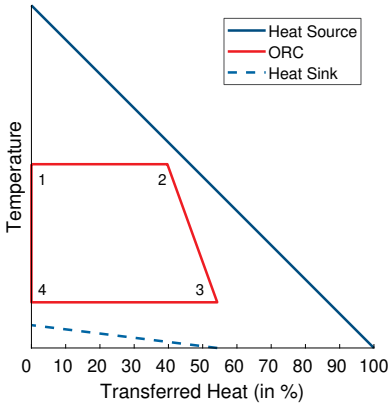

Figure A.1: Results and state points of the shortcut model.

- no pressure losses
- temperature increase of heat sink: $\Delta T_0 = 5\,\mathrm{K}$
- pressure of heat source and heat sink: $p = 4\,\mathrm{bar}$

The model then follows these steps:

1. The specific heat capacity of the heat source is calculated in Refprop [72] at the heat source inlet temperature T and the heat sink temperature T_0. Their average is used to estimate the available energy E_{av}.

$$\begin{aligned} \bar{c}_{p,\mathrm{HS}} &= \frac{c_p(T,p) + c_p(T_0,p)}{2} \\ E_{\mathrm{av}} &= (T - T_0) \cdot \bar{c}_{p,\mathrm{HS}} \cdot \dot{m}_{\mathrm{HS}} = \Delta T \cdot C_{\mathrm{HS}}. \end{aligned} \tag{A.1}$$

2. The temperatures of state points 1 and 2 (see fig. A.1) are defined by the boiling temperature at the given evaporation pressure p_{evap}. The temperatures of state points 3 and 4 are calculated from the heat sink temperature, its predefined raise and the pinch point in the condenser:

$$\begin{aligned} T_1 &= T_2 = T(p_{\mathrm{evap}}); \\ T_3 &= T_4 = T_0 + \Delta T_0 + \mathrm{PP}_{\mathrm{cold}}. \end{aligned} \tag{A.2}$$

3. The specific heat of evaporation at the evaporation temperature is calculated by Refprop $\Delta h_\mathrm{v}(T_\mathrm{evap})$. The average specific heat capacity of the liquid working fluid is estimated from $T_{(1,2)}$ and $T_{(3,4)}$ at saturated liquid conditions.

$$\bar{c}_{p,\mathrm{WF}} = \frac{c_p(T_{(1,2)}, \mathrm{sat.}_\mathrm{liq}) + c_p(T_{(3,4)}, \mathrm{sat.}_\mathrm{liq})}{2} \tag{A.3}$$

4. The position on the x-axis (transferred heat) for state points 1 and 4 is zero. The transferred heat flow for state point 2 can be derived from its temperature level and the distance (pinch point) to the heat source by means of the heat capacity of the heat source C_HS from eq. (A.1).

$$\begin{aligned} Q_1 = Q_4 &= 0; \\ Q_2 &= \left(T - (T_2 + PP_\mathrm{hot})\right) \cdot C_\mathrm{HS} \end{aligned} \tag{A.4}$$

5. The mass flow of the working fluid is then derived from the available heat for the evaporation and the specific heat of evaporation. The heat capacity of the working fluid during the preheating yields the position of Q_3

$$\begin{aligned} \dot{m}_\mathrm{WF} &= \frac{Q_2 - Q_1}{\Delta h_\mathrm{v}}; \\ Q_3 - Q_2 &= -\bar{c}_{p,\mathrm{WF}} \cdot \dot{m}_\mathrm{WF} \cdot (T_3 - T_2) \end{aligned} \tag{A.5}$$

6. If T_3 is closer to the corresponding heat source temperature at Q_3 than the pinch point allows for, the mass flow is reduced to fit this limit. The state point 2 has then also to be adjusted with the updated mass flow rate.

7. The power output is calculated from the working fluid mass flow and the enthalpy difference between state point 1 and 4.

$$P_\mathrm{out} = (h_1 - h_4) \cdot \dot{m}_\mathrm{WF} \tag{A.6}$$

While state 1 is assumed saturated, state 4 results from isentropic expansion from state 1 to the condensation temperature $T_{(3,4)}$. If the defined engine efficiency is not $\eta = 1$, the isentropic expansion is further reduced

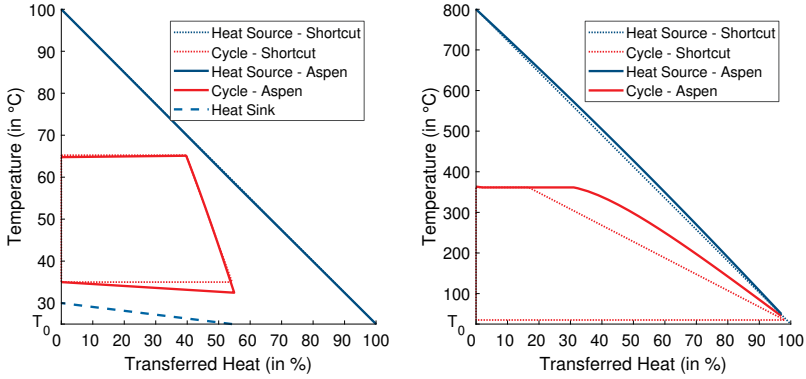

(a) Low temperature case (R134a - 19 bar) (b) High Temperature case (water - 190 bar)

Figure A.2: Comparison of the simulation results for an exemplary ORC.

by these losses:

$$\begin{aligned} h_1 &= h\left(T_{\text{evap.}}, \text{sat.}\right); \\ s_1 &= s\left(T_{\text{evap.}}, \text{sat.}\right); \\ h_{\text{is}} &= h\left(T_{\text{condense.}}, s_1\right); \\ h_4 &= (1-\eta)\cdot h_1 + \eta \cdot h_{\text{is}}; \end{aligned} \tag{A.7}$$

A.1.2 Assessment

This model was, for example, used to plot the example cycles in section 2.1.2 on page 10 and to calculate the exergy distribution for the compared low and high temperature heat source examples (see table 2.2 on page 17).

The model should only be used for a “first guess” or for qualitative comparison due to the made assumptions. The errors for low temperatures are small as can be seen in a validation against the results from Aspen Plus. While the shortcut model in fig. A.2a estimates a second law cycle efficiency of $\eta_{\text{II}} = 42\,\%$, the detailed simulation in Aspen results in $\eta_{\text{II}} = 33\,\%$. This difference origi-

nates mostly from the engine efficiency, which is included in the Aspen model with $\eta_{\text{engine}} = 80\,\%$, but is completely neglected in the shortcut approach. The difference of the bottom line of the cycle is due to the pressure losses in the Aspen model which are also not implemented in the shortcut. Without these losses, the two models give almost identical results. In Contrast, the exact numbers for high temperature cycles and properties close to the critical point may differ widely (see fig. A.2b). Especially the assumption of constant heat capacities for heat source and working fluid affect the temperature match in the simplified approach. Hence, the shortcut model yields $\eta_{\text{II}} = 44\,\%$ compared to the Aspen approach with $\eta_{\text{II}} = 51\,\%$ (without the engine losses, the detailed Aspen model would reach $\eta_{\text{II}} = 64\,\%$). Those numbers do not represent an optimized operation point but should only emphasize the discrepancy in the shortcut model. Still, the simplified model is a valid tool to illustrate the general characteristics of Rankine and Organic Rankine Cycles at different temperature levels.

A.2 Details of the MWM Model

A.2.1 Differential Equations of the Detailed Evaporator Model

The detailed evaporator model for the MWM Cycle is based on the energy balance of an exemplary control volume as shown in fig. A.3 (copy of fig. 5.3). While the main steps were already explained in section 5.1.1.2 on page 80, the detailed derivation is shown in the following paragraphs.

Heat Source Side All three balances for heat source, wall and working fluid consist of the storage term on the left side and the transport terms on the right. For the heat source side the change $\frac{\partial}{\partial t}$ of the internal energy of one differential element ΔU is subject to the ingoing and outgoing enthalpy flow ($\dot{H}_z$ and $\dot{H}_{z+\Delta z}$) and the transferred heat in x-direction to the wall $\dot{Q}_x$:

$$\frac{\partial \Delta U}{\partial t} = +\dot{H}_z - \dot{H}_{z+\Delta z} - \dot{Q}_x. \tag{A.8}$$

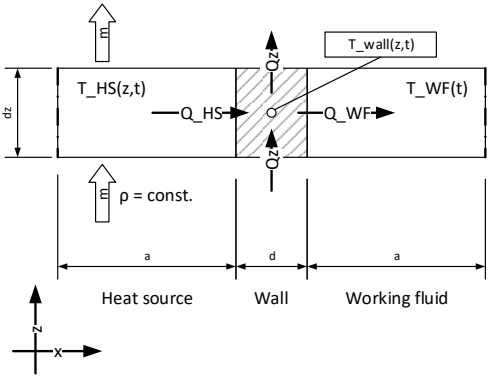

Figure A.3: Detailed control volume of the plate heat exchanger as shown in fig. 5.2.

Replacing the internal energy by the heat capacity and temperature

$$\Delta U = \Delta m \cdot c_{p,\mathrm{HS}} \cdot T_{\mathrm{HS}} = m_{\mathrm{HS}} \cdot z_{\mathrm{frac}} \cdot c_{p,\mathrm{HS}} \cdot T_{\mathrm{HS}}, \tag{A.9}$$

the enthalpy flows by specific enthalpy and mass flow

$$\dot{H} = h \cdot \dot{m} \tag{A.10}$$

and the heat flow by heat transfer coefficients, area and temperature difference

$$\dot{Q}_x = k \cdot A \cdot \Delta T = z_{\mathrm{frac}} \cdot kA_{\mathrm{HS}} \cdot (T_{\mathrm{HS}} - T_{\mathrm{wall}}) \tag{A.11}$$

gives

$$m_{\mathrm{HS}} \cdot z_{\mathrm{frac}} \cdot c_{p,HS} \frac{\partial T_{\mathrm{HS}}}{\partial t} = \dot{m}_{\mathrm{HS}} \left(h_z - h_{z+\Delta z}\right) - z_{\mathrm{frac}} \cdot kA_{\mathrm{HS}} \cdot (T_{\mathrm{HS}} - T_{\mathrm{wall}}) \,. \tag{A.12}$$

Using a first-order Taylor series approximation on the outgoing specific enthalpy yields

$$h_{z+\Delta z} \approx h_z + \frac{\partial h}{\partial z} \Delta z. \tag{A.13}$$

Inserting this approximation to eq. (A.12) already leads to the initial given differential equation in eq. (5.19) on page 81:

$$m_{\mathrm{HS}} \cdot z_{\mathrm{frac}} \cdot c_{p,\mathrm{HS}} \cdot \frac{\partial T_{\mathrm{HS}}}{\partial t} = -\dot{m}_{\mathrm{HS}} \cdot \frac{\partial h}{\partial z} \Delta z - z_{\mathrm{frac}} \cdot kA_{\mathrm{HS}} \cdot (T_{\mathrm{HS}} - T_{\mathrm{wall}})\,. \quad \text{(A.14)}$$

The specific enthalpy can then be further split up by $\mathrm{d}h = c_p\,\mathrm{d}T + v\,\mathrm{d}p$. The final steps are simple repositioning and replacing according to the relationship of L, Δz and z_{frac} that lead to the final form of the heat source equation in eq. (5.21) on page 81.

Wall For the wall equation, the change of the internal energy depends on the in- and outgoing heat flow from the heat source $\dot{Q}_{\mathrm{HS}}$ and to the working fluid $\dot{Q}_{\mathrm{WF}}$, respectively. In addition, the rather small heat conduction along the z-axis is represented by the latter two terms $\dot{Q}_z$ and $\dot{Q}_{z+\Delta z}$.

$$\frac{\partial \Delta U}{\partial t} = \dot{Q}_{\mathrm{HS}} - \dot{Q}_{\mathrm{WF}} + \dot{Q}_z - \dot{Q}_{z+\Delta z}. \quad \text{(A.15)}$$

Following the scheme of the heat source equation, the internal energy is replaced by the mass of the control volume, the specific heat capacity of the wall material c_{wall} and the wall temperature

$$\Delta U = \Delta m \cdot c_{\mathrm{wall}} \cdot T_{\mathrm{wall}} = m_{\mathrm{wall}} \cdot z_{\mathrm{frac}} \cdot c_{\mathrm{wall}} \cdot T_{\mathrm{wall}}, \quad \text{(A.16)}$$

and the heat transfer is replaced by specific heat transfer coefficients, the area and temperature differences

$$\dot{Q}_{\mathrm{HS}} = k \cdot A \cdot \Delta T \qquad = z_{\mathrm{frac}} \cdot kA_{\mathrm{HS}} \cdot (T_{\mathrm{HS}} - T_{\mathrm{wall}}) \quad \text{(A.17)}$$

$$\dot{Q}_{\mathrm{WF}} = k \cdot A \cdot \Delta T \qquad = z_{\mathrm{frac}} \cdot kA_{\mathrm{WF}} \cdot (T_{\mathrm{wall}} - T_{\mathrm{WF}})\,. \quad \text{(A.18)}$$

In analogy to the heat source side, the total wall mass m_{wall} was taken from eq. (5.14) and the two adjusted overall heat transfer numbers respond to eqs. (5.20) and (5.24), respectively. The heat flow, subject to conduction along the z-axis, is better handled as the product of heat flux and the cross section of the wall

$$\dot{Q}_z = A_{\mathrm{cross}} \cdot \dot{q}_z \quad \text{(A.19)}$$

Then, as for the specific enthalpy in eq. (A.13), the heat flux at position $z + \Delta z$ could be approximated by a Taylor series

$$\dot{q}_{z+\Delta z} \approx \dot{q}_z + \frac{\partial \dot{q}}{\partial z} \Delta z. \tag{A.20}$$

Including eqs. (A.16) to (A.20) into eq. (A.15) leads to

$$\begin{aligned} m_{\text{wall}} \cdot z_{\text{frac}} \cdot c_{\text{wall}} \cdot \frac{\partial T_{\text{wall}}}{\partial t} = & + z_{\text{frac}} \cdot kA_{\text{HS}} \cdot (T_{\text{HS}} - T_{\text{wall}}) \\ & - z_{\text{frac}} \cdot kA_{\text{WF}} \cdot (T_{\text{wall}} - T_{\text{WF}}) - A_{\text{cross}} \cdot \frac{\partial \dot{q}_z}{\partial z} \Delta z. \end{aligned} \tag{A.21}$$

With Fourier's law ($\vec{q} = -\lambda \operatorname{grad} T$), the one-dimensional heat flux can also be expressed by

$$\dot{q} = -\lambda \frac{\partial T}{\partial z} \tag{A.22}$$

Solving eq. (A.21) for $\frac{\partial T}{\partial t}$ then leads to

$$\frac{\partial T}{\partial t} = \frac{1}{m_{\text{wall}} \cdot c_{\text{wall}}} \cdot (kA_{\text{HS}} \cdot \Delta T_{\text{HS}} - kA_{\text{WF}} \cdot \Delta T_{\text{WF}}) + \frac{A_{\text{cross}} \cdot \Delta z \cdot \lambda_{\text{wall}}}{m_{\text{wall}} \cdot z_{\text{frac}} \cdot c_{\text{wall}}} \frac{\partial^2 T}{\partial z^2}. \tag{A.23}$$

The pre-factor of the last term can conveniently be repositioned to

$$\frac{A_{\text{cross}} \cdot \Delta z \cdot \lambda_{\text{wall}}}{m_{\text{wall}} \cdot z_{\text{frac}} \cdot c_{\text{wall}}} = \frac{A_{\text{cross}} \cdot L \cdot \lambda_{\text{wall}}}{m_{\text{wall}} \cdot c_{\text{wall}}} = \frac{\lambda_{\text{wall}}}{\rho_{\text{wall}} \cdot c_{\text{wall}}}, \tag{A.24}$$

where the combination of the undefined cross section A_{cross}, the cell properties (z_{frac} and Δz) and the total wall mass m_{wall} is replaced by the density of the wall material ρ_{wall}. The substitution of eq. (A.24) in eq. (A.23) results in the final form of the wall equation as shown in eq. (5.27) on page 84, where any specifics about the plate geometry are again eliminated.

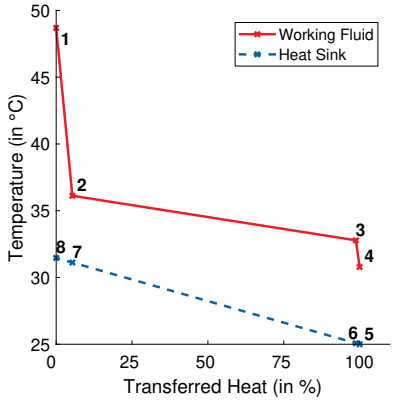

Figure A.4: Detail of the condensation and state points of the condenser shortcut model.

A.2.2 Equations of the Shortcut Condenser Model

The condenser can be approximated in the style of the heat exchanger shortcut model in appendix A.1. With the assumption of stationary conditions in the condenser even for the MWM Cycle, the following model is valid for both ORC and MWM calculations.

Figure A.4 shows are more detailed view of the condensation as for example shown in fig. A.1 (ORC) or fig. 4.3 (MWM). Depending on the cycle settings and the fluid, the working fluid may enter the condenser in a superheated state **(1)** or a two–phase state (between **(2)** and **(3)**). It is then, if superheated, cooled down to its saturation point **(2)**, condensed with some pressure drop **(3)** and subcooled for a few degrees **(4)**. The counter–flow of cold water **(5)** to **(8)** provides the heat sink for the condensation.

The properties of state point **(1)** are directly received from the evaporator model, where the enthalpy after the turbine

$$h_1 = h_{\text{exp}}$$

is already used for the power calculations in eq. (5.32). With the known pressure after the turbine $p_1 = p_{\text{exp}}$ (reference condition to the model), REFPROP

provides the corresponding temperature

$$T_1 = f(h_1, p_1).$$

State **(2)** simply are the saturated vapor conditions at the expansion pressure

$$T_2, h_2 = f(p_1, \mathrm{sat}_{\mathrm{vap}}).$$

When the expanded stream is in the two–phase state and state **(1)** is already beyond the saturated vapor, states **(1)** and **(2)** become identical and both hold the actual values of the expansion stream. State **(3)** is defined as the saturated liquid at p_1 reduced by the pressure drop of the working fluid over the condenser $p_3 = p_1 - \Delta p_{\mathrm{WF,cond}}$ (again a reference condition to the model)

$$T_3, h_3 = f(p_3, \mathrm{sat}_{\mathrm{liq}}).$$

The final state **(4)** of the working fluid results from the subcooling of state **(3)** by $\Delta T_{\mathrm{WF,cond}} = 2\,\mathrm{K}$

$$T_4 = f(p_3, \mathrm{sat}_{\mathrm{liq}}) - \Delta T_{\mathrm{WF,cond}}$$

and the corresponding enthalpy

$$h_4 = f(p_3, T_4).$$

The state points of the cooling water correspond to the four states of the working fluid. State **(5)** are the given reference conditions of the model. The massflow is then calculated in order to ensure a pinch point of $\mathrm{PP}_{\mathrm{cond}} = 5\,\mathrm{K}$ between the states **(2)** and **(7)**

$$T_7 = T_2 - \mathrm{PP}_{\mathrm{cond}}.$$

The enthalpy of the water at this point is based on the temperature and the remaining pressure of the water $p_7 = p_5 - \Delta p_{\mathrm{H2O,cond}}$ by

$$h_7 = f(T_7, p_7).$$

The mass flow of the cooling water has to match the released enthalpy flow of the working fluid between the known states **(2)** to **(4)** and **(5)** to **(7)**, respec-

tively

$$\dot{m}_{\mathrm{H2O,cond}} = -\frac{\overline{\dot{m}}_{\mathrm{WF,out}} \cdot (h_4 - h_2)}{h_7 - h_5}.$$

The enthalpies of the two missing state points **(6)** and **(8)** can then be derived from the corresponding enthalpy difference on the working fluid side and the two mass flows by

$$h_k = h_5 + \frac{\Delta h_{\mathrm{WF}} \cdot \overline{\dot{m}}_{\mathrm{WF,out}}}{\dot{m}_{\mathrm{H2O,cond}}}.$$

The according temperatures are taken from REFPROP with the approximated pressure levels of $p_6 = p_5$ and $p_8 = p_7$ by

$$T_k = f(h_k, p_k).$$

Considering that the condensation itself takes up most of the heat exchanger area, the major part of the pressure drop is in good approximation distributed to the section **(6)** to **(7)**.

With all state points set, the area of the condenser for the economic evaluation can be estimated with the mean logarithmic temperature difference (LMTD) of each section of the condenser by

$$A = \frac{\dot{Q}}{k \cdot LMTD},$$

where k is the heat transfer coefficient of each section (saturation, condensation, subcooling) and the $LMTD$ is defined, at the example of the condensation section, by

$$\begin{aligned} LMTD &= \frac{(\Delta T_2 - \Delta T_1)}{\log(\Delta T_2 / \Delta T_1)}, \text{ with} \\ \Delta T_1 &= T_2 - T_7 \\ \Delta T_2 &= T_3 - T_6. \end{aligned}$$

The heat transfer coefficients k for the condenser are given in section 5.3.1 on page 97 together with those for the evaporators.

A.3 Correlations for Heat Transfer Coefficients in Evaporators and Condensers

Three important dimensionless numbers in the context of heat transfer correlations are the Reynolds number Re, the Prandtl number Pr and the Nusselt number Nu. Common literature on heat transfer, as for example Marek and Nitsche [74], Shah and Sekulić [77], and Incropera et al. [108], uses the following definitions:

- The Reynolds number gives the ratio of the force of inertia to the viscosity and is an important number for forced convection.

$$\mathrm{Re} = \frac{\mathrm{v} \cdot L_0}{\nu}, \tag{A.25}$$

  where v is the flow velocity, L_0 is a characteristic length (in most cases the flow diameter) and ν is the kinematic viscosity.

- The Prandtl number shows the ratio of momentum transport to heat transport of a fluid and is therefore an important number for fluid properties.

$$\mathrm{Pr} = \frac{\nu}{a} = \frac{\eta \cdot c_p}{\lambda}, \tag{A.26}$$

  where $a = \frac{\lambda}{\rho \cdot c}$ is the thermal diffusivity and $\eta = \nu \cdot \rho$ is the dynamic viscosity.

- Similar to the Biot number, the Nusselt number is defined as the ratio of heat transfer to heat conduction. Only while the Biot number refers to the heat conduction within solids, the Nusselt number is its equivalent for fluids. Being the dimensionless heat transfer coefficient, the Nusselt number is the final output of many heat transfer correlations.

$$\mathrm{Nu} = \frac{\alpha}{\lambda_{\mathrm{fluid}}/L_0}. \tag{A.27}$$

The following correlations where used to estimate typical heat transfer coefficients in plate heat exchangers.

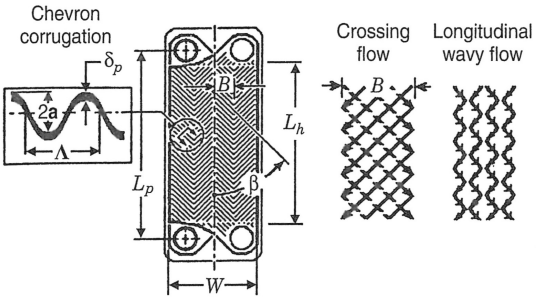

Figure A.5: Geometrical parameters of a chevron plate (From Martin [75], edited by Shah and Sekulić [77]).

A.3.1 Forced Convection in Plate Heat Exchangers

The detailed correlation for a forced convective single–phase flow in a plate heat exchanger as recommended by Shah and Sekulić [77] was originally introduced by Martin [75]. Martin [75] first defines several geometric parameters to describe the plate geometry (see fig. A.5). The basic dimensions of one plate are the height or length L (the subscript p denotes the length for pressure drop calculations, the subscript h denotes the length for heat transfer) and the width W, where B is the width of the herringbone structure (here: $W = 4B$). The wavy structure is defined by the wavelength Λ, the wave amplitude a, the plate thickness δ or s and the chevron angle φ (the angle is labeled as β in fig. A.5, but in this work φ is chosen to not be confused with the thermal expansion coefficient). The average distance between two plates is $2a$.

From these characteristics, the area enlargement factor Φ, which describes the ratio between the developed surface area and the projected surface area, can be calculated as

$$\Phi(X) \approx \frac{1}{6}\left(1 + \sqrt{1+X^2} + 4\sqrt{1+X^2/2}\right), \tag{A.28}$$

where the dimensionless corrugation parameter X is

$$X = 2a\pi/\Lambda. \tag{A.29}$$

The area enlargement factor can then be used to calculate the hydraulic diameter d_H which is used as the characteristic length L_0 in the Reynolds number

$$d_H = 4a/\Phi. \tag{A.30}$$

The needed flow velocity can be calculated from the overall fluid mass flow $\dot{m}$ and the overall flow cross section $A_0 = 2aWN_P$ with the number of plates N_P.

The plate geometry primarily affects the flow pattern and has a direct influence on the pressure losses. The overall pressure drop Δp is given by

$$\Delta p = \underbrace{4f \cdot \frac{L}{d_H} \cdot \frac{\rho u^2}{2}}_{\text{friction}} + \underbrace{\rho g H}_{\text{gravity}}, \tag{A.31}$$

which includes the pressure drop due to friction as well as the gravitational pressure drop. For vertical flows, the height H is equal to the length L of the flow. The fanning friction factor f for the plate gap is calculated by

$$\frac{1}{\sqrt{f}} = \frac{\cos\varphi}{\sqrt{0.045\tan\varphi + 0.09\sin\varphi + f_0/cos\varphi}} + \frac{1-\cos\varphi}{\sqrt{3.8 f_1}}. \tag{A.32}$$

The numbers f_0 and f_1 are for the two limiting cases with $\varphi = 0°$ and $\varphi = 90°$, respectively. Their values are given by Shah and Sekulić [77] as

$$f_0 = \begin{cases} \dfrac{16}{\mathrm{Re}} & \text{for } \mathrm{Re} < 2000 \\ \left(1.56\log_{10}\mathrm{Re} - 3.0\right)^{-2} & \text{for } \mathrm{Re} \geq 2000 \end{cases} \tag{A.33}$$

and

$$f_1 = \begin{cases} \dfrac{149.25}{\mathrm{Re}} + 0.9625 & \text{for } \mathrm{Re} < 2000 \\ \dfrac{9.75}{\mathrm{Re}^{0.289}} & \text{for } \mathrm{Re} \geq 2000 \end{cases} \tag{A.34}$$

Based on the friction factor, the heat transfer coefficient α_{HS} for forced convection in the plate gap is then given in form of the Nusselt number by

Shah and Sekulić [77] as

$$\mathrm{Nu} = \frac{\alpha_{\mathrm{HS}} \cdot d_{\mathrm{H}}}{\lambda_{\mathrm{HS}}} = 0.205 \cdot \mathrm{Pr}^{1/3} \cdot \left(\frac{\eta_{\mathrm{HS}}}{\eta_{\mathrm{HS,wall}}} \right)^{1/6} \cdot \left(f \cdot \mathrm{Re}^2 \sin 2\varphi \right)^{0.374}. \quad \text{(A.35)}$$

As for all other equations, the subscript HS denotes properties of the heat source medium. Attention has to be paid concerning $\eta_{\mathrm{HS,wall}}$ which is the viscosity of the heat source medium at wall temperature, whereas η_{HS} is the viscosity at the bulk temperature of the fluid.

A.3.2 Generic Nucleate Pool Boiling

As soon as the wall temperature exceeds the boiling temperature of the working fluid by more than a certain, fluid specific amount ΔT_{e}, bubbles start to form and the nucleate boiling begins. This excess temperature is called "onset of nucleate boiling" (T_{ONB}) and can be approximated according to Smith [80] by the equation

$$T_{\mathrm{ONB}} = T_{\mathrm{s}} + \Delta T_{\mathrm{e}} = T_{\mathrm{s}} + \left(\frac{8\sigma_{\mathrm{liq}} \cdot \dot{q} \cdot T_{\mathrm{s}}}{\lambda_{\mathrm{WF}} \cdot \Delta h_{\mathrm{v}} \cdot \rho_{\mathrm{vap}}} \right)^{1/2} \cdot \mathrm{Pr}_{\mathrm{liq}}. \quad \text{(A.36)}$$

The subscript s denotes saturated properties, σ is the surface tension, $\dot{q}$ is the local heat flux and Δh_{v} is the heat of vaporization. The subscripts liq and vap denote the properties of the liquid and vapor phase, respectively.

Instead of a dimensionless coefficient, the actual heat flux caused by the nucleate pool boiling can directly be calculated by the equation proposed by Incropera et al. [109]. It is based on the original findings of Rohsenow [79], which are still recommended (e.g. by Polifke and Kopitz [73] and Rohsenow [110]):

$$\dot{q} = \eta_{\mathrm{liq}} \cdot \Delta h_{\mathrm{v}} \cdot \left[\frac{g(\rho_{\mathrm{liq}} - \rho_{\mathrm{vap}})}{\sigma} \right]^{1/2} \cdot \left[\frac{c_{p,\mathrm{liq}} \cdot \Delta T_{\mathrm{e}}}{C_{\mathrm{sf}} \cdot \mathrm{Pr}_{\mathrm{liq}}^{n}} \right]^{3}. \quad \text{(A.37)}$$

The coefficient C_{sf} and the exponent n are dependent on the involved fluid and the wall material. For organic fluids the exponent can be assumed to be $n = 1.7$ and the coefficient varies between 0.0027 and 0.0154. For this model it is averaged as $C_{\mathrm{sf}} = 0.01$.

The boiling heat transfer is limited by the critical heat flux at which point the bubbles start to form a closed film which will insulate the hot wall and interfere with the heat transfer. To represent this effect in the model, the heat flux is limited to a maximal value that is calculated according to Smith [80] as

$$\dot{q}_{\mathrm{crit}} = 0.131 \cdot \Delta h_{\mathrm{v}} \cdot \rho_{\mathrm{vap}} \cdot \left[\frac{\sigma g (\rho_{\mathrm{liq}} - \rho_{\mathrm{vap}})}{\rho_{\mathrm{vap}}^2} \right]. \tag{A.38}$$

A.3.3 Generic Natural Convection on a Vertical Plate

As there are no specific correlations for natural convection in plate heat exchangers, the widely used correlation of Churchill and Chu [81] for natural convection on vertical plates (recommended by Marek and Nitsche [74] and Incropera et al. [109]) was implemented. Comparable to the Reynolds number for forced flows, the Grashof number Gr is used to describe natural convective flows:

$$\mathrm{Gr} = \frac{g \beta_p \cdot |T_{\mathrm{wall}} - T_{\mathrm{bulk}}| \, L^3}{\nu_{\mathrm{WF}}^2}. \tag{A.39}$$

It is often combined with the Prandtl number to the derived dimensionless Rayleigh number $\mathrm{Ra} = \mathrm{Gr} \cdot \mathrm{Pr}$ and contains the gravitational acceleration g, the thermal expansion coefficient β_p, the temperature difference ΔT between wall and fluid bulk, the length of the natural convection area L (here the height of the liquid level or the height of the gas phase area) and the kinematic viscosity ν. The subscript WF again identifies properties of the working fluid. Using these numbers, the heat transfer coefficient can be calculated from the average Nusselt number

$$\overline{\mathrm{Nu}} = \frac{\alpha_{\mathrm{WF}} \cdot L}{\lambda_{\mathrm{WF}}} = \left\{ 0.825 + \frac{0.387 \cdot \mathrm{Ra}^{1/8}}{\left[1 + (0.492/\mathrm{Pr})^{9/16} \right]^{8/27}} \right\}^2 \tag{A.40}$$

Appendix B

Custom Cost Regressions for Economic Evaluation

B.1 Plate Heat Exchangers

The common cost correlations for plate heat exchangers tend to over–estimate the prices for small components. As there were actual prices available from the pilot plant at MWM, Walter [82] introduced a custom correlation.

Based on personal correspondence with Felgenhauer [111] from SWEP, Walter summarized the costs for PHE models as given in table B.1. The two alternative brazed plate heat exchanger models were both selected for their suitable material and pressure class. Their price is built from a basic price for the frame and the connections and is then extended by a flex price for every additional plate. For higher needed total heat transfer areas, several modules can be modularly connected. The costs can then be estimated with the known eq. (2.35) and the coefficients from table B.2. The final fit as used in the simulation can be seen in fig. B.1.

Table B.1: Actual Costs for Brazed Plate Heat Exchangers [111].

Model	Basic Price (€)	Flex Price (€ per plate)	Area per Plate (m^2)	max. Plates (-)
B80TH (1P-SC-M)	48.93	1.725	0.063	100
B120TH (1P-SC-M)	40.93	4.125	0.128	180

Table B.2: Custom Coefficients for Module Costing Technique Basic Costs

Component	Characteristic Dimension X	C_1	C_2	C_2
Heat Exchanger	Area m^2	1.7540	0.8619	0.0288
Motor-Generator Set	max. Power (kW)	3.6894	1.4800×10^{-8}	0.1734

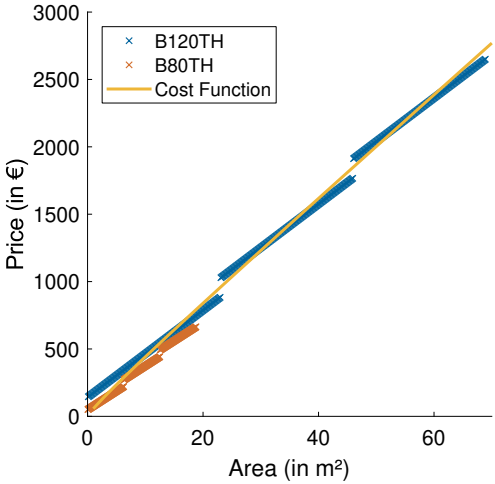

Figure B.1: Custom Cost Function for small Plate Heat Exchangers

B.2 Motor-Generator Set

The price for a motor-generator set includes a modified piston engine and a generator. As tested on the pilot plant, it is intended to use a common diesel engine for the MWM Cycle where only the cam shaft, the valves and the cylinder heads have to be changed. In correspondence with Moullion [91] from MWM, Walter [82] estimated a fixed addition of 3000 € for the custom cam shaft. The costs for the valves and cylinder heads depend on the number of cylinders and are accounted for with 5 % and 10 % of the market price, respectively. The cost estimation was based of prices from Hardydiesel [112]

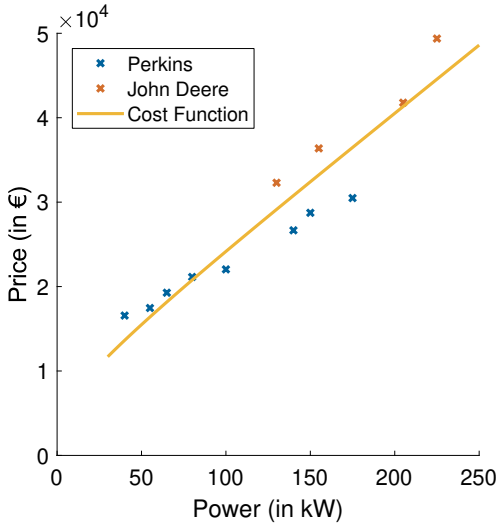

Figure B.2: Custom Cost Function for the Final Price of the Customized Motor-Generator-Sets

as listed in table B.3. The costs where converted from $ to € with the average exchange rate from 2015 (1€ = $1.11[89]). The custom cost fit, as seen in fig. B.2, gives the coefficients in table B.2.

Table B.3: Actual Costs for Diesel Engine-Generator Sets [112].

Brand	Model	Power (kW)	Market Price ($)	Market Price (€)	Customized (€)
Perkins	HDPK-40-3P	40	12 652.00	11 398.20	16 557.93
	HDPK-55-3P	55	13 517.00	12 177.48	17 454.10
	HDPK-65-3P	65	15 264.00	13 751.35	19 264.05
	HDPK-80-3P	80	17 064.00	15 372.97	21 128.92
	HDPK-100-3P	100	17 930.00	16 153.15	22 026.13
	HDPK-140-3P	140	22 274.00	20 066.67	26 526.67
	HDPK-150-3P	150	24 394.00	21 976.58	28 723.06
	HDPK-175-3P	175	26 081.00	23 496.40	30 470.86
John Deere	HDHIJD-130	130	27 828.00	25 070.27	32 280.81
	HDHIJD-155	155	31 757.00	28 609.91	36 351.40
	HDHIJD-205	205	36 980.00	33 315.32	41 762.61
	HDHIJD-225	225	44 306.00	39 915.32	49 352.61

Appendix C

Optimization Results

Additional optimized cycle results at heat source temperatures of 120 °C and 140 °C.

C.1 Thermodynamic Optimizations

120 °C See table C.1 on the following page for the ORC and table C.2 on page 209 for the MWM Cycle.

140 °C See table C.3 on page 210 for the ORC and table C.4 on page 211 for the MWM Cycle.

C.2 Economic Optimizations

120 °C See table C.5 on page 212 for the ORC and table C.6 on page 213 for the MWM Cycle.

140 °C See table C.7 on page 214 for the ORC and table C.8 on page 215 for the MWM Cycle.

Table C.1: Thermodynamic cycle performance of the ORC for different working fluids at a heat source temperature of 120 °C

Fluid		R134a	R227ea	R1234ze(E)	Isobutylene	R1233zD(E)
Net power	P_{net} (kW)	51.2	53.8	49.6	44.8	41.9
Self consumption	P_{self} (kW)	7.6	7.4	5.8	3.0	1.7
Second law efficiencies	$\eta_{II,int}$ (%)	46.6	46.7	45.2	43.0	41.8
	$\eta_{II,ext}$ (%)	82.5	85.6	82.3	78.3	75.4
	η_{II} (%)	**38.5**	**40.4**	**37.2**	**33.7**	**31.5**
Evaporation pressure	p_{evap} (bar)	28.4	21.4	20.5	11.6	6.4
Condensation pressure	p_{exp} (bar)	8.4	5.9	6.4	4	1.9

Table C.2: Cycle performance of the MWM Cycle for different working fluids at a heat source temperature of 120 °C (unheated discharge and six heat exchangers)

Cycle		ORC	MWM				
Fluid		R134a	R134a	R227ea	R1234ze(E)	Isobutylene	R1233zD
Net power	P_{net} (kW)	51.2	59.30	53.30	55.30	65.90	59.30
Self consumption	P_{self} (kW)	7.6	3.50	3.60	3.90	2.10	2.60
Second law efficiencies	$\eta_{\text{II,int}}$ (%)	46.6	50.00	48.30	56.70	54.00	53.00
	$\eta_{\text{II,ext}}$ (%)	82.5	89.30	83.00	78.20	91.80	86.50
	η_{II} (%)	**38.5**	**44.60**	**40.10**	**41.60**	**49.60**	**44.60**
Total heat transfer	kA_{all} (kW/K)	-	11.35	15.29	12.65	25.88	18.25
Free volume	$V_{\text{HX},0}$ (m^3)	-	0.10	0.08	0.12	0.33	0.15
Plate thickness	s (mm)	-	1.20	0.60	1.20	0.50	1.10
Wave amplitude	a (mm)	-	1.50	1.50	1.50	1.50	1.50
Mass flow	$\dot{m}_{\text{WF,fill}}$ (kg/s)	-	20	20	20	20	17
Maximum mass	$m_{\text{WF,fill}}$ (kg)	-	40	40	40	40	40
Switch pressure	$p_{\text{WF,switch}}$ (bar)	-	12.20	11.92	15.50	5.12	3.14
Discharge flow	$\dot{V}_{\text{WF,dis}}$ (m^3/min)	-	5.36	6.33	5.43	11.48	18.03

Table C.3: Thermodynamic cycle performance of the ORC for different working fluids at a heat source temperature of 140 °C

Fluid		R134a	R227ea	R1234ze(E)	Isobutylene	R1233zD(E)
Net power	P_{net} (kW)	72.2	76.0	72.7	60.2	56.3
Self consumption	P_{self} (kW)	11.1	11.0	9.9	4.2	2.2
Second law efficiencies	$\eta_{II,int}$ (%)	48.3	49.6	50.4	46.4	44.6
	$\eta_{II,ext}$ (%)	96.0	98.4	92.8	83.4	81.2
	η_{II} (%)	**46.4**	**48.4**	**46.7**	**38.7**	**36.2**
Evaporation pressure	p_{evap} (bar)	30.4	23.0	27.4	15.0	8.3
Condensation pressure	p_{exp} (bar)	8.4	5.9	6.4	4	1.9

Table C.4: Cycle performance of the MWM Cycle for different working fluids at a heat source temperature of 140 °C (unheated discharge and six heat exchangers)

Cycle		ORC	MWM	
Fluid		R134a	Isobutylene	R1233zD(E)
Net power	P_{net} (kW)	72.2	80.20	72.90
Self consumption	P_{self} (kW)	11.1	2.30	1.50
Second law efficiencies	$\eta_{\text{II,int}}$ (%)	48.3	57.00	52.00
	$\eta_{\text{II,ext}}$ (%)	96.0	90.50	90.20
	η_{II} (%)	**46.4**	**51.60**	**46.90**
Total heat transfer	kA_{all} (kW/K)	-	18.89	13.26
Free volume	$V_{\text{HX},0}$ (m^3)	-	0.27	0.09
Plate thickness	s (mm)	-	1.20	1.10
Wave amplitude	a (mm)	-	1.50	1.60
Massflow	$\dot{m}_{\text{WF,fill}}$ (kg/s)	-	20	19
Maximum mass	$m_{\text{WF,fill}}$ (kg)	-	40	40
Switch pressure	$p_{\text{WF, switch}}$ (bar)	-	6.85	2.89
Discharge flow	$\dot{V}_{\text{WF, dis}}$ (m^3/min)	-	10.88	19.35

Table C.5: Economic performance of different fluids in the ORC at a heat source temperature of 120 °C

Working fluid		R134a	R227ea	R1234ze(E)	Isobutylene	R1233zD(E)
Evaporation pressure	p_{evap} (bar)	28.40	21.40	20.50	11.60	6.30
Annuities	$A_{N,C}$ (€)	−11 380	−11 623	−10 903	−9093	−8300
	$A_{N,O}$ (€)	−17 192	−17 398	−16 740	−15 822	−15 305
	$A_{N,P}$ (€)	83 965	88 266	81 139	73 586	68 769
	A_N (€)	**55 391**	**59 245**	**53 795**	**48 971**	**45 163**
Economics	SIC (€/kW)	2926	2846	2826	2679	2619
	IRR (%)	50.10	52.00	51.90	54.20	55.10
	dPBT (a)	2.11	2.03	2.04	1.94	1.91
Bare Module Costs	pump (€)	27 369	26 655	24 162	18 715	16 403
	turbine (€)	65 052	67 346	61 957	55 036	50 833
	condenser (€)	7140	7564	7038	6456	6057
	evaporator (€)	1656	2083	1497	1152	1064
Initial Investment	K_0 (€)	149 880	153 620	140 210	120 570	110 170

Table C.6: Optimized economic results of the MWM Cycle (R134a with a 120 °C heat source).

Cycle		ORC	MWM			
Number of evaporators		1	3	4	5	6
Net power	P_{net} (kW)	51.20	47.20	52.10	55.70	48.70
Self consumption	P_{self} (kW)	7.60	4.00	4.50	3.40	3.90
Second law efficiency	η_{II} (%)	**38.50**	**35.50**	**39.20**	**41.90**	**36.60**
Total heat transfer	kA_{all} (kW/K)	40.50	34.00	19.70	12.20	24.50
Free volume	$V_{HX,0}$ (m^3)	-	0.06	0.09	0.09	0.08
Plate thickness	s (mm)	-	0.50	0.50	1.10	0.60
Wave amplitude	a (mm)	-	1.70	1.70	1.90	2.00
Massflow	$\dot{m}_{WF,fill}$ (kg/s)	-	10	6	14	15
Maximum mass	$m_{WF,fill}$ (kg)	-	38	40	40	39
Switch pressure	$p_{WF,switch}$ (bar)	-	13.40	17.80	11.40	11.90
Discharge flow	$\dot{V}_{WF,dis}$ (m^3/min)	-	4.64	4.46	5.19	5.50
Annuities	$A_{N,C}$ (€)	−11 380	−13 405	−17 872	−20 192	−16 601
	$A_{N,O}$ (€)	−17 192	−15 362	−17 231	−18 257	−16 699
	$A_{N,P}$ (€)	89 965	55 087	60 891	65 049	56 841
	A_N (€)	**55 391**	**26 320**	**25 788**	**26 599**	**23 542**
Economics	SIC (€/kW)	2926	3105	4118	4395	3917
	IRR (%)	50.10	30.20	22.00	20.40	22.80
	dPBT (a)	2.11	3.48	4.76	5.10	4.56
Initial Investment	K_0 (€)	149 880	146 430	214 680	244 780	190 630

Table C.7: Economic performance of different fluids in the ORC at a heat source temperature of 140 °C

Working fluid		R134a	R227ea	R1234ze(E)	Isobutylene	R1233zD(E)
Evaporation pressure	p_{evap} (bar)	30.40	23.00	27.40	15.00	8.30
Annuities	$A_{N,C}$ (€)	−14 600	−15 040	−14 200	−11 129	−10 019
	$A_{N,O}$ (€)	−19 468	−19 759	−19 308	−17 409	−16 730
	$A_{N,P}$ (€)	117 996	124 247	118 851	98 479	92 082
	A_N (€)	**83 928**	**89 448**	**85 341**	**69 940**	**65 333**
Economics	SIC (€/kW)	2675	2619	2585	2455	2369
	IRR (%)	57.00	58.60	59.20	61.50	63.40
	dPBT (a)	1.85	1.80	1.78	1.71	1.66
Bare Module Costs	pump (€)	32 108	30 983	30 482	21 130	17 120
	turbine (€)	85 458	88 197	84 820	69 986	64 829
	condenser (€)	9368	10 098	8583	6964	6521
	evaporator (€)	2819	4434	2327	1247	1121
Initial Investment	K_0 (€)	193 040	199 040	187 930	147 850	133 410

Table C.8: Optimized economic results of the MWM Cycle (R1233zD(E) with a 140 °C heat source).

Cycle		ORC (R134a)	MWM			
Number of evaporators		1	3	4	5	6
Net power	P_{net} (kW)	72.20	60.70	66.90	70.00	72.00
Self consumption	P_{self} (kW)	11.10	1.40	1.60	1.60	1.80
Second law efficiency	$\boldsymbol{\eta_{\text{II}}}$ **(%)**	**46.40**	**39.10**	**43.00**	**45.10**	**46.30**
Total heat transfer	kA_{all} (kW/K)	67.80	20.50	20.10	13.80	14.90
Free volume	$V_{\text{HX},0}$ (m^3)	-	0.07	0.07	0.07	0.07
Plate thickness	s (mm)	-	1.20	0.50	1.20	1.20
Wave amplitude	a (mm)	-	1.50	1.50	1.50	1.50
Massflow	$\dot{m}_{\text{WF,fill}}$ (kg/s)	-	16	11	10	9
Maximum mass	$m_{\text{WF,fill}}$ (kg)	-	40	40	40	40
Switch pressure	$p_{\text{WF, switch}}$ (bar)	-	4.54	4.24	3.90	4.35
Discharge flow	$\dot{V}_{\text{WF, dis}}$ (m^3/min)	-	15.50	16.70	17.60	17.40
Annuities	$A_{\text{N,C}}$ (€)	−14 600	−13 933	−15 279	−16 406	−17 292
	$A_{\text{N,O}}$ (€)	−19 468	−15 770	−16 389	−16 893	−17 253
	$A_{\text{N,P}}$ (€)	117 996	70 915	78 094	81 822	84 085
	$\boldsymbol{A_{\text{N}}}$ **(€)**	**83 928**	**41 211**	**46 426**	**48 524**	**49 541**
Economics	SIC (€/kW)	2675	2453	2470	2566	2676
	IRR (%)	57.00	41.40	41.70	40.20	38.50
	dPBT (a)	1.85	2.55	2.53	2.63	2.74
Initial Investment	K_0 (€)	193 040	148 960	165 180	179 760	192 630